Monte Carlo and Self-Consistent Feynman Diagram Studies of Magnetic and Correlated Electron Models

by

CEJUN LIU

(Under the direction of H.-B. Schüttler)

Abstract

A Metropolis-Type Dynamics and the Monte Carlo Damage Spreading technique are proposed to study Ising, mixed-spin Ising, and Blume-Capel models on the 2-dimensional square lattice. For the mixed spin Ising model, our results strongly suggest that this spin model may have a tricritical point at finite temperature; For S=1 and 2 integer spin Blume-Capel models, our results suggest there exists one multi-critical point along the order-disorder transition line. For S=3/2 and 5/2 half-integer spin Blume-Capel models, our results show that this multi-critical behavior does not exist.

The Self-Consistent High-Order Feynman Diagram Expansion Technique is introduced and then employed to study two correlated electron models: the Hubbard Model (HBM) and the Anderson Impurity Model (AIM) with maximum expansion order $n = 3$. The basic idea of Monte Carlo Summation technique combined with the Self-Consistent Feynman Diagram Expansion, the initial results, and proposed future work on this topic are also presented.

Index words: Monte Carlo, Damage Spreading, Ising Model, Mixed Spin Ising Model, Blume-Capel Model, Self-Consistent Feynman Diagram Expansion, Hubbard Model, Anderson Impurity Model, Monte Carlo Summation Technique

Monte Carlo and Self-Consistent Feynman Diagram Studies of Magnetic and Correlated Electron Models

by

CEJUN LIU

M.S. , Shanghai Jiao Tong University, China, 1991

B.S. , Hunan Educational Institute, China, 1987

Diploma , XiangTan Normal University, China, 1982

A Dissertation Submitted to the Graduate Faculty

of The University of Georgia in Partial Fulfillment

of the

Requirements for the Degree

Doctor of Philosophy

Athens, Georgia

2002

Monte Carlo and Self-Consistent Feynman Diagram Studies of Magnetic and Correlated Electron Models

by

CEJUN LIU

Approved:

Major Professor: H.B. Schüttler

Committee: M.R. Geller
W.M. Dennis
D.P. Landau
S.P. Lewis

Electronic Version Approved:

Maureen Grasso
Dean of the Graduate School
The University of Georgia
December 2002

Acknowledgments

I would like to thank my supervisor Dr. H.-B. Schüttler for his instruction, help, patience, understanding and support during the process of this research work.

I also thank my wife (Qun Wang), my parents and my elder sister for their encouragement and consistent support during these years.

I would also like to thank Dr. D.P. Landau, Dr. S.P. Lewis, Dr. W.M. Dennis, and Dr. M.R. Geller, not only for serving as committee members, but also for helpful discussions, suggestions in my research work, and for many benefits I obtained from taking their courses. I would also like to thank Dr. A. Voigt for helpful discussions and suggestions in this work.

I greatly appreciate the Department of Physics and Astronomy for granting a teaching assistantship, and the Center for Simulational Physics for the use of the computer facilities.

I greatly appreciate Prof. H.-B. Schüttler for granting a research assistantship. This work was financially supported by US National Science Foundation under NSF Grant No. DMR-9970291 and No. ITR-0081789.

Table of Contents

List of Figures

Chapter 1

Introduction

It could be argued that current physics research can be divided into three areas - theoretical, experiment, and computational. Numerical approaches, in which systems are mimicked as accurately as possible using a computer or in which computer models are set up to provide well-behaved experimental systems are increasingly providing a bridge between theory and experiment.

A powerful numerical approach is the Metropolis Monte Carlo method. It was introduced in 1953 at the dawn of computer age and its range of applicability and accuracy have continued to increase with the development of more advanced technology. One of the simplest and most natural applications is to discrete magnetic spin models. In the first part of this work, we will study the *Ising* model, *mixed spin* Ising model and *Blume-Capel* model on the two-dimensional square lattice by using the Monte Carlo Damage Spreading (MCDS) technique. The reasons why I choose mixed spin Ising model and Blume-Capel model to be studied are that there are two opposite conclusions regarding the existence or not of the tricritical point. Here, we first introduce the MCDS technique and a Metropolis-type Dynamics on the basis of Metropolis Monte Carlo principle, then we use this technique to study the above spin models. For the mixed spin Ising model, our results strongly suggest that this spin model may have a tricritical point at finite temperature. We also employ the damage spreading technique to study the general integer and half-integer spin-S Blume-Capel model on the square lattice. For S=1 and 2 integer spins, our results

suggest that there exists one multi-critical point along the order-disorder transition line. For S=3/2 and 5/2 half-integer spins, our results show that this multi-critical behavior does not exist for this model.

The interacting fermion problem is of fundamental importance in a wide range of research areas, including fields as diverse as electronic structure theory of solids, strongly correlated electron physics, quantum chemistry, and the theory of nuclear matter. The Self-Consistent High-Order Feynman Diagram Expansions Technique is potentially a very efficient tool for the controlled approximate solution of interacting fermion models. In the second part of this work, we will first introduce the Self-Consistent Feynman Diagram Expansion (SCFDE) Technique, and then implement a brute force summation technique to evaluate the expansion for two correlated electron models, the 2D Hubbard model(2DHBM) and the Anderson Impurity Model (AIM), with maximum expansion order $n = 3$. At last, we briefly present a Monte Carlo Summation Technique for evaluating the Self-Consistent Feynman Diagram Expansion and initial calculation results comparing the brute force and Monte Carlo summation results. The implementation of this Monte Carlo diagram summation method for higher, $n > 3$, order Feynman diagram poses major algorithmic and computational challenges and is the direction of our future work on this topic.

The outline of this thesis is as follows: Chapter 2 reviews the theoretical background about the Monte Carlo method and Damage Spreading technique. Chapter 3 first introduces a Metropolis-Type dynamics, and then presents the MCDS results for Ising, mixed spin Ising, and Blume-Capel models. The Self-Consistent Feynman Diagram Expansion Technique is introduced in Chapter 4, and the calculation results for Hubbard model and Anderson Impurity Model are presented in Chapter 5. In Chapter 6, we briefly present the basic principle of the Monte Carlo Summation Technique combined with the Self-Consistent Feynman Diagram Expansion, and the initial results.

Chapter 2

The Monte Carlo (MC) Method

2.1 Introduction

The Monte Carlo(MC) method is defined by representing the solution of a problem as a parameter of a hypothetical population, and using a random sequence of numbers to construct a sample of the population, from which statistical estimates of the parameter can be obtained.

The definition shows that the scope of applications is enormous and fascinating. Many problems that at first glance do not seem to allow treatment with the MC method, can be transformed into stochastic ones. Here we concentrate on the description of MC method to statistical mechanics problems [1]-[4].

2.2 Simple Sampling vs. Importance Sampling

2.2.1 Simple Sampling

One of the simplest and most effective uses for MC method is the evaluation of definite integrals which are intractable by analytical techniques. For simplicity, we wish to calculate the one-dimensional integral

$$I = \int_a^b f(x)\,dx \tag{2.1}$$

The simple sampling Monte Carlo method gives an estimate value of this integral by choosing n points x_i randomly from the interval [a,b] with a uniform distribution

$$I \cong \frac{b-a}{M} \sum_{i=1}^{M} f(x_i) \tag{2.2}$$

Here we actually approximate the average of the function $f(x)$ to be

$$\langle f(x) \rangle \cong \frac{1}{M} \sum_{i=1}^{M} f(x_i) \tag{2.3}$$

The error for this estimate is $O(1/\sqrt{M})$, the convergence is very slow. Also, simple sampling will only be approximate for functions that are relatively smooth. Any sharp peak in the f value will probably be missed by the simple MC method. Obviously, it would be more efficient to sample the function at points where the main contribution comes from. This leads to the development of *importance* sampling Monte Carlo method.

2.2.2 Importance Sampling

The importance sampling Monte Carlo method involves the use of a weight function $p(x) > 0$ such that

$$\int_a^b p(x)\, dx = 1 \tag{2.4}$$

It follows that

$$I = \int_a^b f(x)\, dx = \int_a^b \frac{f(x)}{p(x)} p(x)\, dx \tag{2.5}$$

We may choose the points x_i according to the measure $p(x)dx$, instead of uniformly. The average of the function $f(x)$ is then

$$\langle f(x) \rangle \cong \frac{1}{M} \sum_{i=1}^{M} \frac{f(x_i)}{p(x_i)} \tag{2.6}$$

Computing the variance one obtains

$$\sigma^2 = \int_a^b \left[\frac{f(x)}{p(x)}\right]^2 p(x)\,dx - \left[\int_a^b \frac{f(x)}{p(x)} p(x)\,dx\right]^2 \tag{2.7}$$

To make the variance as small as possible, we may choose

$$p(x) \cong \frac{|f(x)|}{\int_a^b |f(x)|\,dx} \tag{2.8}$$

At this point we have arrived at the idea of *importance sampling*.

For a real thermal system with phase space $\mathbf{X}$ governed by the Hamiltonian $H(\mathbf{X})$, the average value of an observable as a function of temperature T , $\langle A(\mathbf{X})\rangle$ is given by

$$\langle A(\mathbf{X})\rangle_\beta = \frac{1}{Z}\int_{-\infty}^{\infty} A(\mathbf{X}) e^{-\beta H(\mathbf{X})}\,d\mathbf{X} \tag{2.9}$$

where β=$1/k_BT$. Z is the normalization factor for the canonical ensemble known as the *partition function*

$$Z = \int_{-\infty}^{\infty} e^{-\beta H(\mathbf{X})}\,d\mathbf{X} \tag{2.10}$$

Now, according to the above procedures, we have

$$\langle A(\mathbf{X})\rangle_\beta \cong \frac{\sum_{i=1}^{M} A(\mathbf{X_i}) e^{-\beta H(\mathbf{X_i})}}{\sum_{i=1}^{M} e^{-\beta H(\mathbf{X_i})}} \tag{2.11}$$

and using the idea of importance sampling , we get

$$\langle A(\mathbf{X})\rangle_\beta \cong \frac{\sum_{i=1}^{M} [A(\mathbf{X_i}) e^{-\beta H(\mathbf{X_i})}/p(\mathbf{X_i})]}{\sum_{i=1}^{M} [e^{-\beta H(\mathbf{X_i})}/p(\mathbf{X_i})]} \tag{2.12}$$

Choosing

$$p(\mathbf{X_i}) = \frac{1}{Z} e^{-\beta H(\mathbf{X_i})} \tag{2.13}$$

i.e. the equilibrium distribution, the variance, which we want to reduce, is practically zero. At this point, the computation of the quantity $\langle A(\mathbf{X})\rangle$ then reduces to simple arithmetic averaging

$$\langle A(\mathbf{X})\rangle_\beta \cong \frac{1}{M}\sum_{i=1}^{M} A(\mathbf{X_i}) \tag{2.14}$$

How can we generate a random sample of $\mathbf{X_i}$ which are distributed according to $p(\mathbf{X})$?

2.3 The Metropolis Algorithm

2.3.1 Metropolis Algorithm

Metropolis[5] etal. put forward the idea of using a *Markov Chain* such that starting from an initial state $\mathbf{X_0}$ further states are generated which are ultimately distributed according to $p(\mathbf{X})$, i.e. $p(\mathbf{X})$ tends to $p_{eq}(\mathbf{X})$ as $M \to \infty$. In order that the Markov process converges to $p_{eq}(\mathbf{X})$, the transition rate (the probability of transition from point $\mathbf{X}_i$ to point $\mathbf{X}_j$ in phase space) $W(\mathbf{X}_i \to \mathbf{X}_j)$ must satisfy the *detailed balance* condition

$$p_{eq}(\mathbf{X}_i)W(\mathbf{X}_i \to \mathbf{X}_j) = p_{eq}(\mathbf{X}_j)W(\mathbf{X}_j \to \mathbf{X}_i) \tag{2.15}$$

Then from Eqs.(2.13) and (2.15)

$$\frac{p_{eq}(\mathbf{X}_i)}{p_{eq}(\mathbf{X}_j)} = \frac{W(\mathbf{X}_j \to \mathbf{X}_i)}{W(\mathbf{X}_i \to \mathbf{X}_j)} = e^{-\beta\Delta H} \tag{2.16}$$

where ΔH is the energy change ($H(\mathbf{X}_i)$ - $H(\mathbf{X}_j)$). The choice of $W(\mathbf{X}_i \to \mathbf{X}_j)$ is not unique. A convenient one is

$$W(\mathbf{X}_i \to \mathbf{X}_j) = \begin{cases} e^{-\beta\Delta H} & \text{if } \Delta H > 0 \\ 1 & \text{if } \Delta H \leq 0 \end{cases} \tag{2.17}$$

So, The Metropolis algorithm is very simple to program

(1) Specify an initial point $\mathbf{X}_0$ in phase space.

(2) Generate a new state $\mathbf{X}'$.

(3) Compute the energy change ΔH

(4) Generate a uniform random number $R \in$[0,1].

(5) If $\Delta H < 0$, accept the new state and return to step (2).

(6) Otherwise, if $\Delta H > 0$, then calculate $e^{-\beta \Delta H}$, if it is larger than R, accept the new state and return to step (2); otherwise retain the old configuration as the new one and return to step (2).

Note that the Metropolis algorithm does not specify how the changes to the configuration should be made, it just says that any proposed change to the system should be accepted with a certain probability that depends on the change in energy.

How the changes are made depends on the variables and the model being studied. The only constraints on the update procedure are :

(1) It should be *ergodic* , i.e. every configuration can be reached from every other configuration in a finite number of iterations.

(2) The transition probability $W(\mathbf{X}_i \rightarrow \mathbf{X}_j)$ satisfy the detailed balance condition.

2.3.2 Metropolis Algorithm for the Ising Model

For the Ising model, governed by the Hamiltonian

$$H = -J \sum_{<ij>} S_i S_j \tag{2.18}$$

where the S takes the values ± 1. $< ij >$ denotes that spin S_i has only S_j as nearest neighbors and vice versa. J is the exchange interaction. For this model, the obvious change in the configuration is to try to update (or 'flip') a spin, i.e. flip the sign (

or direction) of the spin variable. ΔH here depends only on the spin values at the site and its nearest neighbors, i.e.

If $\Delta H \leq 0$, we make the proposed change.

If $\Delta H > 0$, we make the change with probability $e^{-\beta \Delta H}$.

The Ising model is a very important model in statistical physics. It displays the phenomenon of a second order *Phase Transition*. Phase Transitions are classified in part by their *order*:

• First order: discontinuity in order parameter or energy (i.e. the first derivative of the partition function).

• Second order: divergence in the susceptibility or specific heat (i.e. the second derivative of the partition function).

etc.

2.4 The Monte Carlo Damage Spreading Technique

The Monte Carlo Damage Spreading (MCDS) technique, i.e. measuring the Hamming distance between two different initial configurations as they evolve in time as explained in the next chapter, was first studied in theoretical biology in the context of genetic evolution[6]. Later the MCDS concept found its way into the simulations of physical systems[7]-[16]. In this method one essentially monitors the time evolution of two or more copies of the same system with different initial configurations subject to a specific dynamics and to the same thermal noise (i.e. same random number sequence). It turns out that this method is less sensitive to the static fluctuations, when compared to the conventional Monte Carlo method where the time evolution of a single copy is investigated. The MCDS method has been successfully applied to many magnetic models, like cellular automata, Ising ferromagnet, P-state clock, Potts, ANNNI(Axial Next-Nearest Neighbor Ising), Ashkin-Teller,

discrete N-vector, XY, the Heisenberg, and spin glasses. Besides its wide variety of applications, the relationship between damage spreading and the time-dependent thermodynamic properties in the Ising model[17], the possible connection of damage transition (where the damage vanishes) and the percolation transition of geometrical clusters of correlated spins [18]-[20] are also investigated.

Most of the above systems to which the damage spreading technique have been applied are the systems with the second order phase transition. Also, the MCDS technique has been used to study the critical properties of the BEG model on a honeycomb lattice in the vicinity of tricritical line and showed how the MCDS technique may be applied to identify the tricritical point[21]. For the q-state Potts model on square lattice the MCDS studies also showed that it is possible to calculate the critical temperature of the model as well as to give some indication of the order of the phase transition[22]. MCDS technique represents nowadays an important tool in the study of the dynamic as well as the static behavior in magnetic systems.

In the next chapter, we will use the MCDS technique to study several magnetic spin models.

2.5 References

[1] K.Binder, D.W. Heermann. Monte Carlo Simulation in Statistical Physics: an introduction. Berlin: Springer-Verlag. 1988.

[2] D.W. Heermann. Computer Simulation Method in Theoretical Physics. 2nd edition. Berlin: Springer-Verlag. 1990.

[3] D.P. Landau, K.Binder. A guide to Monte Carlo Simulations in Statistical Physics. Cambridge University Press. 2000.

[4] J.M.Yeomans. Statistical Mechanics of Phase Transitions. Oxford University Press. 1992.

[5] N. Metropolis, A.W. Rosenbluth, M.N. Rosenbluth, A.H. Teller, E. Teller, J.Chem. Phys. 21,1087(1953).

[6] S.A.Kauffman, J.Theor.Biol. **22**, 437(1969).

[7] N.Jan, L.de Arcangelis, Annu.Rev.Comput.Phys. **1**, 1(1994), World Scientific, Singapore ; and references therein.

[8] H.J. Herrmann, 56(1989), Computer Simulations in Condensed Matter Physics II eds. D.P. Landau, K.K. Mon and H.B. Schüttler(Berlin:Springer).

[9] F.G.B. Moreira, A.J.F. de Souza,A.M. Mariz, Phys. Rev. E **53** 332(1996).

[10] A.A. Júnior, F.D. Nobre, Physics A **243** 58(1997).

[11] P. Grassberger, J.Phys A **547** 214(1995); U. Gropengiesser, Physica A **215** 308(1995); F. Wang, N. Hatano, M.Suzuki, J. Phys. A **28**4543(1995); T. Vojta, M. Schreiber, Phys. Rev. E **58** 7998(1998).

[12] E.S. de Sousa, A.M. Mariz, F.D. Nobre, U.M.S. Costa, Physica A **241** 469(1997).

[13] L. da Silva, F.A. Tamarit, A.C.N. de Magalhães, J. Phys. A **30** 2329(1997).

[14] J.A. Redinz, F.A. Tamarit, A.C.N. de Magalhães, Physics A **255** 439(1998).

[15] M.N. Barber, B. Derrida, J. Stat. Phys. **51** 877(1988).

[16] O. Golinelli, B. Derrida, J. Phys. A **22** L939(1989).

[17] C. Glotzer, P.H. Poole, N.Jan, J. Stat.Phys. **68** 895(1992).

[18] G.M. Zhang, C.Z Yang , Europhys. Lett. **22** 505(1993).

[19] L.de Arcangelis, A. Coniglio, F. Peruggi, Europhys. Lett. **14** 515(1991).

[20] M. Nicodemi, Physica A **238** 9(1997).

[21] U.M.S. Costa, I.V.Rojdestvenski, Phys. Lett. A **231** 128(1997).

[22] M.F. de A. Bibiano, F.G. Brady Moreira, A.M. Mariz, Phys. Rev. E **55** 1448(1997).

Chapter 3

The Monte Carlo Damage Spreading (MCDS) Studies of Some Two-Dimensional Magnetic Spin Models

3.1 The Monte Carlo Damage Spreading Technique

3.1.1 A Metropolis-Type Dynamics

The numerical simulations are implemented on a square lattice with N spins and linear size $L(N = L^2$ sites) submitted to periodic boundary conditions. A configuration of lattice spins at Monte Carlo time t is

$$C(t) = \{S_i(t)\} \qquad i = 1, 2, 3...N \tag{3.1}$$

The spin variable, S_i, assumes values -S,-S+1, ... , S-1, S where S is either a positive integer or a non-negative integer plus a half. In order to make a configuration $C(t)$ evolve in time, we use the following dynamics:

During each time interval $\delta t = 1/N$, one spin site i is chosen randomly. The spin value $\Delta_i(t + \delta t)$ at time $t + \delta t$ is then chosen as

$$\Delta_i(t+\delta t) = \begin{cases} -S & 0 \le Z_{i1}(t) < 1/(2S+1) \\ -S+1 & 1/(2S+1) \le Z_{i1}(t) < 2/(2S+1) \\ ..... & ..... \\ S-1 & (2S-1)/(2S+1) \le Z_{i1}(t) < 2S/(2S+1) \\ S & 2S/(2S+1) \le Z_{i1}(t) < 1 \end{cases} \tag{3.2}$$

where $Z_{i1}(t)$ is a uniform random number, $0 \leq Z_{i1}(t) \leq 1$.

One then updates the spin according to the following dynamics rule

$$S_i(t+\delta t) = \begin{cases} \Delta_i(t+\delta t) & P_i(t) \geq Z_{i2}(t) \\ S_i(t) & \text{otherwise} \end{cases} \tag{3.3}$$

and $S_j(t+\delta t) = S_j(t)$ for $j \neq i$, where

$$P_i(t) = e^{-\Delta H_i/T} \tag{3.4}$$

$$\Delta H_i = H\{\Delta_i(t+\delta t)\} - H\{C(t)\} \tag{3.5}$$

where $0 \leq Z_{i2}(t) \leq 1$ is another uniform random number, T is the temperature of the system in unit of J/K_B, K_B is the Boltzmann constant.

3.1.2 Damage Spreading Technique

Now, we consider two different initial configurations $C^A(0) = \{S_i^A(0)\}$ and $C^B(0) = \{S_i^B(0)\}$ at time $t = 0$, and let them evolve in time according to the same above dynamics rule with the same sequence of random numbers for updating the spins. Then two configurations $C^A(t)$ and $C^B(t)$ at time t are computed through the following Hamming Distance (or Damage) between them

$$D(t) = \frac{1}{N}\sum_{i=1}^{N}[1 - \delta(S_i^A(t), S_i^B(t))] \tag{3.6}$$

where $\delta(,)$ is the Kronecker delta symbol. Physically $D(t)$ measures the fractions of the spins which differ in the two replicas at time t. In calculations, we average $D(t)$ over many samples. The average distance is

$$\langle D(t)\rangle = \frac{1}{N_s}\sum_{j=1}^{N_s} D_j(t) \tag{3.7}$$

where $D_j(t)$ is the damage distance for the jth independent trial, N_s is the number of independent sample, the sum is over all trials. Also here, we may average the $D_j(t)$ over only those samples which have survived (i.e. such that $C^A(t) \neq C^B(t)$), since one may regard those samples whose $D(t) = 0$ at low temperature as the 'bad' ones and hence exclude them.

We also study the 'Damage Susceptibility '

$$\sigma_{D(t)} = \sqrt{\langle D^2(t) \rangle - \langle D(t) \rangle^2} \tag{3.8}$$

which measures the fluctuations of damage $D(t)$. This quantity will provide a set of information to characterize different phases of the system, and is very sensitive to the phase transition.

We will investigate a quantity which we define it as the ratio of $N_{S_i=c}$ (number of spins whose spin S_i takes one specified value c $\in$ (-S, -S+1, ... , S-1, S) to N at the equilibrium state. In order to decrease the fluctuations, we take an average over those two replicas (configuration A and B)

$$\langle P_{S_i=c} \rangle = \frac{1}{N_s} \sum_{k=1}^{N_s} [\frac{N^A_{S_i=c} + N^B_{S_i=c}}{2N}]_k \tag{3.9}$$

$\langle P_{S_i=c} \rangle$ depends on the temperature, time , initial conditions and the noise. $\langle\rangle$ in (3.9) denotes an average over many samples. This quantity can show us the detailed spin configurations.

Those three quantities $\langle D(t) \rangle$, $\sigma_{D(t)}$ and $\langle P_{S_j=c} \rangle$, together with temperature, initial condition and any other parameters, will lead to information about the criticality of the system.

3.1.3 Finite Size Scaling

In the context of MCDS studies, in order to obtain a more reliable estimate for the dynamical (second order) phase transition temperature, we use the finite-size scaling procedure [1]. For each sample s, we calculate the distance $D_s(t)$ at times t=1,2,3... . The characteristic time τ_1 (a measure of time for two configurations to meet) and characteristic square time τ_2 are defined as

$$\tau_1(L,T,s) = \sum_t tD_s(t) / \sum_t D_s(t) \tag{3.10}$$

$$\tau_2(L,T,s) = \sum_t t^2 D_s(t) / \sum_t D_s(t) \tag{3.11}$$

At the transition temperature, one expects for τ_1 the following scaling form valid for large L and T close to T_c:

$$\tau_1(L,T,s) \sim u(L) f_1(v(L)(T-Tc), s) \tag{3.12}$$

$u(L)$ gives the size dependence at $T = T_c$ (for an ordinary second order phase transition, $u(L)$ and $v(L)$ are power laws). One expects for τ_2 that

$$\tau_2(L,T,s) \sim u^2(L) f_2(v(L)(T-Tc), s) \tag{3.13}$$

and since τ_2 is a measure of the squared characteristic time, one expects that the ratio should be independent of lattice size L at the dynamical transition T_c:

$$R(L,T,s) = \tau_2(L,T,s)/\tau_1^2(L,T,s) \sim f_3(v(L)(T-Tc), s) \tag{3.14}$$

Average over many samples, one gets

$$\langle R(L,T,s) \rangle = \langle \tau_2(L,T,s)/\tau_1^2(L,T,s) \rangle \sim g(v(L)(T-Tc)) \tag{3.15}$$

This means that for large L, all the curves $\langle R \rangle$ plotted as function of T for different L should cross at the same temperature T_c, i.e. the dynamical critical temperature when $L \to \infty$.

In the following simulations, we employ the widely used *Power Residue Method* to generate a sequence of pseudo random number, which has both a long period and good statistical properties (e.g. see [40]).

3.2 The S=1/2 and S=1 Ising Spin Models

We first consider Eq.(2.18), the usual Ising spin model. $J > 0$ is the (ferromagnetic) exchange interaction coefficient. For the standard $S = 1/2$ Ising model, S_i=$\pm$1; For $S = 1$ Ising model, S_i=0,$\pm$1.

In the following calculations, we average the $D_j(t)$ over only those samples which have survived. Three kinds of initial conditions are chosen:

IC1: $C^A(0) = \{+1\}$, and $C^B(0)$=$\{-1\}$ for all i. So from Eq.(3.6), $\langle D(0) \rangle$=1.

IC2: $C^A(0)$ is random, and $C^B(0)$=$-C^A(0)$ for all i. So, $\langle D(0) \rangle$=1.

IC3: $C^A(0)$ and $C^B(0)$ are random and independent. So, $\langle D(0) \rangle$=1/2 (S =1/2 model) and $\langle D(0) \rangle$=2/3 ($S = 1$ model).

Fig. 3.1 is the calculation results for S=1/2 and 1 models. In Fig.3.1(a) and (b), the results are averaged over 1000, 500 and 100 samples for L=10, 20 and 40, respectively. Similar to other dynamics approaches, we can see that two temperature regimes exist for both models where a sharp dynamical phase transition (or damage spreading transition), with $k_B T_D/J \cong$2.4 and 1.8 the respective dynamical transition temperatures for S=1/2 and S=1 models can be observed in our dynamics. In both figures, at the maximum $\sigma_{D(t)}$ point (the magnitude of $\sigma_{D(t)}$ of other points are smaller than this point) with L=40, IC1 and t=6000, we estimate (run for several different random number sequences) the transition temperature $k_B T_\sigma/J$ to be

2.30±0.05 and 1.70±0.045, respectively, for these two models. The standard errors (error bars) are less than the size of symbols.

For the S=1/2 Ising model, Neumann and Derrida [1] applied finite-size scaling with heat bath dynamics to this model and got the dynamical phase transition temperature as $k_BT_D/J \cong 2.25 \pm 0.05$, which is consistent with the corresponding exact static transition temperature k_BT_c/J=2.269. Fig.3.1(c) is our finite size scaling results for the S=1 model within our dynamics. The standard errors (error bars) are less than the size of symbols. We calculate $\langle R \rangle$ averaged over 1500, 800 and 200 samples against T for L=10, 20 and 40, respectively, using IC2 (other initial conditions may also be used. The shapes will be a little different, but the estimates for the transition temperature should be close to this one). Our estimate of T_c for S=1 Ising model is $k_BT_c/J \cong 1.675 \pm 0.025$. This result is consistent with the static case as 1.693 [2] or 1.693559 [3], etc.

Fig.3.1(d) is the simulation result of $\langle P_{S_j=0} \rangle$ -T relationship for the S=1 model with IC1 averaged over 200 samples at t=6000. $\langle P_{S_j=0} \rangle$ increases as the temperature increases, and its S-like shape is very similar to the exact U - T relationship for the standard Ising $S = 1/2$ model, U is the internal energy. Actually, $\langle P_{S_j=0} \rangle$ can indeed reflect the internal energy U. We can see that there exists an inflection point in this relationship curve. At the maximum standard deviation point (the magnitude of standard deviations of other points are smaller than this point), we estimate the transition temperature to be 1.70±0.055. This point is just the inflection point of the curve and also corresponds to the static phase transition point of the model. The standard errors (error bars) are less than the size of symbols.

3.3 The Mixed Spin Ising Model

3.3.1 The Mixed Spin Ising Model

The mixed spin Ising system is relevant for understanding bimetallic molecular ferrimagnets that are synthesized in search of stable, crystalline materials, with spontaneous magnetic moments at room temperature[38].

Here, we will use the MCDS technique to study a mixed spin Ising model [MSIM] on the square lattice in which two inter-penetrating sub-lattices have spins one half ($\pm 1/2$) and spins one (± 1,0). We consider a mixed spin Ising model on the square lattice given by the Hamiltonian

$$H = -J \sum_{<ij>} \sigma_i S_j + G \sum_j S_j^2 \tag{3.16}$$

where the S_j takes the values ± 1 or 0 and are located in alternating sites with spins $\sigma_i = \pm 1/2$. We choose to put the factor of $1/2$ into the interaction parameter. Each spin S has only σ as nearest neighbors and vice versa. The first summation is carried out only over nearest neighbor pairs of spins, the second summation only runs over all sites of S sub-lattice. J is the exchange interaction, G is called the crystal field interaction parameter.

Mixed spin systems provide good results for studying ferrimagnetism. The magnetic properties of the mixed Ising models have been studied by high-temperature series expansions[22], renormalization group(RG)[23, 24, 25], mean field[26], effective field[27, 28, 17], Monte Carlo simulations and numerical transfer matrix calculations[30, 31] and the free-fermion approximation[33]. Besides at equilibrium conditions as stated as above, within mean field approach, the kinetics of the model in the presence of a time-dependent oscillating external field, has been studied[34].

Among those works, there exist two opposite conclusions for the mixed spin Ising model on the square lattice: one RG analysis[23], effective field theory with correlations[29], and mean filed theory[26] indicate that there exists a compensation point or tricritical point at finite temperature; another RG scheme[24], MC and numerical transfer matrix techniques[30, 31] then got a contradictory conclusion. Here, the MCDS technique is also applied to study the MSIM on the square lattice. We found that the mixed spin Ising model may have a tricritical point at finite temperature.

A configuration of lattice spins at time t is

$$C(t) = \{\sigma_i(t), S_j(t)\} \qquad i, j = 1, 2, 3...N/2 \tag{3.17}$$

In the following calculations presented here, we take $J > 0$ (ferromagnetic interaction), the initial configuration is chosen to be

$$C^A(0) = -C^B(0) = \{1\} \qquad \forall\, i, j \tag{3.18}$$

where we have assumed that there are no zero values in both S^A and S^B sub-lattices at t=0, i.e. $\langle D(t)\rangle$=1 . Similarly, if we take $J < 0$(anti-ferromagnetic), i.e. the mixed Ising ferrimagnetic model, the initial condition could be chosen as: spins in the S sub-lattice to be +1, spins in the σ sub-lattice to be -1 in configuration A, spins in configuration B then keep opposite to A.

Results for MSIM with G=0

We first study the 'pure' mixed spin Ising model with zero crystal field interaction. For this model, high-temperature series expansion[35], RG[23, 25], the equiscale transformation[36], etc. have shown this model belongs to the same universality class as the standard $\sigma = 1/2$ Ising ferromagnetic model.

In our MCDS procedure, the simulations have been performed for four lattice size. The results are averaged over 1500, 800, 400 and 180 samples for L=10,20, 30 and 40, respectively. Fig.3.2. shows the $\langle D(t)\rangle$ as a function of temperature and the time. We know that equilibrium is reached at all temperature except in the critical region where finite-size and finite-time effects can be seen. The shape of $\langle D(t)\rangle$ in Fig.3.2 is very similar to the standard Ising model studied by the DS technique within the heat bath dynamics and the same initial condition (Chap.2 [15]). For the standard Ising model, within the heat bath dynamics and the initial condition(3.17), it has been proved that the damage distance $\langle D(t)\rangle$ is equivalent to the order parameter, the average magnetization of the system at time t[1].

We clearly observe two distinct regions in Fig.3.2 (i) a low-temperature region ($T < T_D, T_D \cong 2.0$) where $\langle D(t)\rangle$ does not vanish for all cases; (ii) a high-temperature region ($T \geq T_D$), where $\langle D(t)\rangle$ vanishes for all system sizes and time t. Two distinct temperature regions divided by a damage spreading transition temperature $k_B T_D/J$ are believed to denote the corresponding static continuous phase transition. The damage spreading features in Fig.3.2 have been observed in most of the Ising-like systems.

We observed in the calculations that the finite-time effect for t=1000 and t=2000 is relatively small for our chosen initial condition, we will assume that systems have reached their equilibrium states at t=1000 for the chosen initial condition (3.17). We only present our calculation results at t=1000.

In view of the temperature dependence of the fluctuation $\sigma_{D(t)}$, our simulation shows that there is an almost null fluctuation in the low- and high-temperature regions, except near the damage spreading transition temperature $k_B T_D/J$ where it rises abruptly. Fig.3.3 shows the $\sigma_{D(t)}$ as a function of temperature for four system sizes.

From the maximum values of $\sigma_{D(t)}$, we may locate the phase transition temperature k_BT_σ/J. We estimate (run for several different random number sequences) $k_BT_\sigma(L)/J$ to be 1.90±0.05, 1.99±0.04, 2.02±0.05 and 2.02±0.03 for L=10, 20, 30 and 40, respectively. From those data, we get a more accurate estimate for the damage spreading (dynamical phase transition) temperature than k_BT_D/J to be $k_BT_\sigma/J \cong 2.02$ for this model.

In order to obtain a more reliable estimate for this transition temperature, we use the finite size scaling procedure. In Fig.3.4 we plot $\langle R\rangle$ averaged over 1500, 800, 400 and 180 samples against k_BT/J for L=10, 20, 30 and 40, respectively. Our estimate of k_BT_c/J for this mixed Ising ferrimagnetic model with G=0 and the initial condition (3.17) is $k_BT_c/J \cong 2.00 \pm 0.01$. This result is close to $k_BT_\sigma/J = 2.02$ from $\sigma_{D(t)}$ and also consistent with its static transition temperature at 1.9569 [33], or 2.016±0.078 [35].

We may use this method to estimate the dynamical critical exponent z defined at the dynamical critical temperature k_BT_c/J by $\tau \sim L^z$, where L is the linear size and τ is the relaxation time for the dynamics[1]. Near the critical temperature, the fluctuations are very strong, and unlike the standard Ising model we have no exact solution of k_BT_c/J for this model. Therefore we expect rather large error bars in the estimate of the critical exponent z. We may use τ_1 in Eq.(3.10) to measure the average vanishing time at k_BT_c/J and repeat the simulations 40 times on different sizes L=10, 20, 30 and 40. z is the slope of the curve of $\ln(\langle\tau_1\rangle)$ versus ln(L). In Fig.3.5 we have estimated z with the initial condition (3.17) for this 'pure' MSIM to be

$$z = 2.65 \pm 0.26 \quad (k_BT_c/J = 2.00) \tag{3.19}$$

RESULTS FOR MSIM WITH $G \neq 0$

We choose several values of G to study by DS procedure. In the following calculations, we take the parameters to be L=40, t=1000 and N_s=200. Fig.3.6 shows the results of $\langle D(t) \rangle$ as a function of k_BT/J and G/J.

We may observe a completely different behavior of $\langle D(t) \rangle$: for $G/J \leq 3.0$, the behavior of $\langle D(t) \rangle$ are very similar to the previous G=0 case(the G=0 result is also presented in the figure), there exist Ising-like continuous phase transition for the model for those G values; for $G/J > 3.0$, contrary to the $G/J \leq 3.0$ cases, $\langle D(t) \rangle$ are zero for all temperature regions. For the low temperature (e.g. k_BT/J=0.1), when G changes from 3.0 to 3.01, the $\langle D(t) \rangle$ 'jumps'from 1 to 0. From Fig.3.6 we may estimate the approximate(continuous) dynamical transition temperature k_BT_D/J to be 2.55, 2.5,2.25, 2.2, 1.9 and 1.45 for G/J=-6.0, -3.0, -1.0, 0.0, 2.0 and 3.0, respectively.

In Fig.3.7, we plot the $\sigma_{D(t)}$ curves. Similar things as in Fig.3.6 can be observed: for $G/J \leq 3.0$, peak-like curves of $\sigma_{D(t)}$ can be seen and they are the features of second order transition; for $G/J >$3.0, $\sigma_{D(t)}$=0 for all temperature regions. We may get more accurate (continuous) dynamical transition temperatures than k_BT_D/J to be k_BT_σ/J=2.3±0.035, 2.25±0.04, 2.19±0.035, 2.02±0.03, 1.62±0.04 and 1.26±0.02 for G/J=-6.0, -3.0, -2.0, 0.0, 2.0 and 3.0, respectively. Similarly, we may use the same finite size scaling procedure to get the improved dynamical transition temperature results.

The interesting features of $\langle P_{S_j=0} \rangle$ in S sub-lattice as a function of k_BT/J and G/J are plotted in Fig.3.8. We can also see there exist two different regions for G/J values: (i) $G/J \leq$3.0, the $\langle P_{S_j=0} \rangle$ curves are very similar to the G=0 S-like curve. There exist continuous phase transitions within those G/J values. In the limit of $G \to -\infty$, this model is reduced to the standard Ising model. S and σ can only take

+1 or -1 values; (ii) $G/J \geq 3.01$, contrary to the $G/J \leq 3.0$ cases, $\langle P_{S_j=0} \rangle$ decreases as the temperature increases. In the limit of $G \to +\infty$, this model reaches a new phase which we may call it the staggered quadrupolar phase, similar to a phase in the BEG model[37]. In this phase, S sub-lattice has S_j=0 at every site and the σ sub-lattice has sites occupied randomly by σ_i=+1 or -1. This phase can be reached at low temperature k_BT/J=0.1 and G/J=5.0 as shown in Fig.3.8 in our DS dynamics approach.

We may explain the behavior of this model as follows. In this model, we only consider the nearest-neighbor interaction between S and σ spins. When G becomes large, the probability for S sub-lattice spins to take the zero values increases, the interaction of the total system becomes weak, and the second order phase transition temperature also becomes small. However, when the interaction of the system is too small, it can not support the long range order of the system, i.e. there is no continuous phase transition. We may analyze this problem from another angle. We regard the S_j=0 state as a 'hole', then the S sub-lattice are occupied by $\sigma = \pm 1$ and the holes. Parameter G can change the relative number of σ spins and the holes in the S sub-lattice (it has the meaning of chemical potential). When $G \to -\infty$, there is no hole in the S sub-lattice, both sub-lattices are occupied by σ spins, corresponding to the standard Ising model. When G increases, the number of holes increases. When $G \to +\infty$, the S sub-lattice are all occupied by S_j=0 spin states. In the equilibrium state, for G changing between $-\infty$ and $+\infty$, the holes can move and have a tendency to gather to form clusters in order to make the system stable. When G increases to a critical value, the σ spins can no longer form infinite clusters, then there is no long range order and no continuous phase transition. However, the finite σ spin clusters and the formation of the equivalent 'hole clusters' can support a first order phase transition for the system. Here, the so-called 'hole cluster' means: the spins of the S sub-lattice within a hole cluster are all occupied by hole (S_j=0), although

the σ spins occupy the σ sub-lattice within a hole cluster, they have no interactions among them, it is equivalent to the cluster which is completely composed of holes. The configuration of spins can verify this point.

According to our DS results, we may schematically plot the finite-temperature phase diagram for this model, and use k_BT_σ/J obtained from the $\sigma_{D(t)} - T$ relationship in Fig.3.9 as the (second order) phase transition temperature. In Fig.3.9, the general shape of the phase diagram shows reasonable agreement between our results and the Monte Carlo simulations[30], except for the range of $G/J > 3.01$ where the first order transition could occur in our DS approach. ¿From our data, we estimate the tricritical point (white square in Fig.3.9) to be (k_BT_{tri}/J , G_{tri}/J)=(1.26$\pm$0.02, 3.00). The estimated static values for the tricritical point for this mixed spin Ising model on the square lattice are (1.232, 4.198)[23] and (0.9936, 3.9376)[32], etc.

We have also performed the same calculations for the $J < 0$ mixed Ising ferrimagnetic model (using the initial condition stated below Eq.(3.17)), and very similar features have been obtained. Therefore, we expect there exist both second and first order phase transition for this mixed spin Ising model on the square lattice depending on the G values.

We should point out that, unlike the conventional criteria for a first order transition, the damage spreading results here seem not to give us explicit evidence for the first order transition, such as an obvious discontinuity for the order parameter. In Fig.3.10, we calculate one thermodynamic order parameter, the total magnetization of the system using the same initial condition of Eq.(3.17) (we take an average over A and B configurations). Its behavior is quite similar to the $\langle D(t)\rangle - T$ relationship. We do not observe the obvious discontinuity or 'jump' for $\langle|M(t)|\rangle$, $\langle D(t)\rangle$ or $\langle P_{S_j=0}\rangle$ at the tricritical point G/J =3.0 where we regard it as the meeting point of the second order and the first order transition lines , even if we may claim that at

$G/J = 3.0$ those three quantities have had the largest 'jump' in the critical region when compared to other $G/J < 3.0$ cases as seen in Figs.6, 8 and 10.

Here, we conclude the existence of a tricritical point for the mixed spin Ising model due to its very similar behavior to the S=1 Blume-Capel model, where its tricritical behavior is well-known (see next section). The S=1 Blume-Capel model on the square lattice where only one spin variable S_i takes 0, or ± 1 for each lattice site has the same form of the Hamiltonian as in Eq.(3.15). For the S=1 Blume-Capel model, we got quite the same shapes and features for those quantities, $\langle D(t) \rangle$, $\sigma_{D(t)}$ and $\langle P_{S_j=0} \rangle$ as the mixed spin Ising model, except at the tricritical point (i.e. above meeting point), an obvious discontinuity or 'jump' of $\langle D(t) \rangle$ and $\langle P_{S_j=0} \rangle$ can be observed for the S=1 Blume-Capel model. Also, the estimated dynamical tricritical point for this Blume-Capel model by DS technique is in excellent agreement with other approaches. Unlike the S=1 Blume-Capel model, we can not observe an obvious discontinuity at the tricritical point in the mixed spin Ising model because there is only one S=1 *sub-lattice* for this model. Because of the small discontinuity in the mixed spin Ising model, we may also name this first order transition the 'weak' first order transition. A similar case may refer to the q-state Potts model (e.g. q=5,6, etc.)[39]. We also expect the results could be improved when system size L is increased. This simple but fruitful model, the behavior of which is not yet well established, would be worthy of further studies.

3.4 The Blume-Capel Model

3.4.1 The Blume-Capel Model

The $S = 1$ Blume-Capel model was originally proposed to study the first-order phase transition in magnetic systems[4, 5] and has also been used in describing $He^3 - He^4$ mixtures[6]. The Hamiltonian can be written as

$$H = -J \sum_{<ij>} S_i S_j + G \sum_i S_i^2 \tag{3.20}$$

The first summation is carried out only over nearest neighbor pairs of spins, the second summation runs over all sites of a square lattice. $J > 0$ is the ferromagnetic exchange interaction between nearest neighbor spins, G is the single spin anisotropy parameter. The S=1 case has been extensively studied by a variety of methods such as mean field[4, 5], variational methods[7], constant coupling approximation[8], Monte Carlo simulations[9, 10], transfer matrix[11], renormalization- group[12, 13], finite-size scaling based on transfer matrix[14], etc. It is well established that for dimension $d \geq 2$, the S=1 Blume-Capel model exhibits a line of continuous phase transition (Ising type), a line of first-order phase transitions and a tricritical point where those two lines meet.

For values of spin $S > 1$, however, the situation is quite unclear and fewer results are available. For the S=3/2 case, the mean-field calculation[15], correlated effective-field treatment[16], differential operator technique[17], finite-size scaling based on transfer matrix[14] and conventional equilibrium Monte-Carlo simulations[18, 19] indicate a second-order phase transition with no tricritical point and a separated first-order transition line which terminates in an isolated multi-critical point. In contradiction with these results, a renormalization group calculation[13] presents a unique first-order transition line at low temperature which terminates in the second-order transition line at a tetra-critical point. Similar results are also obtained by finite size renormalization group calculations[20] and other conventional equilibrium Monte Carlo simulations[21].

In the following section, the MCDS technique is also applied to study the Blume-Capel model on the square lattice. Our results show that for the integer S=1 and 2 Blume-Capel model, there exist a multi-critical point at low temperature which is

not present for the half-integer S=3/2 and 5/2 spin models. For the controversies surrounding the S=3/2 Blume-Capel model, the MCDS method allows us for the first time to distinguish definitely between the two conflicting scenarios discussed in the literature.

3.4.2 MCDS results for the Blume-Capel Model

In the following calculations presented here, the initial configuration is chosen to be

$$C^A(0) = -C^B(0) \neq 0 \qquad \forall\, i \tag{3.21}$$

i.e we choose $\langle D(t)\rangle = 1$. For example, for the S=2 case, we may choose $C^A(0) = -C^B(0) = \{2\}$, or , $C^A(0) = -C^B(0) = \{1\}$; Those two choices will not alter the features of the calculation results. The calculations could have been done starting with other initial conditions, e.g. two random initial configurations, but in this case, the equilibrium of the system needs longer to be established at low temperature, however the results would be also very similar[41].

We choose several values of G to study by our DS procedure. The simulations have been performed for system size L=40, t=1000 and the results are averaged over N_s=200 samples. We observed that the finite-time effect for $t = 1000$ and $t = 2000$ is relatively small for our chosen initial condition. In the following calculations, we will assume the systems have reached their equilibrium states at $t = 1000$ for the chosen initial condition of Eq.(3.19).

Results for the Blume-Capel model with S=1 and 2

We first study the Blume-Capel model with spin S=1 and initial condition $C^A(0) = -C^B(0) = \{1\}$. The results are plotted in Fig.3.11. We explain Fig.3.11 as follows. Fig.3.11(a) shows the results of $\langle D(t)\rangle$ as a function of k_BT/J and G/J. We

may observe a completely different behavior of $\langle D(t)\rangle$: for $G/J \leq 2.0$, there exist Ising-like continuous phase transitions for the model. We clearly observe two distinct regions, a low-temperature region ($T < T_D$) where $\langle D(t)\rangle$ does not vanish and a high-temperature region($T \geq T_D$) for which $\langle D(t)\rangle$ vanishes; for $G/J > 2.0$, contrary to the $G/J \leq 2.0$ cases, $\langle D(t)\rangle$ is zero for all temperature regions. For $G/J \leq 2.0$ in Fig.3.11(a), two distinct temperature regions divided by a damage spreading transition temperature k_BT_D/J are believed to denote the corresponding static continuous phase transition that has been observed in most of the Ising-like systems. From Fig.3.11(a) we may estimate the approximate (continuous) dynamical transition temperature k_BT_D/J to be 2.35, 2.3, 2.2, 2.1, 1.85, 1.55 and 0.6 for G/J=-4.0, -3.0, -2.0, -1.0, 0.0, 1.0 and 2.0, respectively. In Fig.3.11(b), we plot the temperature dependence of the fluctuation$\sigma_{D(t)}$ for our chosen G values. We have observed that: for $G/J \leq 2.0$, the simulations show that there is almost null fluctuation in the low- and high-temperature regions, except near the damage spreading transition temperature T_D where it rises abruptly; for $G/J > 2.0$, $\sigma_{D(t)}$=0 for all temperature regions. The peak-like curves of $\sigma_{D(t)}$ in the $G/J \leq 2.0$ regions are features of a second order transition, and from the maximum values of $\sigma_{D(t)}$ we may get the more accurate (continuous) dynamical transition temperatures than k_BT_D/J. We estimate (run for several different random number sequences) that k_BT_σ/J to be k_BT_σ/J=2.25±0.10, 2.20±0.12, 2.10±0.10, 1.95±0.08, 1.75±0.05, 1.45±0.01 and 0.56±0.03 for G/J=-4.0, -3.0, -2.0, -1.0, 0.0, 1.0 and 2.0, respectively. In Fig.3.11(c), the interesting features of $\langle P_{S_i=0}\rangle$ as a function of k_BT/J and G/J are plotted. We also regard $\langle P_{S_i=0}\rangle$ as an important factor to explain the multi-critical behavior for this model. We can also see there exist two different regions for those G values: for $G/J \leq$2.0, $\langle P_{S_i=0}\rangle$ increases as the temperature increases. In the limit of $G \to -\infty$, this model is reduced to the standard Ising model, and S can only take +1 or -1 values. For $G/J \geq$2.01, contrary to $G/J \leq$2.0 cases, $\langle P_{S_i=0}\rangle$ decreases as the tem-

perature increases. In the limit of $G \to +\infty$, this model reaches a phase in which S_i=0 at every site.

Similar to the mixed spin Ising model, the behavior of this $S = 1$ Blume-Capel model could also be explained as follows. In this model, we only consider the nearest-neighbor interaction between S_i spins. We regard the $S_i = 0$ state as a 'hole', then the lattice sites are occupied by either $S_i = \pm 1$ spins and the holes. The parameter G can change the relative number of $S_i = \pm 1$ spins and the holes in the system (it has the meaning of chemical potential). When $G \to -\infty$, there is no hole in the system , corresponding to the standard Ising model. When G increases, the number of holes increases, the interaction of the total system becomes smaller, the second order phase transition temperature also becomes smaller. When G increases to a critical value, the $S_i = \pm 1$ spins can no longer form infinite clusters, the interaction of the system becomes weak and can no longer support long range order of the system. Then there are no continuous phase transition, however, the clusters composed of $S_i = \pm 1$ spins and the holes can support a first order phase transition for the system. From the angle of our Metropolis-type dynamics, because of the smaller interaction (i.e. ΔH_i in Eq(3.5) approaches zero) when G is larger than this critical G value, the probability (i.e. P_i in Eq(3.4)) to accept the new proposed spin value increases quickly, and then causes $\langle D(t) \rangle$ to go to zero quickly. The above critical G value is therefore the multi-critical point, i.e. the meeting point of the second order and the first order transition lines. For the $S = 1$ Blume-Capel model, this meeting point is G_{tri}=2.0 in our DS simulations, and at this point an obvious discontinuity or 'jump' of $\langle D(t) \rangle$ and $\langle P_{S_i=0} \rangle$ can be observed in Fig.3.11(a) and Fig.3.11(c). At last, when $G \to +\infty$, the sites are all occupied by S_i=0 spin state.

According to our DS results, we may schematically plot the finite-temperature phase diagram for this model as in Fig.3.11(d). We use T_σ obtained from $\sigma_{D(t)} - T$ relationship in Fig.3.11(b) as the (second order) phase transition temperature. In

Fig.3.11(d), the general shape of the phase diagram shows very good agreement between our calculations and other familiar results. From our results, we estimate the tricritical point (white square in Fig.3.11(d)) for the $S = 1$ Blume-Capel model to be (k_BT_{tri}/J,G_{tri}/J)= (0.56±0.03, 2.00). The estimated static values for the tricritical point for this model are (0.609, 1.965)[14], (0.608, 1.967)[10], (0.610±0.005, 1.966±0.001)[11], (1.088,1.8848)[17], and (1.333, 1.848)[15], etc.

Fig.3.12 shows the results for the integer $S = 2$ Blume-Capel model with the initial condition $C^A(0) = -C^B(0) = \{1\}$. Very similar features to $S = 1$ case are obtained by our DS simulations. From the maximum values of $\sigma_{D(t)}$ in Fig.3.12(b) we may get the (continuous) dynamical transition temperatures to be k_BT_σ/J=7.60±0.25, 7.45±0.20, 7.10±0.15, 6.40±0.20, 5.50±0.25, 4.20±0.20 and 1.00±0.15 for G/J=-4.0, -3.0, -2.0, -1.0, 0.0, 1.0 and 2.0, respectively. Then we get the phase diagram for the S=2 Blume-Capel model in Fig.3.12(d) with the tricritical point (white square in Fig.3.12(d)) for $S = 2$ Blume-Capel model to be (k_BT_{tri}/J , G_{tri}/J)=(1.00±0.15, 2.00). The general shape of this phase diagram is also in agreement with other results such as mean field theory[15] and effective-field theory[17] that predict (1.645, 1.994)[17], and (1.333, 1.848)[15], etc.

Results for the Blume-Capel model with S=3/2 and 5/2

For the half-integer spin Blume-Capel model, we choose to put the factor of 1/4 (product of two 1/2 of the S_i spin values) into the J and G parameters in Eq.(3.19). For example, for the $S = 3/2$ model, the parameters in Eq.(3.19) become $J/4$ and $G/4$, and the spin S_i can take one of the values among (-3, -1, 1, 3). One advantage of this procedure is that it is easy for us to calculate $D(t)$ in Eq.(3.6), since the spin S_i still takes integer values now. We first apply our MCDS procedure to the controversial case of S=3/2 Blume-Capel model concerning the existence or not of a multi-critical point along the transition line.

The results are plotted in Fig.3.13 with the initial condition $C^A(0) = -C^B(0) = \{3\}$. For this model we have observed a different behavior from previous integer models. Fig.3.13(a) shows the results of $\langle D(t) \rangle$ as a function of k_BT/J and G/J. There exist only Ising-like continuous phase transitions for the model. When $G \to +\infty$, the model goes to the standard Ising model with the critical temperature $4k_BT_c/J$=2.269 (the dotted line in the figure), which is consistent with the temperature $4t_c$=$4k_BT_c/J$=$4*1/[2\ln(\sqrt{2}+1)] = 2/\ln(\sqrt{2}+1)$=2.269 as shown in Ref.[14]. In Fig.3.13(b), we plot the temperature dependence of the fluctuation$\sigma_{D(t)}$ for our chosen G values (the dotted line has the same meaning as in Fig.3.13(a)), and we estimate the continuous transition temperature to be $4k_BT_c/J$=19.00±0.40, 18.20±0.36, 17.12±0.34, 15.40±0.50, 13.60±0.30, 10.70±0.30, 3.30±0.45, 3.10±0.20, 2.40±0.10, and 2.40±0.10 for G/J=-4.0, -3.0, -2.0, -1.0, 0.0, 1.0, 2.0, 2.01, 3 and 4, respectively. Our results indicate the absence of a multi-critical point along the phase transition line.

In order to detect the existence or not of an isolated first-order phase transition line as shown in Refs.[15, 14, 19] for this model, we plot $\langle P_{|S_i|=3/2} \rangle$ and $\langle P_{|S_i|=1/2} \rangle$ at G/J=2.0 and 2.01 in Fig.3.13(c). In the literature[14, 19], the range of this isolated first-order transition line is presented between ($4k_BT/J$, G/J)= (3.2, 1.96) and (1.6, 2.0), we plot two dashed lines in Fig.3.13(c) to cover this temperature range. In Fig.3.13(c), we can observe an obvious exchange of the spin values, indicating the first-order transition of two different ordered ferromagnetic phases, one is magnetization $m_1 \to 3/2$ and the other is $m_2 \to 1/2$. Fig.3.13(d) is the plot of the phase diagram for this model. We still use T_σ obtained from $\sigma_{D(t)} - T$ relationship in Fig.3.13(b) as the (second order) phase transition temperature. In Fig.3.13(d), the general shape of the phase diagram shows very good agreement between our calculations and other known results[15, 14, 19]. In this model, because of the absence of

zero value for the spins, the long range order will not vanish, therefore we can only observe the second-order transition along the transition line when G is changed.

Fig.3.14 shows the results for the half-integer $S = 5/2$ Blume-Capel model with the initial condition $C^A(0) = -C^B(0) = \{3\}$. Very similar features to the $S = 3/2$ case are obtained by our DS simulations. Because the transition temperatures is very high for negative G for this model, we only present the results for several positive G values. ¿From the maximum values of $\sigma_{D(t)}$ in Fig.3.14(b) we estimate continuous dynamical transition temperatures to be $4k_BT_c/J$=4.50±0.20, 4.00±0.22, 3.60±0.23, 2.40±0.15, 2.40±0.15 and 2.40±0.10 for G/J=2.01, 2.05, 2.10, 2.5, 3 and 4, respectively. In Fig.3.14(c), we plot $\langle P_{|S_i|=5/2}\rangle$, $\langle P_{|S_i|=3/2}\rangle$ and $\langle P_{|S_i|=1/2}\rangle$ as a function of temperature at G/J=1.98 and 2.01. We can also observe an obvious exchange of the spin values, indicating the first-order transition of three different ordered ferromagnetic phases: magnetization $m_1 \rightarrow 5/2$, $m_2 \rightarrow 3/2$ and $m_3 \rightarrow 1/2$. Therefore we have confirmed the mean field theory results about the existence of two isolated first-order transition lines for this model[15]. At last, we plot the phase diagram for S=5/2 Blume-Capel model in Fig.3.14(d), where the model also goes to the standard Ising model with $4k_BT_c/J$=2.269 when $G \rightarrow +\infty$.

In this work, we investigate, by means of the MCDS technique, the dynamical behavior of integer S=1, 2 and half-integer S=3/2, 5/2 Blume-Capel models on a square lattice within Metropolis-type dynamics. We find that the behavior of the systems are qualitatively different for the integer- and the half-integer- spin versions of this model. For the S=1 and S=2 Blume-Capel models, there exists a multi-critical point along the transition line which strongly depends on the values of the G parameter; For the S=3/2 and S=5/2 cases, our results indicate the absence of a multi-critical point along the transition line when G is changed. In the context of the controversies surrounding the S=3/2 Blume-Capel model, our MCDS results allow us for the first time to distinguish definitely between two proposed contradictory

scenarios. In addition, the MCDS simulations present evidence of isolated first-order transition line(s) for the half-integer Blume-Capel model. A physical explanation to this quite distinct critical behavior is given.

More detailed description of the calculations for above models can be found in [41]- [43].

3.5 References

[1] A.U. Neumann, B. Derrida, J. Phys. France **49** 1647(1988).

[2] P.F. Fox, A.J. Guttmann, J. Phys. C**6** 913(1973).

[3] I.G. Enting, A.J. Guttmann, I. Jensen, J. Phys. A **27** 6987(1994).

[4] M.Blume, Phys.Rev. **141**, 517(1966).

[5] H.W.Capel, Physica **32**, 966(1966).

[6] M.Blume, V.J.Emery, R.B. Griffiths, Phys. Rev. A **4**, 1071(1971).

[7] W.Man Ng, J.H.Barry, Phys. Rev. B **17**, 3675(1978).

[8] M.Tanaka, K.Takahashi, Phys. Status Solidi B **93**, K85(1979).

[9] A.K.Jain, D.P. Landau, Phys. Rev. B **22**, 445(1980).

[10] N.B. Wilding, P. Nielaba, Phys. Rev. E **53**, 926(1996).

[11] P.D. Beale, Phys. Rev. B **33**, 1717(1986).

[12] A.N. Berker, M.Wortis, Phys. Rev. B **14**, 4946(1976); O.F. de Alcántara Bonfim, Physica A **130**, 367(1985).

[13] S.M. de Oliveira, P.M.C. de Oliveira, F.C. de Sá Barreto, J. Stat. Phys. **78**, 1619(1995).

[14] J.C. Xavier, F.C. Alcaraz, D. Penã, J.A. Plascak, Phys. Rev. B **57**, 11575(1998).

[15] J.A. Plascak, J.G. Moreira, F.C. Sá Barreto, Phys. Lett. A **173**, 360(1993).

[16] G.Le Gal, T. Kaneyoshi, A. Khater, Physica A **195**, 174(1993).

[17] T. Kaneyoshi, J.W. Tucker, M. Jaščur, Physica A **186**, 495(1992).

[18] D. Peña Lara, J.A. Plascak, Int. J. Mod. Phys. B **12** 2045(1998).

[19] J.A. Plascak, D.P. Landau, **85**, 100(1999), Computer Simulations in Condensed Matter Physics XII, Eds. D.P. Landau, S.P. Lewis and H.B. Schüttler (Berlin:Springer).

[20] A. Bakchich, A. Bassir, A. Benyoussef, Physica A **195**, 188(1993).

[21] F.C. Sá Barreto, O.F. Alcantara Bonfim, Physica A **172**, 378(1991).

[22] G.J.A. Hunter, R.C.L. Jenkins, C.J. Tinsley, J. Phys. A **23**4547(1990); R.G. Bowers, B.Y. Yousif, Phys. Lett. A **96** 49(1983).

[23] Kun-Fa Tang, Jia-Zhen Hu, Acta Physica Sinica, **35** 1048(1986).

[24] S.G.A. Quadros, S.R. Salinas, Physica A **206** 479(1994).

[25] S.L. Schofield, R.G. Bowers, J. Phys. A **13** 3697(1980).

[26] T. Kaneyoshi, J.C. Chen, J. Magn. Magn. Mater. **98** 201(1991).

[27] A.F. Siqueira, I.P. Fittipaldi, J. Magn. Magn. Mater. **54** 678(1986).

[28] T. Kaneyoshi, Solid State Commun. **70** 975(1989).

[29] T. Kaneyoshi, J. Phys. Soc. Jpn **56** 2675(1989).

[30] G.M. Buendia, M.A. Novotny, J.Phys.: Condens. Matter. **9** 5951(1997).

[31] G.M. Buendia, M.A. Novotny, J. Zhang , 223(1994), Computer Simulations in Condensed Matter Physics VII eds. D.P. Landau, K.K. Mon and H.B. Schüttler (Berlin:Springer).

[32] T.Kaneyoshi, J. Phys. Soc. Jpn **56** 2675(1989).

[33] Kun-Fa Tang, J. Phys. A **21** L1097(1988).

[34] G.M. Buendia, E. Machado, Phys. Rev. E **58** 1260(1998).

[35] B.Y. Yousif, R.G. Bowers, J. Phys. A **17** 3389(1984).

[36] Kun-Fa Tang, Jia-Zhen Hu, J. Phys. A **20** 3069(1987).

[37] Yung-Li Wang, Felix Lee, J.D. Kimel Phys. Rev. B **36** 8945(1987).

[38] Magnetic Molecular Materials, Vol. 198 of NATO ASI Series E, edited by D. Gatteschi, O. Kahn, J. S. Miller, and F. Palacio (Kluwer Academic, Dordrecht, 1991).

[39] K. Binder, J. Stat. Phys. **24** 69(1981).

[40] R. Ehrlich, Physics and Computers: Problems, Simulations, and Data Analysis. Houghton Mifflin Company . 1973 .

[41] Ce-Jun Liu, H.B. Schüttler, Jia-Zhen Hu, Commun. Theor. Phys. **35** 480(2001).

[42] Ce-Jun Liu, H.B. Schüttler, Jia-Zhen Hu, Phys. Rev. E , **65** 016114(2002).

[43] Ce-Jun Liu, H.B. Schüttler, Phys. Rev. E , **65** 056103(2002).

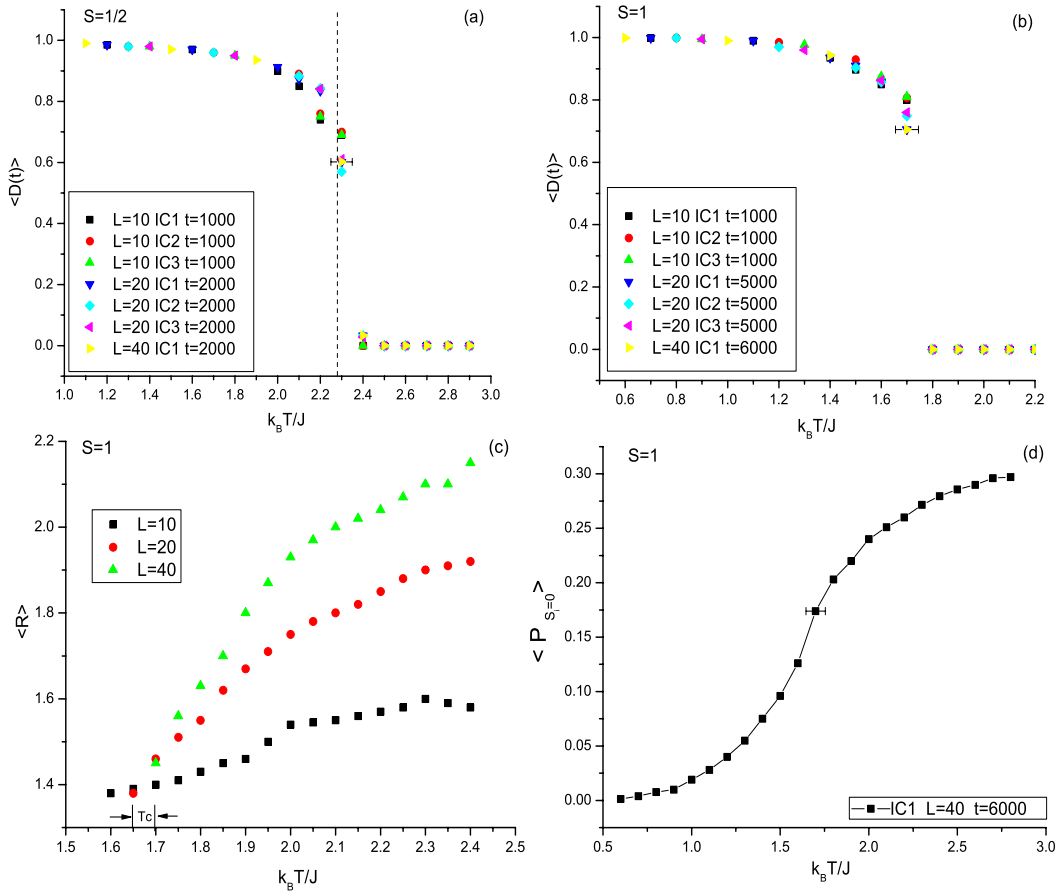

Figure 3.1: The damage spreading results for $S = 1/2$ and $S = 1$ Ising spin models. Fig.3.1(a), the $\langle D(t)\rangle$ as a function of k_BT/J for the $S = 1/2$ model. The vertical dotted line marks the exactly known value of $k_BT_c/J = 2.269$ for the standard Ising model. Two temperature regimes are observed. In Fig.3.1(b), two temperature regimes are also observed for S=1 model. In both Fig.3.1(a) and Fig.3.1(b), at the maximum $\sigma_{D(t)}$ point (the magnitude of $\sigma_{D(t)}$ of other points are smaller than this point) with L=40, IC1 and t=6000, we estimate the transition temperature k_BT_σ/J to be 2.30±0.05 and 1.70±0.045, respectively, for these two models. Fig. 3.1(c), the ratio $\langle R\rangle$ versus k_BT/J for different sizes L for the $S = 1$ model. All curves cross in the k_BT_c/J region; Fig.3.1(d), the ratio $\langle P_{S_i=0}\rangle$ as a function of k_BT/J for the S=1 model after a long time limit. At the maximum standard deviation point (the magnitude of standard deviations of other points are smaller than this point), we estimate the transition temperature to be 1.70±0.05. In all figures, the standard errors (error bars) are less than the size of symbols.

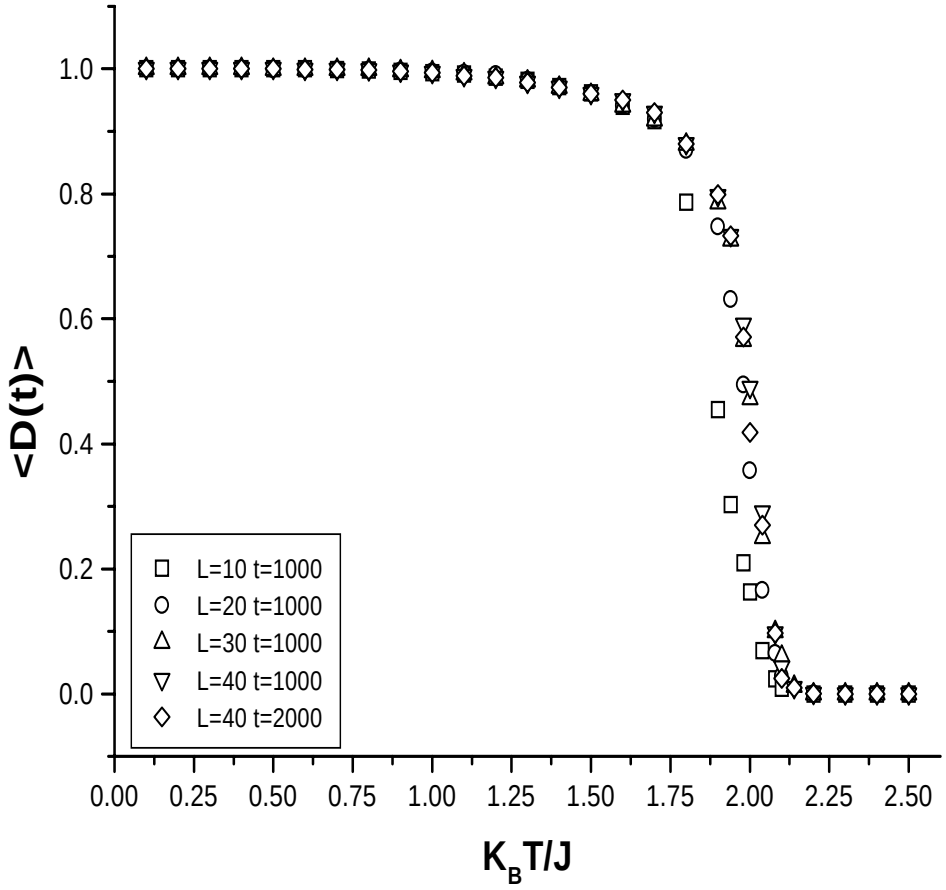

Figure 3.2: The average damage $\langle D(t)\rangle$ as a function of temperature for the mixed Ising ferrimagnetic model with G=0 on the square lattice. The symbols for different times and the same lattice superimpose, indicating the establishment of equilibrium. The standard errors (error bars) are less than the size of symbols.

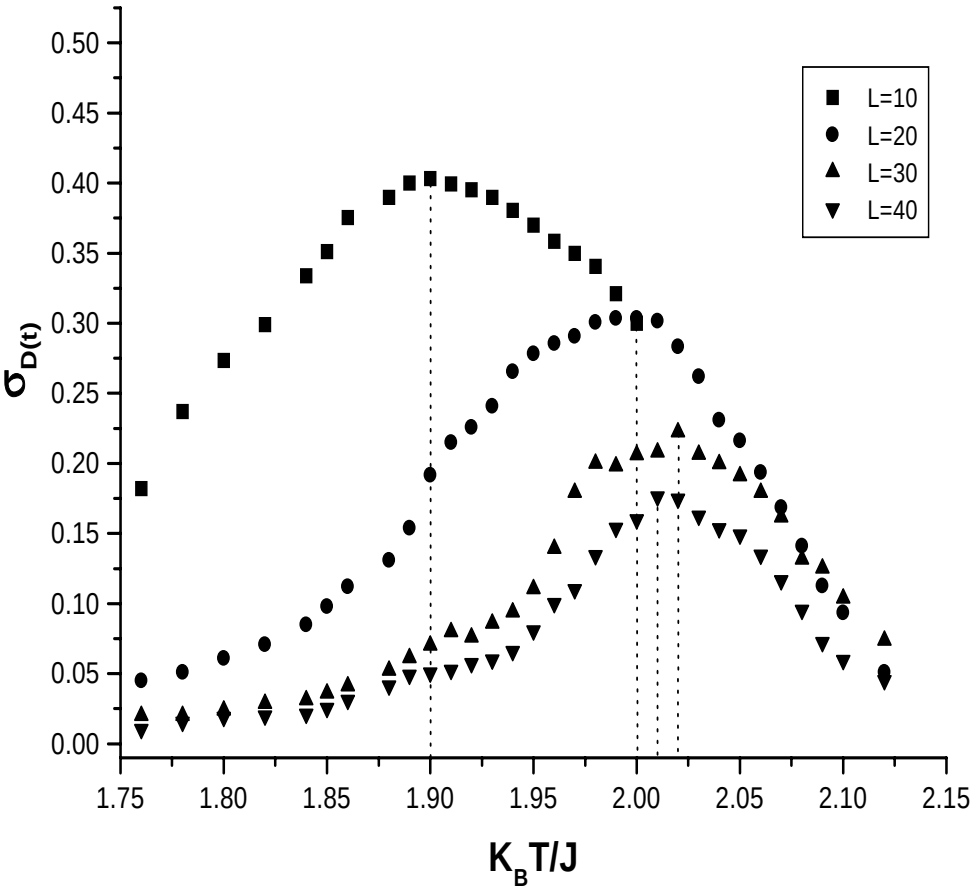

Figure 3.3: The damage susceptibility $\sigma_{D(t)}$ as a function of temperature for mixed Ising ferrimagnetic model with G=0 on the square lattice at t=1000. The dotted lines indicate the positions of $k_B T_\sigma(L)/J$. The standard errors (error bars) are less than the size of symbols.We estimate the damage spreading temperature $k_B T_\sigma/J$ from $\sigma_{D(t)}$ to be 2.02.

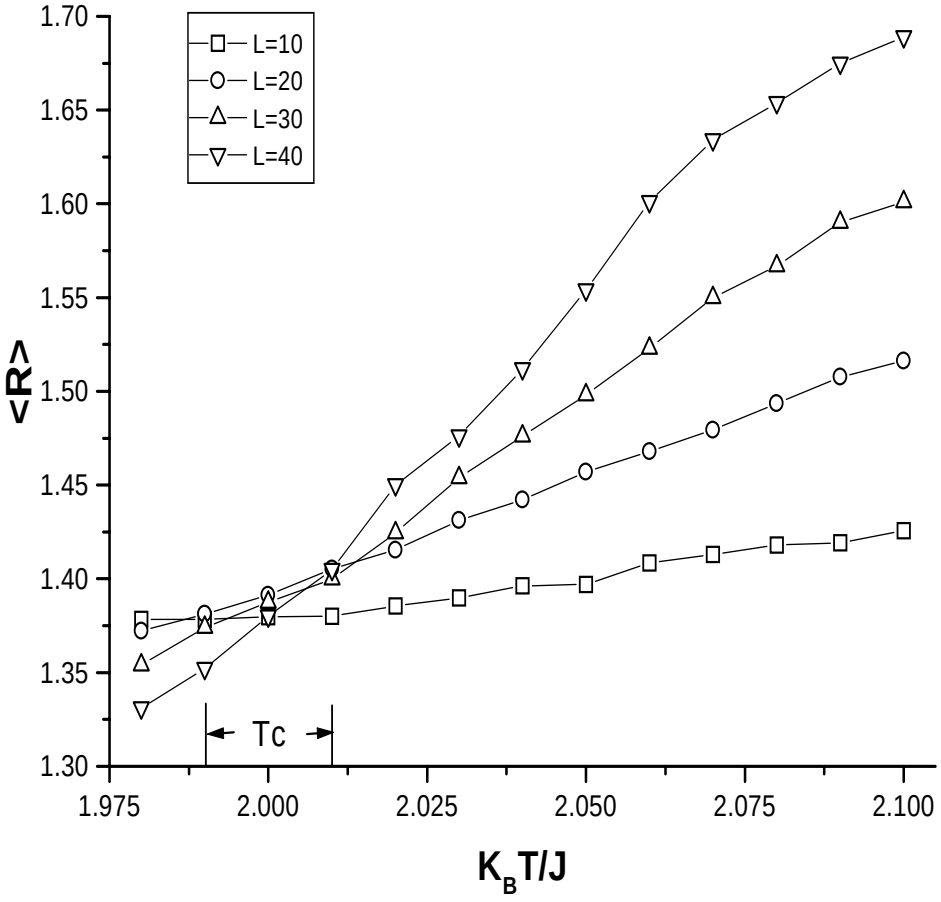

Figure 3.4: The ratio $\langle R \rangle$ versus temperature for different sizes L for the mixed Ising ferrimagnetic model with G=0 on the square lattice. The full line is a guide for the eye. The standard errors (error bars) are less than the size of symbols. All curves cross in the region of $k_B T_c/J$=2.00 $\pm$ 0.01.

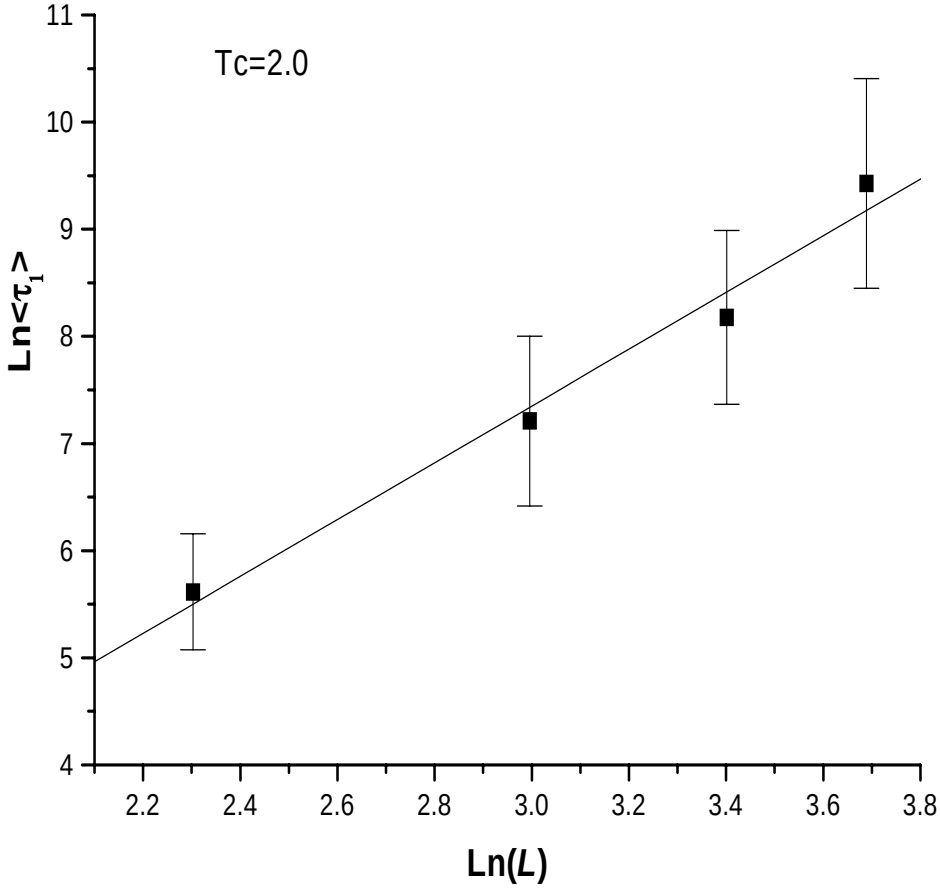

Figure 3.5: Linear fit for dynamical critical exponent z at $k_B T_c/J$=2.0

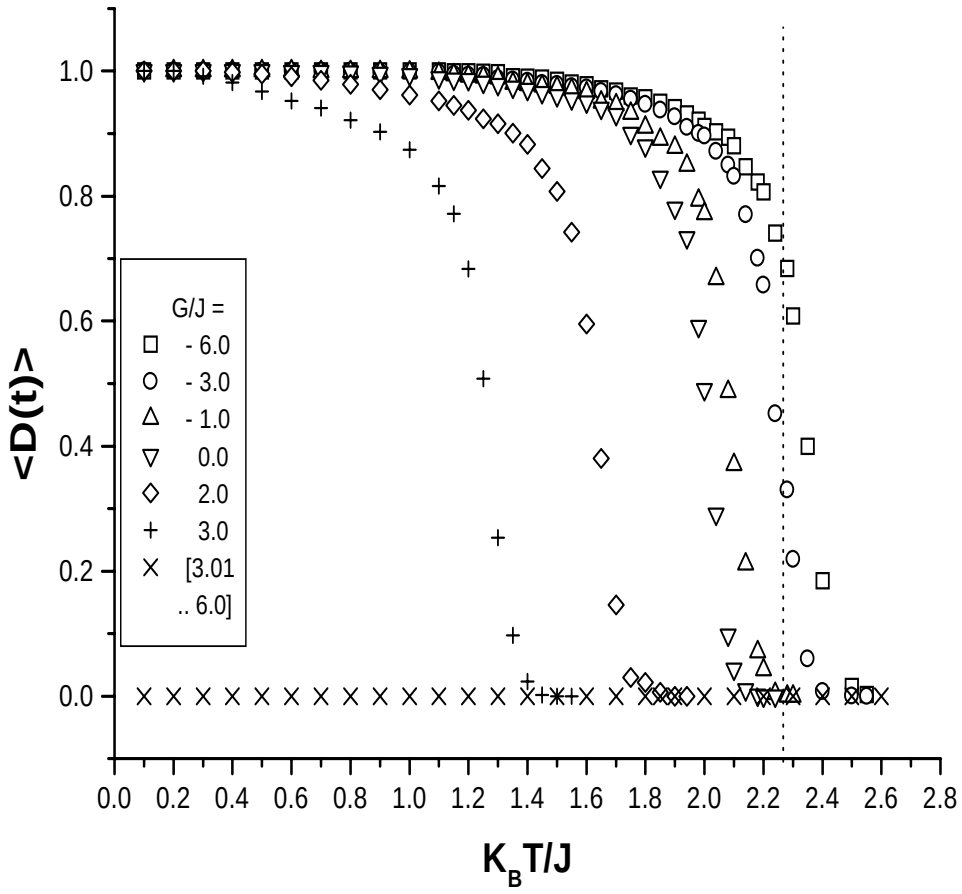

Figure 3.6: The average damage $\langle D(t)\rangle$ as a function of temperature and G for mixed Ising ferrimagnetic model with $G \neq 0$ on the square lattice at L=40, t=1000 and N_s=200. The standard errors (error bars) are less than the size of symbols. A completely different behavior of $\langle D(t)\rangle$ can be observed for $G/J \leq 3.0$ and for $G/J > 3.0$. The vertical dotted line marks the exactly known value of $k_B T_c/J$ for the standard Ising model on the square lattice.

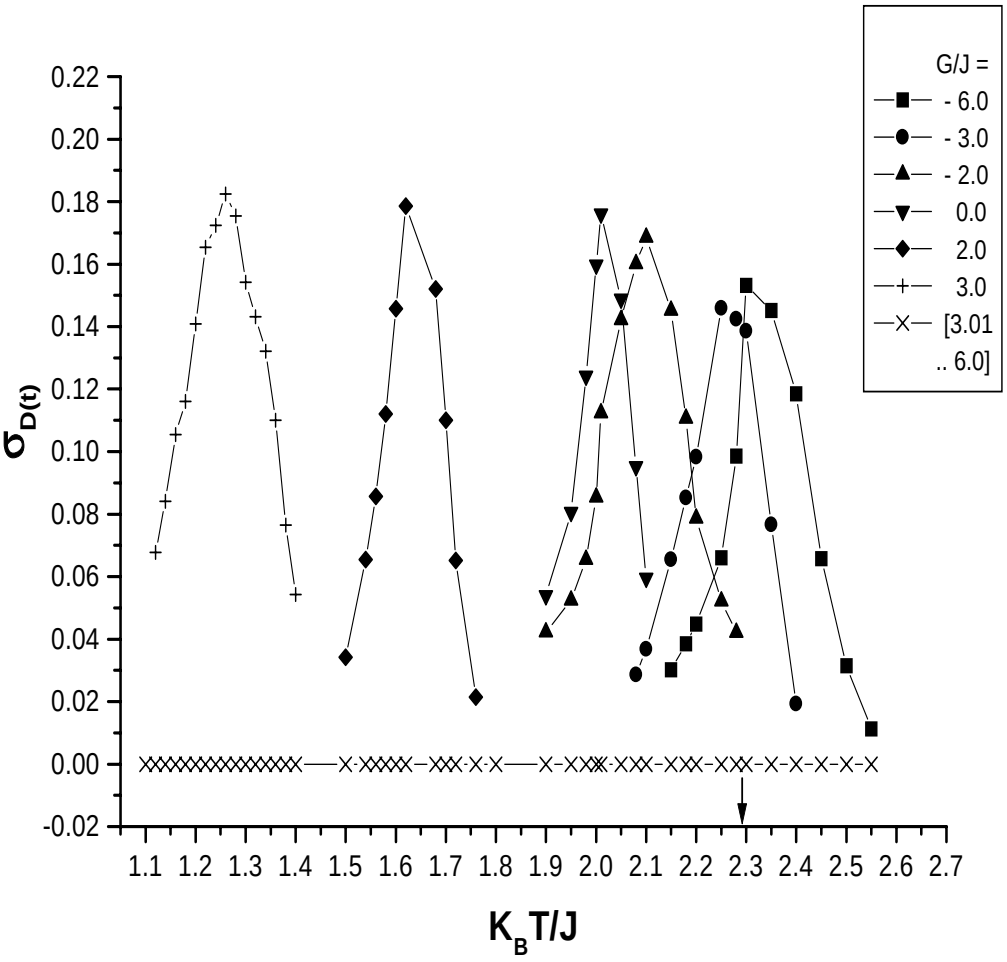

Figure 3.7: The damage susceptibility $\sigma_{D(t)}$ as a function of temperature and G/J for mixed Ising ferrimagnetic model with $G \neq 0$ on the square lattice at L=40, t=1000 and N_s=200. The standard errors (error bars) are less than the size of symbols. A completely different behavior can be observed for $G/J \leq 3.0$ and for $G/J >$3.0. The full line is a guide to the eye. The arrow points to the transition temperature of standard Ising model on the square lattice.

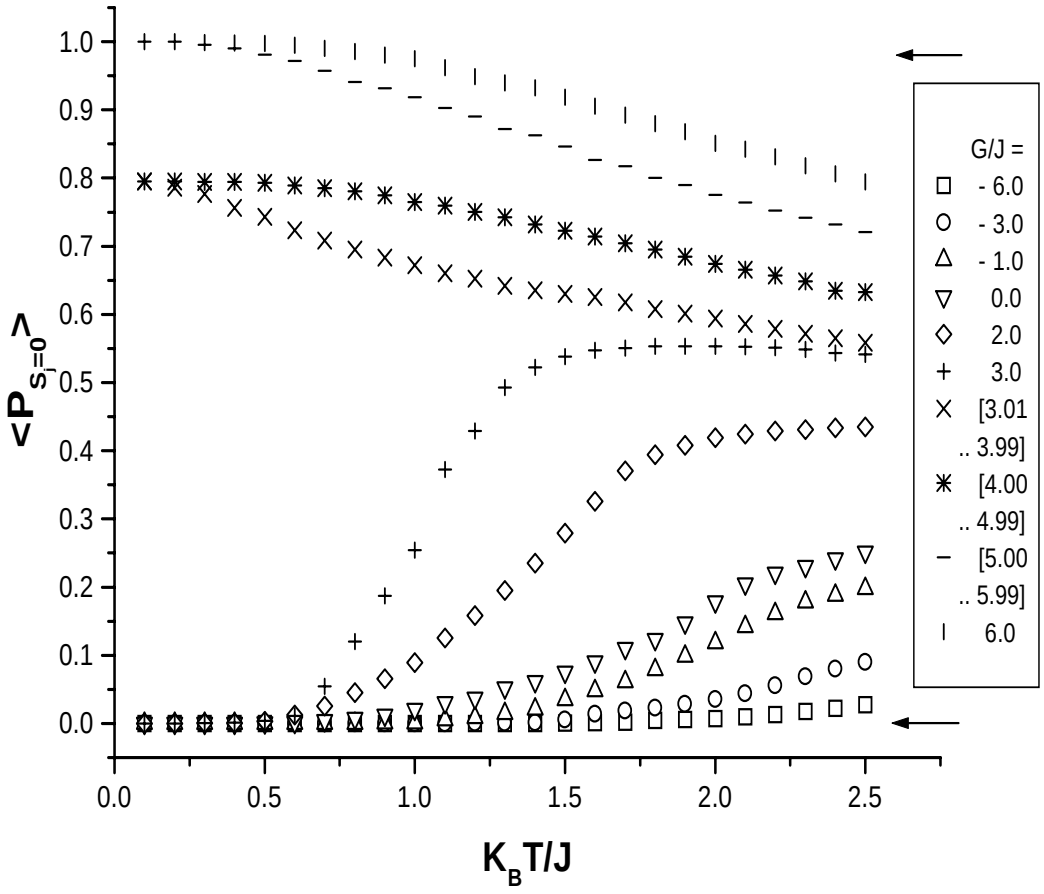

Figure 3.8: The ratio $\langle P_{S_j=0} \rangle$ in S sub-lattice as a function of $k_B T/J$ and G/J for the mixed Ising ferrimagnetic model on the square lattice at L=40,t=1000 and N_s=200. The standard errors (error bars) are less than the size of symbols. Two completely different regions can be observed for $G/J \leq 3.0$ and for $G/J >$3.0. The upper arrow points to the $\langle P_{S_j=0} \rangle$=1.0 which corresponds to the staggered quadrupolar phase. The lower arrow points to the $\langle P_{S_j=0} \rangle$=0.0 which corresponds to the standard Ising model.

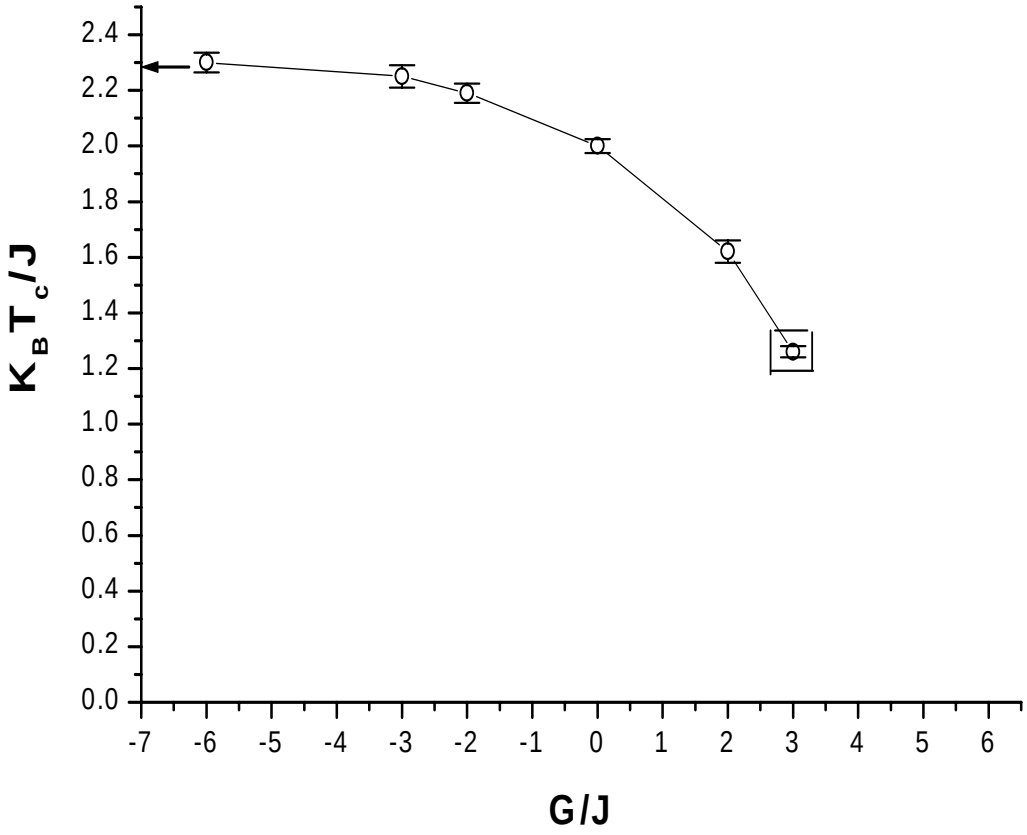

Figure 3.9: The finite-temperature phase diagram for the mixed spin Ising model on the square lattice using damage spreading procedure. The solid line corresponds to the second order transition. The white square denotes the tricritical point at which the phase transition changes from second-order to first-order. The upper-left arrow points to the transition temperature of the standard Ising model.

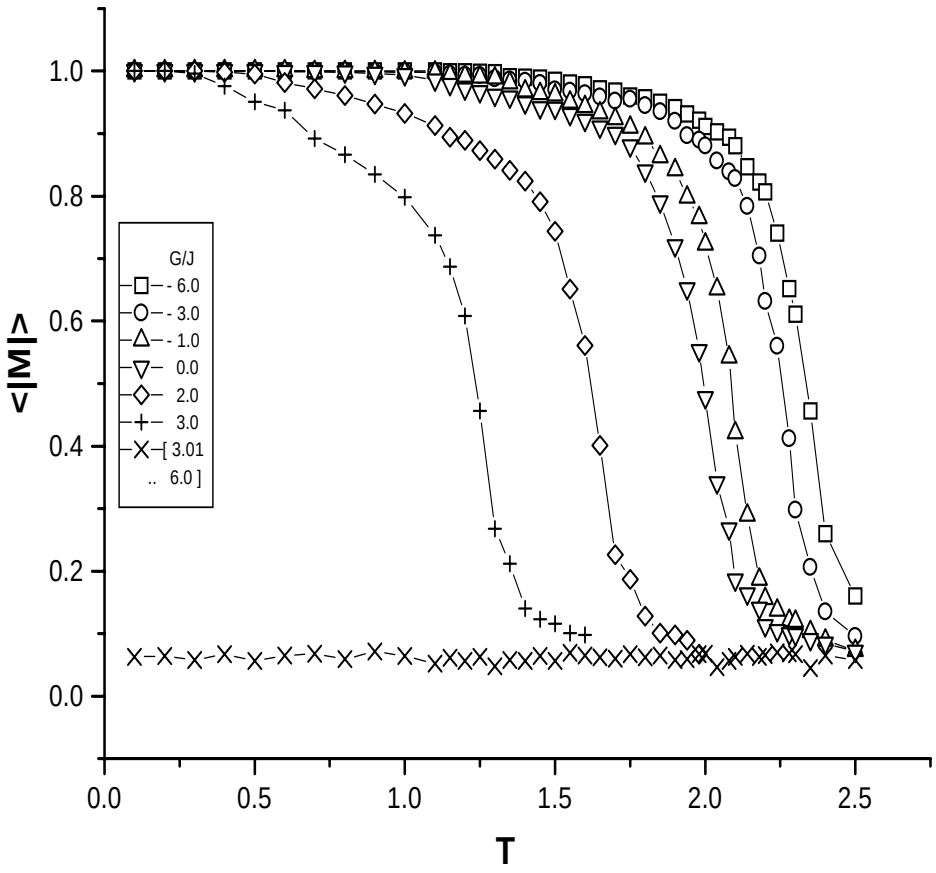

Figure 3.10: The total magnetization of the system $\langle |M(t)| \rangle$ as a function of temperature and G/J for the mixed spin Ising model on the square lattice at L=40, t=1000 and N_s=200. The standard errors (error bars) are less than the size of symbols. Similar to $\langle D(t) \rangle$, two completely different regions can be observed for $G/J \leq$ 3.0 and for $G/J >$3.0. For each $G/J >$ 3.0 value, $\langle |M(t)| \rangle$ independently goes to zero, except for the remnant finite-size and finite-time effects.

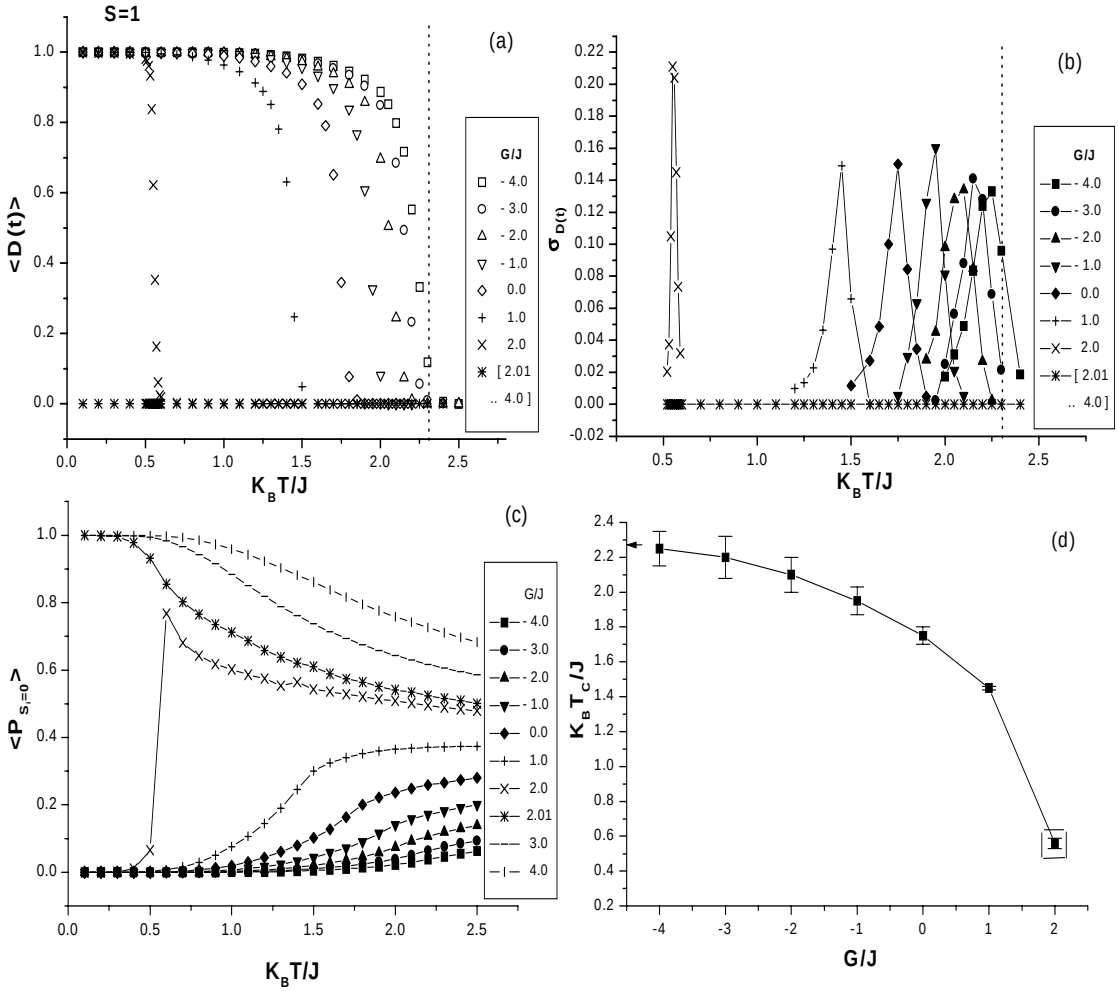

Figure 3.11: The damage spreading results for $S = 1$ Blume-Capel model on the square lattice at L=40, t=1000 and N_s=200. In the figure, a completely different behavior can be observed for $G/J \leq 2.0$ and for $G/J > 2.0$. The vertical dotted line marks the exactly known value of k_BT_c/J for the standard Ising model on the square lattice. Fig.3.11(a), the average damage $\langle D(t)\rangle$ as a function of temperature and G/J. Fig.3.11(b), the damage susceptibility $\sigma_{D(t)}$ as a function of temperature and G/J. The full line is a guide to the eye. From the maximum values of $\sigma_{D(t)}$, we may locate the phase transition temperature. Fig.3.11(c), the ratio $\langle P_{S_i=0}\rangle$ as a function of temperature and G/J. The $\langle P_{S_i=0}\rangle$=0.0 corresponds to the standard Ising model. Fig.3.11(d), the finite-temperature phase diagram for $S = 1$ Blume-Capel model on the square lattice by damage spreading procedure. The solid line represents the second order transition. The white square denotes the tricritical point at which the phase transition changes from second-order to first-order. In Figures (a), (b) and (c), the standard errors (error bars) are less than the size of symbols.

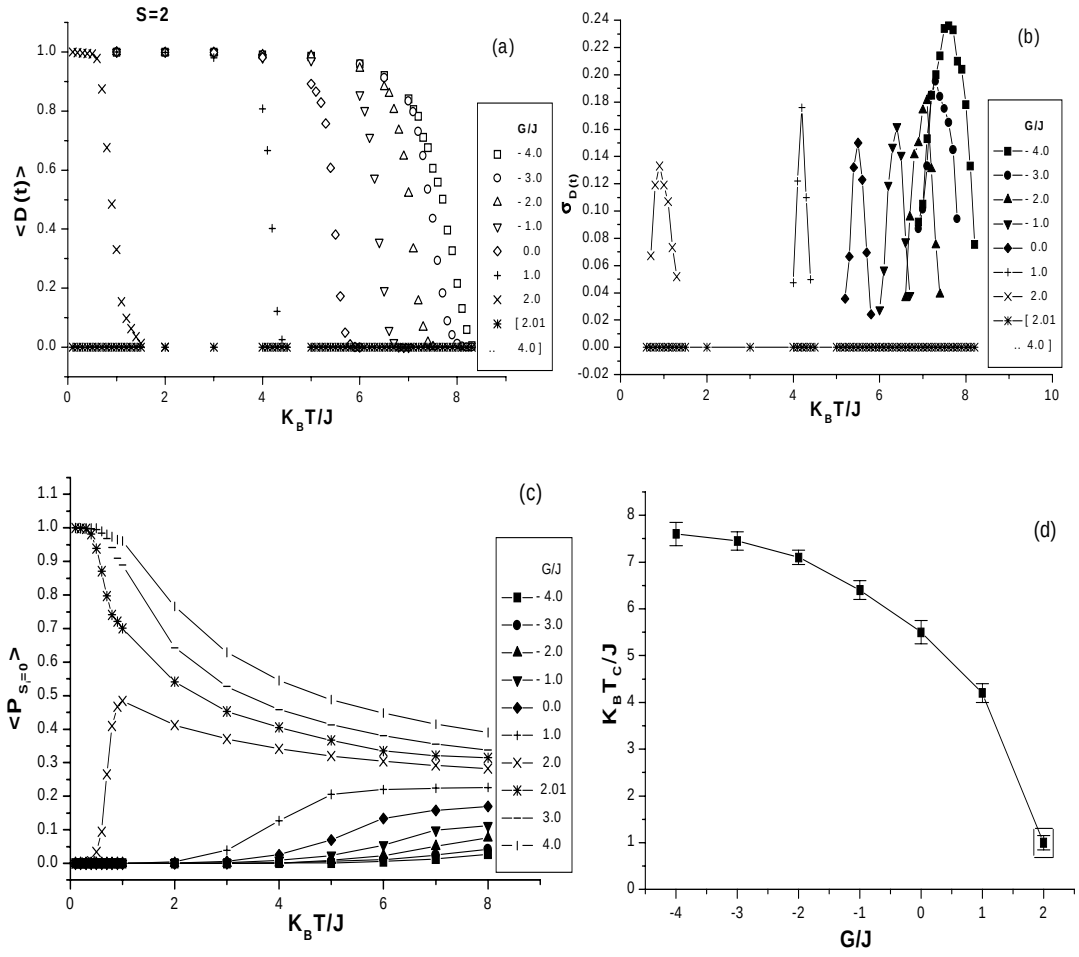

Figure 3.12: The damage spreading results for $S = 2$ Blume-Capel model on the square lattice at L=40, t=1000 and N_s=200. The notes are the same as in Fig.3.11. In Figures (a), (b) and (c), the standard errors (error bars) are less than the size of symbols.

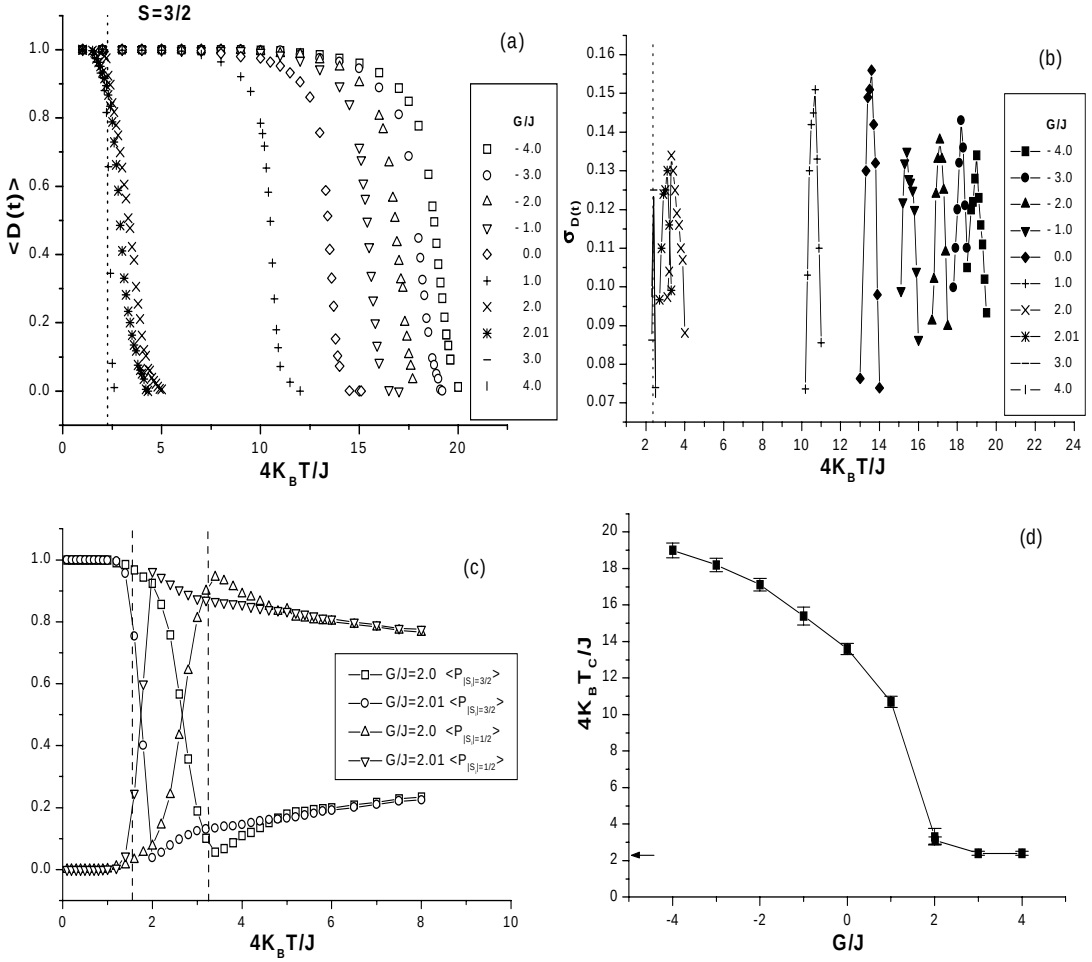

Figure 3.13: The damage spreading results for $S = 3/2$ Blume-Capel model on the square lattice at L=40, t=1000 and N_s=200. Fig.3.13(a), the average damage $\langle D(t)\rangle$ as a function of temperature and G/J. Fig.3.13(b), the damage susceptibility $\sigma_{D(t)}$ as a function of temperature and G/J. The full line is a guide to the eye. Fig.3.13(c), $\langle P_{|S_i|=3/2}\rangle$ and $\langle P_{|S_i|=1/2}\rangle$ as a function of temperature at G/J=2.0 and 2.01. Fig.3.13(d), the phase diagram for $S = 3/2$ Blume-Capel model on the square lattice by damage spreading procedure. The solid line represents the second order transition. The lower arrow points to the transition temperature ($4k_BT_c/J$=2.269) of the standard Ising model on the square lattice. In Figures (a), (b) and (c), the standard errors (error bars) are less than the size of symbols. See text for details.

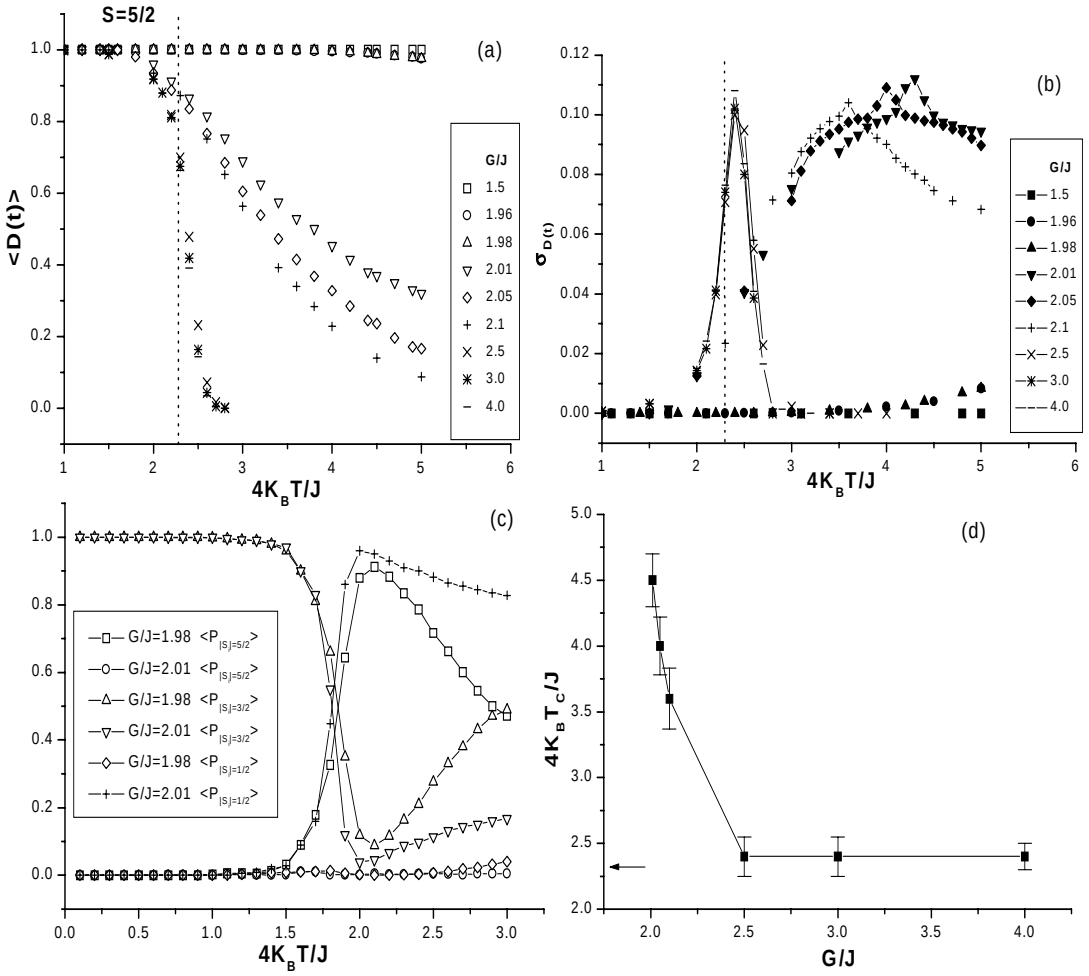

Figure 3.14: The damage spreading results for $S = 5/2$ Blume-Capel model on the square lattice at L=40, t=1000 and N_s=200. The notes are the same as in Fig.3.13. In Figures (a), (b) and (c), the standard errors (error bars) are less than the size of symbols.

Chapter 4

Self-Consistent Feynman Diagram Expansion (SCFDE) Technique

4.1 Field Theory at Finite Temperature

Experiments are done at finite temperatures. Since one goal of many-body theory is to explain experiments, here we will briefly show how to incorporate finite temperature into the Green's function. The finite temperature formalism was originated by *Matsubara*. It will actually be easier to use than the zero temperature version, and the zero temperature result is always easily obtained from the finite temperature result by just setting T=0.[1]

4.1.1 Temperature Green's Function

In treating systems at finite temperature, it will be most convenient to use the *Grand Canonical Ensemble* , which allows a variable number of particles. With the definition of Grand Canonical Hamiltonian

$$\hat{K} = \hat{H} - \mu\hat{N} \tag{4.1}$$

The Grand Partition Function is

$$Z_G = e^{-\beta\Omega} = Tre^{-\beta\hat{K}} \tag{4.2}$$

Ω is called the thermodynamic potential, β=$1/T$ denotes the inverse temperature. The Density Operator is

[1]Note: The References of Chapter 4 are combined in Chapter 5

$$\hat{\rho}_G = Z_G^{-1} e^{-\beta \hat{K}} = e^{\beta(\Omega - \hat{K})} \tag{4.3}$$

where μ is the chemical potential, $Tr()$ denotes the $Trace$ of a matrix. For any Schrödinger operator $\hat{O}_s(\mathbf{x})$, the Heisenberg picture is

$$\hat{O}_{\mathbf{k}}(\mathbf{x}\tau) \equiv e^{\hat{K}\tau/\hbar} \hat{O}_s(\mathbf{x}) e^{-\hat{K}\tau/\hbar} \tag{4.4}$$

The $Field$ operator assumes the form

$$\hat{\Psi}_{\mathbf{k}\alpha}(\mathbf{x}\tau) = e^{\hat{K}\tau/\hbar} \hat{\Psi}_{\alpha}(\mathbf{x}) e^{-\hat{K}\tau/\hbar} \tag{4.5}$$

$$\hat{\Psi}^{\dagger}_{\mathbf{k}\alpha}(\mathbf{x}\tau) = e^{\hat{K}\tau/\hbar} \hat{\Psi}^{\dagger}_{\alpha}(\mathbf{x}) e^{-\hat{K}\tau/\hbar} \tag{4.6}$$

Note that $\hat{\Psi}^{\dagger}_{\mathbf{k}\alpha}(\mathbf{x}\tau)$ is *not* the adjoint of $\hat{\Psi}_{\mathbf{k}\alpha}(\mathbf{x}\tau)$ as long as τ is real. If τ is interpreted as a complex variable, it may be analytically continued to a pure imaginary value τ=it. The resulting $\hat{\Psi}^{\dagger}_{\mathbf{k}\alpha}(\mathbf{x}, it)$ then becomes the true adjoint of $\hat{\Psi}_{\mathbf{k}\alpha}(\mathbf{x}, it)$. The operators in Eqs.(4.5),(4.6) are sometimes called the *imaginary-time* operators.

The single-particle imaginary-time Green's function is then defined as

$$G_{\alpha\beta}(\mathbf{x}\tau, \mathbf{x}'\tau') \equiv -Tr\{\hat{\rho}_G T_\tau[\hat{\Psi}_{\mathbf{k}\alpha}(\mathbf{x}\tau)\hat{\Psi}^{\dagger}_{\mathbf{k}\beta}(\mathbf{x}'\tau')]\} \tag{4.7}$$

where $0 < \tau, \tau' < \beta\hbar$ and $\hat{\rho}_G$ is given by Eq.(4.3). Here the symbol T_τ *orders* the operators according to their values of τ, with the smallest at the right; T_τ also includes the signature factor $(-1)^P$, where P is the number of permutations of *fermion* operators needed to restore the original ordering. The trace (Tr) implies that this Green's function G involves a sum over a complete set of states in the *Hilbert* space, each contribution being weighted with the operator $\hat{\rho}_G$.

The imaginary-time Green's function is useful because it enable us to calculate the thermodynamic behavior of the system. If the Hamiltonian $\hat{H}$ is *time independent*

, as is usually the case, then G depends only on the combination τ-τ', and not on τ and τ' separately.

For example, one of the observables, the *mean number* of particles in the system is given by

$$N(T,V,\mu) = \mp \int TrG_{\alpha\beta}(\mathbf{x}\tau, \mathbf{x}\tau^{+})\, d^3x \tag{4.8}$$

where

$$\begin{aligned} TrG_{\alpha\beta}(\mathbf{x}\tau, \mathbf{x}\tau^{+}) &= \mp \sum_{\alpha} Tr[\hat{\rho}_G \hat{\Psi}^{\dagger}_{\mathbf{k}\alpha}(\mathbf{x}\tau)\hat{\Psi}_{\mathbf{k}\alpha}(\mathbf{x}\tau)] \\ &= \mp e^{\beta\Omega} \sum_{\alpha} Tr[e^{-\beta\hat{K}} e^{\hat{K}\tau/\hbar} \hat{\Psi}^{\dagger}_{\alpha}(\mathbf{x})\hat{\Psi}_{\alpha}(\mathbf{x}) e^{-\hat{K}\tau/\hbar}] \\ &= \mp e^{\beta\Omega} \sum_{\alpha} Tr[e^{-\beta\hat{K}} \hat{\Psi}^{\dagger}_{\alpha}(\mathbf{x})\hat{\Psi}_{\alpha}(\mathbf{x})] \\ &= \mp < \hat{n}(\mathbf{x}) > \end{aligned} \tag{4.9}$$

Here the cyclic property Tr(ABC)=Tr(BCA)=Tr(CAB) is used, along with the commutativity of any two functions of the same operator. The *upper (lower)* signs refer to *bosons (fermions).*

4.1.2 Interaction Picture and Perturbation Theory

We introduce the *interaction* picture, which is a basis for perturbation calculations. For any operator $\hat{O}_S$ in the Schrödinger picture, the interaction picture operator $\hat{O}_I$, and Heisenberg picture operator $\hat{O}_K$ can be defined

$$\begin{aligned} \hat{O}_I(\tau) &\equiv e^{\hat{K_0}\tau/\hbar} \hat{O}_S e^{-\hat{K_0}\tau/\hbar} \\ \hat{O}_K(\tau) &\equiv e^{\hat{K}\tau/\hbar} \hat{O}_S e^{-\hat{K}\tau/\hbar} \end{aligned} \tag{4.10}$$

where we rewrite $\hat{H} = \hat{H}_0 + \hat{H}_1$ and $\hat{H}_0$ acting alone yields a soluble problem, $\hat{H}_1$ is a perturbation term. In general, $\hat{H}_0$ does not commute with $\hat{H}_1$. Therefore, Eq.(4.1) can be written as $\hat{K} = \hat{K_0} + \hat{K_1}$. The two pictures are related by

$$\begin{aligned}\hat{O}_K(\tau) &= e^{\hat{K}\tau/\hbar}e^{-\hat{K}_0\tau/\hbar}\hat{O}_I(\tau)e^{\hat{K}_0\tau/\hbar}e^{-\hat{K}\tau/\hbar} \\ &= \hat{u}(0,\tau)\hat{O}_I(\tau)\hat{u}(\tau,0) \qquad (4.11)\end{aligned}$$

where $\hat{u}$ is defined by

$$\hat{u}(\tau_1,\tau_2) \equiv e^{\hat{K_0}\tau_1/\hbar}e^{-\hat{K}(\tau_1-\tau_2)/\hbar}e^{-\hat{K_0}\tau_2/\hbar} \qquad (4.12)$$

Eq.(4.12) can be rewritten as

$$e^{-\hat{K}\tau/\hbar} = e^{-\hat{K}_0\tau/\hbar}\hat{u}(\tau,0) \qquad (4.13)$$

Eq.(4.12) satisfies the group property

$$\hat{u}(\tau_1,\tau_2)\hat{u}(\tau_2,\tau_3) = \hat{u}(\tau_1,\tau_3) \qquad (4.14)$$

and the boundary condition

$$\hat{u}(\tau_1,\tau_1) = 1 \qquad (4.15)$$

Now, using the definition of

$$\hat{K}_1(\tau) = e^{\hat{K_0}\tau/\hbar}\hat{K}_1e^{-\hat{K_0}\tau/\hbar} \qquad (4.16)$$

we can get the derivative of $\hat{u}$

$$\hbar\frac{\partial\hat{u}(\tau,\tau')}{\partial\tau} = -\hat{K}_1(\tau)\hat{u}(\tau,\tau') \qquad (4.17)$$

If τ is set equal to $\beta\hbar$, Eqs.(4.13),(4.17) provide a perturbation expansion for the grand partition function

$$
\begin{aligned}
e^{-\beta\Omega} &= Tre^{-\beta\hat{K}} \\
&= Tr[e^{-\beta\hat{K}_0}\hat{u}(\beta\hbar,0)] \\
&= \sum_{n=0}^{\infty}(-1/\hbar)^n(1/n!)\int_0^{\beta\hbar} d\tau_1 \cdot\cdot \int_0^{\beta\hbar} d\tau_n Tr\{e^{-\beta\hat{K}_0}Tr[\hat{K}_1(\tau_1)\cdot\cdot\hat{K}_n(\tau_n)]\}
\end{aligned}
\tag{4.18}
$$

The exact imaginary-time Green's function can now be rewritten as

$$
G_{\alpha\beta}(\mathbf{x}\tau,\mathbf{x}'\tau') = \frac{-Tr\{e^{-\beta\hat{K}_0}\sum_{n=0}^{\infty}(-\hbar)^{-n}(n!)^{-1}\int_0^{\beta\hbar} d\tau_1\cdot\cdot\int_0^{\beta\hbar} d\tau_n Tr[\hat{K}_1(\tau_1)\cdot\cdot\hat{K}_n(\tau_n)\hat{\Psi}_{\mathbf{I}\alpha}(\mathbf{x}\tau)\hat{\Psi}^{\dagger}_{\mathbf{I}\beta}(\mathbf{x}'\tau')]\}}{Tr\{e^{-\beta\hat{K}_0}\sum_{n=0}^{\infty}(-\hbar)^{-n}(n!)^{-1}\int_0^{\beta\hbar} d\tau_1\cdot\cdot\int_0^{\beta\hbar} d\tau_n Tr[\hat{K}_1(\tau_1)\cdot\cdot\hat{K}_n(\tau_n)]\}}
\tag{4.19}
$$

An important property of Green's function is its *periodicity*. From Eq.(4.19), we see that the variable τ_i extends from 0 to $\beta\hbar$, so that -$\beta\hbar < \tau - \tau' < \beta\hbar$ is satisfied. Let τ' be fixed ($0 < \tau' < \beta\hbar$), then

$$
\begin{aligned}
G_{\alpha\beta}(\mathbf{x}0,\mathbf{x}'\tau') &= \mp e^{\beta\Omega}Tr\{e^{-\beta\hat{K}}\hat{\Psi}^{\dagger}_{\mathbf{k}\beta}(\mathbf{x}'\tau')\hat{\Psi}_{\mathbf{k}\alpha}(\mathbf{x}0)\} \\
&= \mp e^{\beta\Omega}Tr\{\hat{\Psi}_{\mathbf{k}\alpha}(\mathbf{x}0)e^{-\beta\hat{K}}\hat{\Psi}^{\dagger}_{\mathbf{k}\beta}(\mathbf{x}'\tau')\} \\
&= \mp e^{\beta\Omega}Tr\{e^{-\beta\hat{K}}\hat{\Psi}_{\mathbf{k}\alpha}(\mathbf{x}\beta\hbar)\hat{\Psi}^{\dagger}_{\mathbf{k}\beta}(\mathbf{x}'\tau')\} \\
&= \pm G_{\alpha\beta}(\mathbf{x}\beta\hbar,\mathbf{x}'\tau')
\end{aligned}
\tag{4.20}
$$

Similarly

$$
G_{\alpha\beta}(\mathbf{x}\tau,\mathbf{x}'0) = \pm G_{\alpha\beta}(\mathbf{x}\tau,\mathbf{x}'\beta\hbar) \tag{4.21}
$$

In the usual situation, $\hat{H}$ is time independent, and G depends only on the combination $\tau - \tau'$, so Eqs.(4.20),(4.21) can be rewritten as

$$G_{\alpha\beta}(\mathbf{x},\mathbf{x}',\tau-\tau'<0)=\pm G_{\alpha\beta}(\mathbf{x},\mathbf{x}',\tau-\tau'+\beta\hbar) \tag{4.22}$$

As before, our convention is that upper(lower) signs refer to bosons(fermions). As first proved by Matsubara, Eq.(4.19) can be expressed by a diagrammatic expansion. This leads to the *Feynman Diagram Expansion Technique*.

4.2 Self-Consistent Feynman Diagram Expansion Technique

4.2.1 Derivation of Matsubara Frequency

For simplicity, we assume that Green's function G depends only on the difference $\tau_1-\tau_2$ as shown in Eqs.(4.20)-(4.22), which represents the most common situation:

$$G(\mathbf{x}_1,\tau_1,\mathbf{x}_2,\tau_2)=G(\mathbf{x}_1,\mathbf{x}_2,\tau_1-\tau_2) \tag{4.23}$$

For *both* statistics, G is *periodic* over the range $2\beta\hbar$ and then can be expanded in a *Fourier* series:

$$G(\mathbf{x}_1,\mathbf{x}_2,\tau)=(\beta\hbar)^{-1}\sum_n e^{-i\omega_n\tau}G(\mathbf{x}_1,\mathbf{x}_2,\omega_n) \tag{4.24}$$

where $\tau\equiv\tau_1-\tau_2$ and

$$\omega_n=\frac{n\pi}{\beta\hbar} \tag{4.25}$$

This representation ensures that $G(\mathbf{x}_1,\mathbf{x}_2,\tau+2\beta\hbar)=G(\mathbf{x}_1,\mathbf{x}_2,\tau)$ and the Fourier coefficient is given by

$$G(\mathbf{x}_1,\mathbf{x}_2,\omega_n)=\frac{1}{2}\int_{-\beta\hbar}^{\beta\hbar}d\tau e^{i\omega_n\tau}G(\mathbf{x}_1,\mathbf{x}_2,\tau) \tag{4.26}$$

We now separate the above equation into two parts

$$\begin{aligned} G(\mathbf{x}_1, \mathbf{x}_2, \omega_n) &= \frac{1}{2}\int_{-\beta\hbar}^{0} d\tau e^{i\omega_n\tau} G(\mathbf{x}_1, \mathbf{x}_2, \tau) + \frac{1}{2}\int_{0}^{\beta\hbar} d\tau e^{i\omega_n\tau} G(\mathbf{x}_1, \mathbf{x}_2, \tau) \\ &= \pm\frac{1}{2}\int_{-\beta\hbar}^{0} d\tau e^{i\omega_n\tau} G(\mathbf{x}_1, \mathbf{x}_2, \tau+\beta\hbar) + \frac{1}{2}\int_{0}^{\beta\hbar} d\tau e^{i\omega_n\tau} G(\mathbf{x}_1, \mathbf{x}_2, \tau) \\ &= \frac{1}{2}(1 \pm e^{-i\omega_n\beta\hbar})\int_{0}^{\beta\hbar} d\tau e^{i\omega_n\tau} G(\mathbf{x}_1, \mathbf{x}_2, \tau) \end{aligned} \tag{4.27}$$

It shows that $e^{-i\omega_n\beta\hbar}$ is equal to $e^{-in\pi} = (-1)^n$ (from Eq.(4.25)), and the factor $\frac{1}{2}(1 \pm e^{-i\omega_n\beta\hbar})$ reduces to

$$\frac{1}{2}(1 \pm e^{-i\omega_n\beta\hbar}) = \begin{cases} 1 & \text{if } n \text{ is even(boson) or odd(fermion)} \\ 0 & \text{if } n \text{ is odd(boson) or even(fermion)} \end{cases} \tag{4.28}$$

So, the Eq.(4.26) may be rewritten as

$$G(\mathbf{x}_1, \mathbf{x}_2, \omega_n) = \int_{0}^{\beta\hbar} d\tau e^{i\omega_n\tau} G(\mathbf{x}_1, \mathbf{x}_2, \tau) \tag{4.29}$$

where the Matsubara frequency:

$$\omega_n = \begin{cases} \frac{2n\pi}{\beta\hbar} & \text{boson} \\ \frac{(2n+1)\pi}{\beta\hbar} & \text{fermion} \end{cases} \tag{4.30}$$

To be specific, in the subsequent sections, we will explain the SCFDE technique in the context of *single-band extended Hubbard* (HB) Model for correlated electron systems, and then we only deal with *odd* Matsubara frequency for fermions in Eq.(4.30).

4.2.2 The Hubbard Model

Many theories of strongly correlated electron systems (e.g. High-Tc superconductors) begin with the Hubbard Model because of its simplicity. This is a model in which *band electrons* interact via a two-body *repulsive* Coulomb interaction.

In a *Bloch* state of energy ϵ_p, momentum $\vec{p}$, and band index α has a wave function $\Psi_{\vec{p},\alpha}$, one can construct *Wannier* state

$$\Psi_\alpha(\vec{r_i}) = \frac{1}{N}\sum_{\vec{p}\in B.Z.} e^{i\vec{p}\cdot\vec{r_i}}\Psi_{\vec{p},\alpha}(\vec{r_i}) \tag{4.31}$$

where $\vec{r_i}$ is the location of the i^{th} unit cell, B.Z. denotes 1st *Brillouin Zone* of the lattice. The assumption here will be that only one (or a few) band indices matter, so we drop the index α. The Coulomb interaction matrix elements are

$$U_{ij,i',j'} = \int d^3r_1\, d^3r_2 \Psi_i^*(\vec{r}_1)\Psi_j^*(\vec{r}_2)\tilde{V}(\vec{r}_1-\vec{r}_2)\Psi_{i'}(\vec{r}_1)\Psi_{j'}(\vec{r}_2) \tag{4.32}$$

where $\tilde{V}(\vec{r}_1-\vec{r}_2)$ is the (screened) Coulomb interaction. $U_{ij,i',j'}$ is expected to decrease rather rapidly with the separation $|i-j|$.

The second quantized Hamiltonian in the Wannier function basis is

$$\begin{aligned} H &= -\sum_{ij}\sum_{\sigma=\uparrow\downarrow}(c_\sigma^\dagger(\vec{r_i})t_{ij}c_\sigma(\vec{r_j}) + c_\sigma^\dagger(\vec{r_j})t_{ij}c_\sigma(\vec{r_i})) \\ &+ \frac{1}{2}\sum_{iji'j'}\sum_{\sigma=\uparrow\downarrow} U_{iji'j'}c_\sigma^\dagger(\vec{r_i})c_\sigma^\dagger(\vec{r_j})c_\sigma(\vec{r_{j'}})c_\sigma(\vec{r_{i'}}) \end{aligned} \tag{4.33}$$

where $c_\sigma^\dagger(\vec{r})$ ($c_\sigma(\vec{r})$ creates (annihilates) an electron at the unit cell $\vec{r}$ in the wannier state of band responsible for the Fermi surface and satisfies

$$\begin{aligned} \{c_\sigma(\vec{r}), c_{\sigma'}^\dagger(\vec{r'})\} &= \delta_{\sigma,\sigma'}\delta_{\vec{r},\vec{r'}} \\ \{c_\sigma(\vec{r}), c_{\sigma'}(\vec{r'})\} &= 0 \end{aligned} \tag{4.34}$$

The *hopping* in Eq.(4.33) is assumed to be short-range and restricted to nearest neighbor sites for simplicity:

$$t_{ij} = \begin{cases} t & \text{if } i,j \text{ are nearest neighbors} \\ 0 & \text{otherwise} \end{cases} \tag{4.35}$$

The Hubbard Model is an approximation to the more general Hamiltonian where the Coulomb interaction is assumed to be screened and only the 'on site' term is kept

$$U_{ij,i',j'} = U\delta_{ij}\delta_{i'j'}\delta_{ii'} \tag{4.36}$$

where U is the 'on site' Coulomb repulsive energy, then, we get the known single-band Hubbard Model

$$H = -t \sum_{(\vec{r},\vec{r}'),\sigma=\uparrow,\downarrow} (c^{\dagger}_{\sigma}(\vec{r})c_{\sigma}(\vec{r}') + h.c.) + U\sum_{\vec{r}} n_{\uparrow}(\vec{r})n_{\downarrow}(\vec{r}) \tag{4.37}$$

Here, we have dropped the lattice sites labeling and $(,)$ means nearest neighbor sites. This is also called the *tight-binding* approximation.

The particle number operator at site $\vec{r}$ is

$$n(\vec{r}) = \sum_{\sigma} n_{\sigma}(\vec{r}) = \sum_{\sigma} c^{\dagger}_{\sigma}(\vec{r})c_{\sigma}(\vec{r}) \tag{4.38}$$

The Hilbert space of this system is the tensor product of only $four$ states per site, i.e. $|0>$: vacuum; $|\uparrow>$: an electron with spin up; $|\downarrow>$: an electron with spin down; $|\uparrow\downarrow>$: an up-down pair. For example, for four sites system, we may denote some operations as follows:

$|-,-,-,- >= |vac > ; |\uparrow,\downarrow,-,- >= c^{\dagger}_{1\uparrow}c^{\dagger}_{2\downarrow}|vac >; |\uparrow\downarrow,-,-,- >= c^{\dagger}_{1\uparrow}c^{\dagger}_{1\downarrow}|vac >; |\uparrow,\downarrow,\uparrow,\downarrow>= c^{\dagger}_{1\uparrow}c^{\dagger}_{2\downarrow}c^{\dagger}_{3\uparrow}c^{\dagger}_{4\downarrow}|vac >$ (Half-Filled); etc;

The single-band Hubbard Model can be extended to the single-band *extended* Hubbard Model [8]-[11]

$$\begin{aligned} H &= H_t + H_v \\ &= -\sum_{j,j',\sigma} t_{j,j'} c^{\dagger}_{\sigma,j'} c_{\sigma,j} + \sum_{j,j'} \frac{1}{2} V_{j,j'} n_{j'} n_j \end{aligned} \tag{4.39}$$

Here j, j' label N sites of a finite, d-dimensional Bravais lattice with periodic boundary conditions. $t_{j,j'}$ are to include the on-site chemical potential μ, the 1st neighbor hopping (hybridization) matrix element t and, in a more realistic band structure model, the weaker 2nd and 3rd neighbor terms, t' and t'', etc. The Coulomb interaction $V_{j,j'}$, includes the on-site U and, in a more realistic model, the 1st, 2nd, ..., neighbor repulsions, etc.

4.2.3 Self-Energy and Dyson Equation

Feynman diagram properties can be represented in r-space or k-space. Here, we will restrict ourself to k-space.

The single-fermion Green's function $G(k)$ is the most basic physical quantity which can be obtained via a Feynman diagram expansion. Another important quantity is the *Self Energy*, i.e. $\Sigma(k)$. To recapitulate, $G(k)$ and $\Sigma(k)$ are defined on a domain κ of discrete points $\kappa \equiv \{i\nu, \vec{k}\}$ given by

$$\kappa := M_{-} \times B \tag{4.40}$$

where, for a finite D-dimensional lattice of size $L_1 \times L_2 \times \ ...L_D$, the Brillouin zone B is given by

$$B := \{\vec{k} = (k^1, ..., k^D | k^d = \frac{2m_d\pi}{L_d}, m_d \in \iota_d, for\ d \in \{1, ..., D\}\} \tag{4.41}$$

with

$$\iota_d := \{0, 1, ..., L_d - 1\} \tag{4.42}$$

or, alternatively

$$\iota_d := \{-int(\frac{L_d - 1}{2}), -int(\frac{L_d - 1}{2}) + 1, ..., +int(\frac{L_d}{2})\} \tag{4.43}$$

where $int(x)$:= $\max\{j | j\, integer, j \leq x\}$ for real x. i.e. the wave vector $\vec{k}$=$(k^1, ..., k^D)$ is restricted to a discrete grid in d-dimensional reciprocal space with exactly N such grid points contained in the 1st Brillouin zone B. Also, L_d denotes the integer side length of the D-dimensional finite lattice in the d-th coordinate direction. Hence, the number of lattice sites in the finite r-space lattice ι is

$$|\iota| = |B| = L_1 \times L_2 \times ... \times L_D \tag{4.44}$$

which is the same as $|B|$, the number of $\vec{k}$-points in the corresponding Brillouin zone B. The odd Matsubara frequency domain M_- is given by

$$M_- := \{i\nu | \nu = (2m_0 + 1)\pi T, m_0\, integer\} \tag{4.45}$$

where T=$1/\beta$ is the temperature of the physical system, and we let $\hbar = 1$ in Eq.(4.30).

The relationship between Green's function $G(k)$ and the Self Energy $\Sigma(k)$ is given by *Dyson* Equation

$$G(k) = \frac{1}{i\nu - \epsilon(\vec{k}) - \Sigma(k)} \tag{4.46}$$

where $\epsilon(\vec{k})$ is the non-interacting electron energy band, given by

$$\epsilon(\vec{k}) = -\mu - 2t \sum_{d=1}^{D} cos(k^d) \tag{4.47}$$

with t denoting the 1st neighbor hybridization matrix element and μ denoting the chemical potential. Both t and μ are given input parameters of the model.

One important property of the Green's function is its asymptotic behavior at large $|i\nu|$, given by

$$G(i\nu, \vec{k}) = \frac{1}{i\nu} + o(\frac{1}{i\nu})^2 \; for \; |i\nu| \to \infty \tag{4.48}$$

4.2.4 Self-Consistent Feynman Diagram Expansion

Now, the self-energy $\Sigma(k)$, in turn, is obtained *self-consistent* via a Feynman graph expansion in terms of G and the interaction potential V. As illustrated in Fig.4.1 and Fig.4.1, for order n=1 and 2, an n-th order Σ-graph consists of n non-

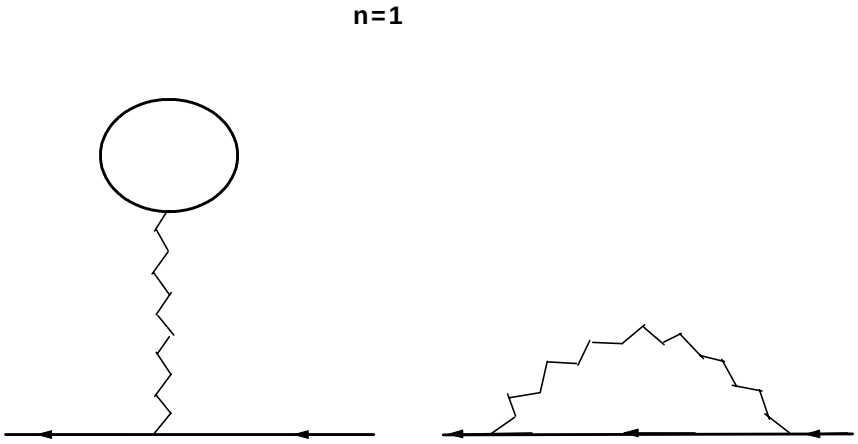

Figure 4.1: All G-irreducible Σ-graphs of n=1 order

directional wavy lines (referred to as *V-lines* hereafter) and of 2 *external* and 2n-1 *internal* directed straight lines (referred to as *G-lines* hereafter). One incoming and

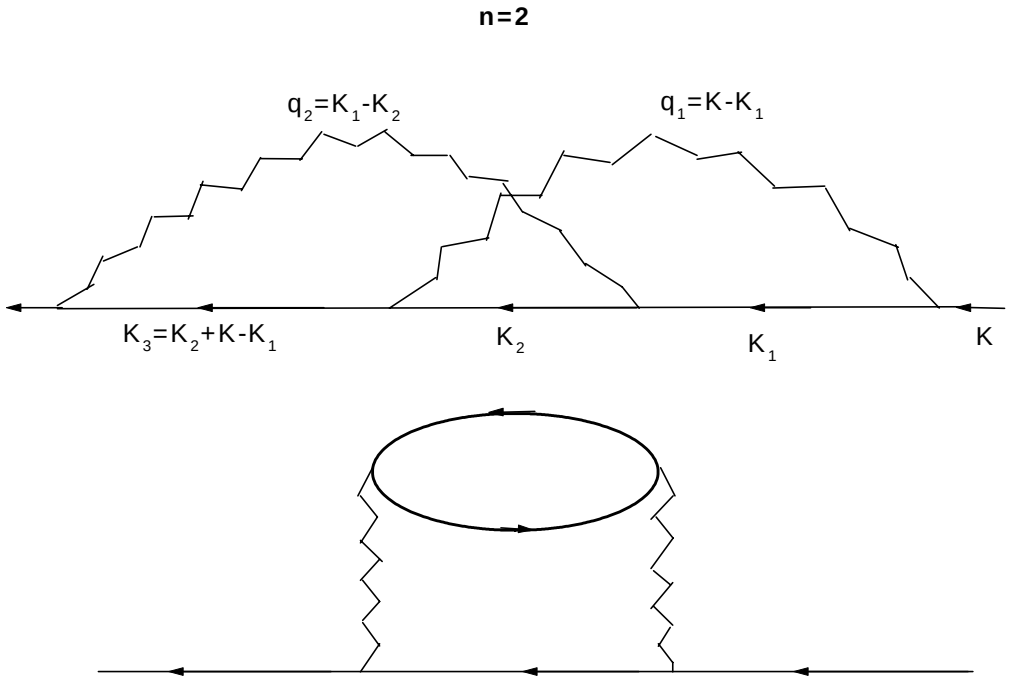

Figure 4.2: All G-irreducible Σ-graphs of n=2 order. A possible k-assignment is also shown.

one outgoing G-line is attached to each endpoint (*vertex*) of each V-line. The $\Sigma(k)$-contribution for each graph is given by the *Feynman rules* so that, for $k \equiv (\vec{k}, i\nu)$ and $k_v \equiv (\vec{k_v}, i\nu_v)(v = 1, 2, ...)$ [12, 13]

$$\Sigma(k) = \sum_{n=1}^{n_{max}} \sum_{g \in G_n} (\frac{-T}{N})^n \sum_{k_1,..,k_n \in \kappa} F_g^{(n)}(k, k_1, .., k_n) \equiv \Sigma^{(1)}(\vec{k}) + \Sigma^{(>)}(k) \qquad (4.49)$$

Here, G_n denotes the set of all topologically distinct *G-irreducible* Σ-graphs g of order n, where g is defined to be *G-irreducible (G-reducible) iff* it cannot (can) be severed into *two* disjoint pieces by cutting no more than *two* internal G-lines, as illustrated in Fig.4.3.

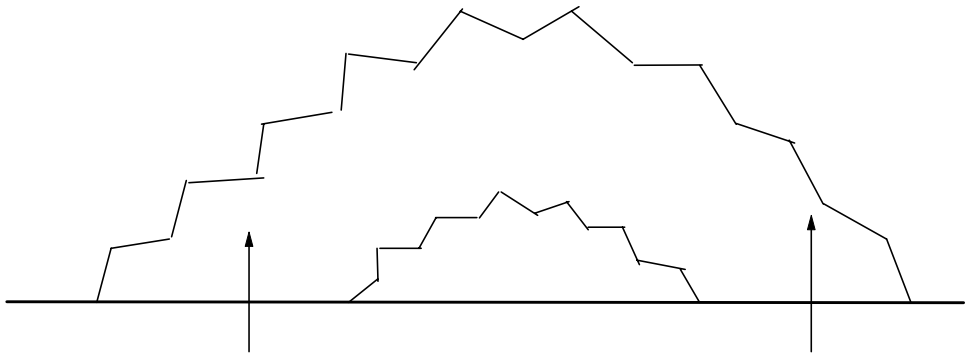

Figure 4.3: Selected G-reducible graph of n=2 order. Vertical arrows indicate the *cuts* which separate the graph into two disjoint pieces.

The $\vec{k_v}$- and $i\nu_v$- summation domains are, respectively, the set B of N k-grid points in the 1st Brillouin zone and the set M_- of odd Matsubara frequencies. $F_g^{(n)}(k, k_1, .., k_n)$ contains the internal $G-$ and $V-$ line factors of graph g, i.e.

$$F_g^{(n)}(k, k_1, .., k_n) = (-(2S_f + 1))^{m_g} exp(\delta_{n,1}, i{\nu_1}^{0+}) \prod_{u=1}^{2n-1} G(k_u) \times \prod_{x=1}^{n} V(q_x) \qquad for \;\; n \geq 1 \tag{4.50}$$

Here, the momenta k_u and q_x associated with the G-and V-lines, respectively, are determined by the graph's topology, via the momentum conservation rules at each vertex, as illustrated in Fig.(4.2). Only the first n of the internal $G-$ lines k-variables k_1, ..,k_n, can be chosen and summed over independently; The remaining $k-$

variables, k_{n+1},...,k_{2n-1}, and all q-variables, q_1,...,q_n, are linear combinations of the external k and of k_1,..,k_n. m_g denotes the number of closed $G-$ loops in graph g and S_f is the single-fermion spin quantum number, i.e. S_f=1/2 for non-spin- polarized electrons. $V(q)$ in Eq.(4.50) denotes the Fourier transform of the interaction potential V, i.e. for the lattice model Eq.(4.39), with $\vec{r}_j$ denoting the position vector of site j and $q \equiv (\vec{q}, i\omega)$

$$V(q) = \frac{1}{N} \sum_{j',j} e^{-i\vec{q}(\vec{r}_{j'} - \vec{r}_j)} V_{j',j} \tag{4.51}$$

$V(q)$ is independent of its (*even*) Matsubara frequency, $i\omega \equiv 2m_\omega i\pi T$.

The n=1 (*Hartree-Fock*) contribution in Eq.(4.49), denoted by $\Sigma^{(1)}$, depends only on the external wave vector $\vec{k}$, but not on the external frequency $i\nu$. Since, the internal frequency ($i\nu_1$) summation of the n=1 graph converges only conditionally and only in the presence of the $exp(\delta_{n,1}, i{\nu_1}^{0+})$ convergence factor, we calculate $\Sigma^{(1)}(\vec{k})$ separately.

We list some numbers of rooted, connected, irreducible diagrams of order n resulting from the *Computational Graph Theory*[14]:

n	number
1	2
2	2
3	10
4	82
5	898
6	12018
7	187626
8	3323682
9	65607682

10 1424967394

In Fig.4.4, we show the total 10 irreducible graphs for the n=3 order.

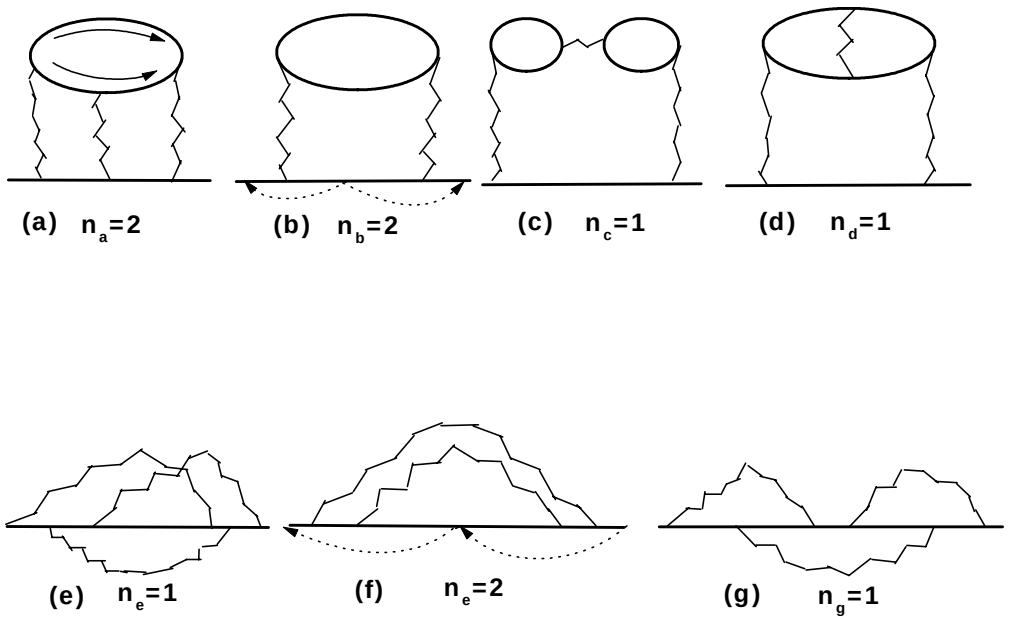

Figure 4.4: 10 G-irreducible Σ-graphs of n=3 order. In Fig.(4.4) (a), 2 different G-line directions in the loop denote 2 different diagrams. In Fig.(4.4) (b), 2 different V-line connections in the graph denote 2 different diagrams. In Fig.(4.4) (f), 2 different V-line connections in the graph denote 2 different diagrams.

Now, we are able to summarize the Self-Consistent Feynman Diagram Expansion Technique as follows:

(1) Starting from an initial guess , e.g. , $\Sigma(k)_{old}$=0.

(2) Use Dyson Eq.(4.46) to get G.

(3) Use Eq.(4.49)-Eq(4.51) to obtain $\Sigma(k)_{new}$.

(4) Check convergence:

If $\Delta\Sigma = |\Sigma(k)_{new} - \Sigma(k)_{old}| < Error$, then stop; Otherwise, using standard *Feed-Back* method to calculate the next iterate of Σ

$\Sigma_{next} = \lambda \times \ \Sigma(k)_{new} + (1 - \lambda) \times \Sigma(k)_{old}$

where λ is the feed-back parameter. Repeat step(1)- step(4), until we achieve convergence of this iteration cycle. Typically we choose values of λ in the range $\lambda \in [0, 1]$.

Chapter 5

The Applications of Self-Consistent Feynman Diagram Expansion to The Correlated Electron Models

5.1 The Hubbard Model (HB)

5.1.1 Summation of Matsubara frequency for the 1st order graph

¿From Eqs.(4.49) and (4.50), we can extract the summation part for Matsubara frequency as

$$S(\vec{k}) = \lim_{\eta \to 0^+} \frac{-T}{N} \sum_{i\nu=-i\infty}^{i\nu=i\infty} G(\vec{k}, i\nu) e^{i\nu\eta} \tag{5.1}$$

Note that Eq.(4.46) and Eq.(4.48), we take

$$G_0(k) = \frac{1}{i\nu - \epsilon(\vec{k})} \cong \frac{1}{i\nu} + \frac{A}{(i\nu)^2} \quad for\ |i\nu| \to \infty \tag{5.2}$$

Consider

$$\Delta G(\vec{k}, i\nu) = G(\vec{k}, i\nu) - G_0(\vec{k}, i\nu) \cong \frac{A - A_0}{(i\nu)^2} \sim \frac{1}{(\nu)^2} \quad for\ |i\nu| \to \infty \tag{5.3}$$

therefore

$$S(\vec{k}) = \lim_{\eta \to 0^+} \frac{-T}{N} [\sum_{i\nu=-i\infty}^{i\nu=i\infty} \Delta G(\vec{k}, i\nu) e^{i\nu\eta} + \sum_{i\nu=-i\infty}^{i\nu=i\infty} G_0(\vec{k}, i\nu) e^{i\nu\eta}] = \Delta S(\vec{k}, \eta) + S_0(\vec{k}, \eta) \tag{5.4}$$

In Eq.(5.4), the first term

$$\Delta S(\vec{k},\eta) = \frac{-T}{N}\sum_{i\nu=-i\infty}^{i\nu=i\infty} \Delta G(\vec{k},i\nu) \tag{5.5}$$

can do summation numerically with finite cut-off frequency, since $\lim_{\eta\to 0^+} e^{i\nu\eta} \to 1$.

The second term can be written as

$$\begin{aligned} S_0(\vec{k},\eta) &= \lim_{\eta\to 0^+} \frac{-T}{N}\sum_{i\nu=-i\infty}^{i\nu=i\infty} G_0(\vec{k},i\nu)e^{i\nu\eta} \\ &= \lim_{\eta\to 0^+} \frac{-T}{N}\sum_{i\nu=-i\infty}^{i\nu=i\infty} \frac{e^{i\nu\eta}}{i\nu-\epsilon(\vec{k})} \\ &= \lim_{\eta\to 0^+} \frac{-T}{N}\sum_{i\nu=-i\infty}^{i\nu=i\infty} F(i\nu) \end{aligned} \tag{5.6}$$

where

$$F(i\nu) = \frac{e^{i\nu\eta}}{i\nu-\epsilon(\vec{k})} \tag{5.7}$$

Now, introducing a function (Fermi function) $f(z) = 1/(e^{\beta z}+1)$, which has poles at $z = i\nu = (2m+1)i\pi/\beta$, and using *Residual Theorem* on the odd Matsubara frequency as shown in Fig.5.1, we can obtain[3]

$$\lim_{\eta\to 0^+}\sum_{i\nu} F(i\nu) = \frac{\beta}{e^{\beta\epsilon(\vec{k})}+1} \tag{5.8}$$

hence, Eq.(5.6) becomes

$$S_0(\vec{k}) = \lim_{\eta\to 0^+} S_0(\vec{k},\eta) = \frac{-T}{N}\frac{\beta}{e^{\beta\epsilon(\vec{k})}+1} = \frac{-1}{N}\frac{1}{e^{\beta\epsilon(\vec{k})}+1} \tag{5.9}$$

An alternative method is: instead of using Eq.(5.3), we could use

$$\Delta G(\vec{k},i\nu) = G(\vec{k},i\nu) - G_1(\vec{k},i\nu) \tag{5.10}$$

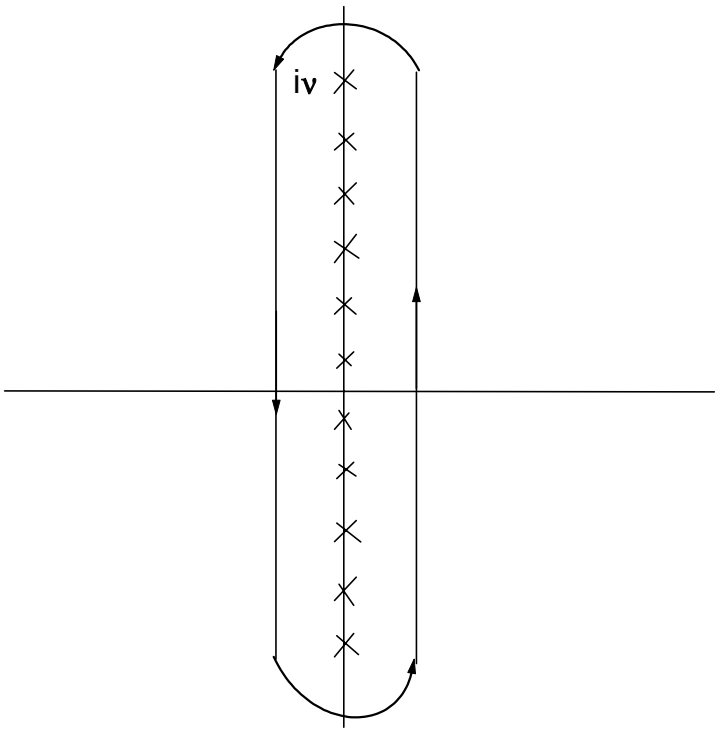

Figure 5.1: Summation of imaginary odd Matsubara frequency

with

$$G_1(\vec{k}, i\nu) := \frac{1}{i\nu - \epsilon(\vec{k}) - \Sigma^{(1)}(\vec{k})} = \frac{1}{i\nu - E(\vec{k})} \tag{5.11}$$

where

$$E(\vec{k}) := \epsilon(\vec{k}) + \Sigma^{(1)}(\vec{k}) \tag{5.12}$$

is called the 'Hartree-Fock' band. Similar to above scheme, we can do the summation numerically with finite cut-off frequency for ΔG, and do the summation analytically for G_1 and get

$$S_1(\vec{k}) = \lim_{\eta \to 0^+} S_1(\vec{k}, \eta) = \frac{-T}{N} \frac{\beta}{e^{\beta E(\vec{k})} + 1} = \frac{-1}{N} \frac{1}{e^{\beta E(\vec{k})} + 1} \tag{5.13}$$

An important physical quantity we will calculate is the average electron number for the model at each lattice site. Similar to Eq.(4.9), the average electron number is

$$\begin{aligned} \langle n \rangle = \bar{n} &= \frac{1}{N} \sum_{\vec{k},\sigma} \langle n_{\vec{k},\sigma} \rangle \\ &= \frac{1}{N} \sum_{\vec{k},\sigma} \lim_{\tau \to 0^-} G(\vec{k}, \tau) \\ &= \frac{1}{N} \sum_{\vec{k},\sigma} \lim_{\tau \to 0^-} \langle c^{\dagger}_{\vec{k},\sigma}(0) c_{\vec{k},\sigma}(\tau) \rangle \end{aligned} \tag{5.14}$$

Using the Fourier Transform of $G(\vec{k}, i\nu)$:

$$G(\vec{k}, \tau) = T \sum_{i\nu} e^{-i\nu\tau} G(\vec{k}, i\nu) \tag{5.15}$$

we get

$$\begin{aligned} \langle n \rangle &= \frac{T}{N} \lim_{\tau \to 0^-} \sum_{\vec{k},\sigma} \sum_{i\nu} e^{-i\nu\tau} G(\vec{k}, i\nu) \\ &= \frac{T}{N} \sum_{\vec{k},\sigma} \lim_{\tau \to 0^-} \{ \sum_{i\nu} e^{-i\nu\tau} [G(\vec{k}, i\nu) - G_1(\vec{k}, i\nu)] + \sum_{i\nu} e^{-i\nu\tau} G_1(\vec{k}, i\nu) \} \end{aligned} \tag{5.16}$$

For the procedures of Eq.(5.1)-Eq.(5.13) we have employed, we may do the first summation term in Eq.(5.16) numerically with finite cut-off frequency and analytically get the second summation term as the Fermi function form. Note that the summation for σ in Eq.(5.16) will lead to factor "2" for the electron.

5.1.2 Some Results for the HB Model

We perform our calculations on the 2-dimensional lattice with size $L_1 \times L_2 = 4 \times 4$. For simplicity, we choose the parameter $t = 1$ and only consider the on-site interaction, i.e.

$$V(q) = U \tag{5.17}$$

The *error* (the convergence criterion of the iteration procedure) on the first line of Page 66 was set to be 10^{-5}. We consider the *Half-Filled* case, i.e. we set the chemical potential to be $\mu = U/2$, the expected average electron number (Eq.(5.16)) should be 1.

Fig.5.2 shows the results of the $n = 2$ order for the $\Delta\Sigma = |\Sigma(k)_{new} - \Sigma(k)_{old}|$ at 5 different temperatures (in order to plot it with appropriate scale in the figure, we divide $\Delta\Sigma$ by the value of first iteration $\Sigma(k)_{new}|_{t=1}$). We can see the higher the temperature, the faster the convergence of the iteration procedure. At very low temperature T=0.05, its behavior is very strange, revealing the possible important dynamical characteristics of the electron. This can also be seen in the similar behavior of the average electron number as shown in Fig.5.3.

Fig.5.4 shows results of $n = 2$ order with three different feed-back convergent parameters. The behavior of $\Delta\Sigma$ and $\langle n \rangle$ are different between them. The small figure in the plot is the self-energy Σ_2 including the real part ($Re\Sigma_2$) and imaginary part ($Im\Sigma_2$). We can see that they converge to the same values with those three different convergent parameters.

Fig.5.5 and Fig.5.6 are the results for the self-energy $Im\Sigma$ and $Re\Sigma$ with maximum $n = 3$ order considered. In the figure, the notation "$n_1.n_2$"($n_1 = 2, 3; n_2 = 2, 3$) means the n_1 order term's result when maximum n_2 order is considered. Fig.5.7 and Fig.5.8 are the results with the same U and μ but a *lower* temperature. The features

at T=1.8 and T=0.5 are a little bit different. From the figures, we can see the results of $\Sigma_{2.2}$ and $\Sigma_{2.3}$ is very close. It is obviously reasonable.

5.2 The Anderson Impurity Model (AIM)

5.2.1 Anderson Impurity Model

The Anderson Impurity Model (AIM)[15]-[18] is the archetype for describing dilute, correlated magnetic impurities in metals. With the Fermi level taken as the energy origin, the Hamiltonian for the spin-1/2 AIM is given in standard notation by

$$\begin{aligned} H &= H_{host} + H_{impurity} + H_{hybridization} \\ &= \sum_{\vec{k},\sigma} \epsilon_{\vec{k}} c^{\dagger}_{\vec{k}\sigma} c_{\vec{k}\sigma} + \sum_{\sigma} (\epsilon_i + \frac{1}{2} U n_{i-\sigma}) n_{i\sigma} + \sum_{\vec{k},\sigma} V_{i\vec{k}} (c^{\dagger}_{i\sigma} c_{\vec{k}\sigma} + c^{\dagger}_{\vec{k}\sigma} c_{i\sigma}) \end{aligned} \tag{5.18}$$

The first term in H refers to the host band of non-interacting electrons with dispersion $\epsilon_{\vec{k}}$ and $c^{\dagger}_{\vec{k}\sigma}(c_{\vec{k}\sigma})$ creates (annihilates) an electron in the conduction band in a Bloch state with wave vector $\vec{k}$ and spin σ. The second term refers to the single impurity i with on-site Coulomb interaction U and on-site energy ϵ_i. $n_{i\sigma} = c^{\dagger}_{i\sigma} c_{i\sigma}$ measures the occupation at impurity site i for spin σ. The final term describes the one-electron hybridization between the impurity and host, $c^{\dagger}_{i\sigma}(c_{i\sigma})$ creates (annihilates) an electron with spin σ at a single impurity site i. Here, we only study the particle-hole (p-h) symmetric AIM where $\epsilon_i = -U/2$ and the impurity charge $n_i = \sum_{\sigma} \langle n_{i\sigma} \rangle = 1$ for all U.

The AIM here can also be studied by the SCFDE technique. The *impurity* Green's function may be written as

$$G(i\nu) = \frac{1}{i\nu + i\Gamma sgn(\nu) - \epsilon_i - \Sigma^{(1)} - \Delta\Sigma(i\nu)} \tag{5.19}$$

Hence, as in Hubbard Model, we may write

$$\Delta G(\vec{k}, i\nu) = G(\vec{k}, i\nu) - G_r(\vec{k}, i\nu) \tag{5.20}$$

with

$$G_r(i\nu) = \frac{1}{i\nu + i\Gamma sgn(\nu) - E_0} \tag{5.21}$$

and

$$E_0 = \epsilon_i + \Sigma^{(1)} \tag{5.22}$$

Then the summation term $\sum_{i\nu} \Delta G(\vec{k}, i\nu)$ can be numerically obtained with finite cut-off frequency, since $\Delta G(\vec{k}, i\nu) \sim \frac{1}{(i\nu)^3}$ for $i(\nu) \to \infty$. For the second term

$$S_r = \sum_{i\nu} G_r(i\nu) e^{-i\nu\tau} \tag{5.23}$$

We can solve it analytically by using the *Residual Theorem*. Eq.(5.21) can be analytically continued as $(i\nu \to z)$

$$G_r(z) = \frac{1}{z - (E_0 - i\Gamma)} \quad for\ \nu > 0 \tag{5.24}$$

with a pole at $z^+ = E_0 - i\Gamma$, and

$$G_r(z) = \frac{1}{z - (E_0 + i\Gamma)} \quad for\ \nu < 0 \tag{5.25}$$

with a pole at $z^+ = E_0 + i\Gamma$. Doing some computations, we will get

$$\begin{aligned} S_r &= S_{r1} + S_{r2} \\ &= \Big(\sum_{i\nu,\nu>0} G_r^+(i\nu) e^{-i\nu\tau}\Big) + \Big(\sum_{i\nu,\nu<0} G_r^-(i\nu) e^{-i\nu\tau}\Big) \end{aligned}$$

$$= \frac{-1}{T}[\frac{1}{\pi}arctg(\frac{A+E_0}{\Gamma}) - \frac{1}{2}] + \frac{\Gamma}{\pi T}\int_{-A}^{A} F(x)\,dx \tag{5.26}$$

where

$$F(x) = \frac{f(x)}{(x-E_0)^2 + \Gamma^2} \tag{5.27}$$

with $f(x) = \frac{1}{e^{\beta x}+1}$, the Fermi function. The constant $A \gg E_0, \Gamma, T$ should be satisfied.

The average electron number is

$$\langle n \rangle = \frac{2T}{N}\sum_{\vec{k}}\sum_{i\nu} G(\vec{k}, i\nu)e^{-i\nu\tau} \tag{5.28}$$

The integration in Eq.(5.26) can be done numerically by *Simpson's rule*[19]: Assume we need to get

$$S = \int_a^b f(x)\,dx \tag{5.29}$$

then

(1)calculating the following quantity by using *trapezoid rule*:

$T_n = h\frac{f(a)+f(b)}{2}$, with $n = 1, h = b - a$

(2)calculating $T_{2n} = \frac{1}{2}T_n + \frac{h}{2}\sum_{k=0}^{n-1} f(x_k + \frac{h}{2})$

(3)Using *Simpson's rule* to calculate

$S_{2n} = \frac{4T_{2n}-T_n}{3}$

(4) If $|S_{2n} - S_n| < \zeta$, stop; Otherwise, set $2n \Rightarrow n, \frac{h}{2} \Rightarrow h$, repeat (2) and (3).

5.2.2 Some Results for the AIM Model

In the following calculations, we find that there is no difference for the integration term in Eq.(5.26) between $A = 10$ and $A = 20$. We will take $A = 10$. The other parameters are set to be $\Gamma = 1$, $\zeta = 10^{-6}$.

We first present the calculation results of Feynman diagram expansion of $n = 2$ order. Fig.5.9 shows $\langle n \rangle$ as a function of iteration step at $T = 0.05$ and for 5 different U. We can see that the higher the U, the slower the convergence when T is fixed. Fig.5.10 and Fig.5.11 are corresponding results of self-energy $Re\Sigma$ and $Im\Sigma$ under the same conditions as in Fig.5.9, the $Re\Sigma$ part can be regarded as zero, and the higher the U, the larger the amplitude of $Im\Sigma$. Fig.5.12 is the required *number* of trapezoids (denoted by n_l in the figure) in order to get $\zeta = 10^{-6}$ in the calculation of integration in Eq.(5.26) for Fig.5.9-Fig.5.11.

Whether an iteration procedure is *convergent, divergent*, or *limit cycle* depends on the feed-back parameter. Fig.5.13 illustrates two λ values' results: one is convergent, the other is divergent.

Fig.5.14, Fig.5.15, and Fig.5.16 give the plots of $\langle n \rangle - t$, $Re\Sigma$ and $Im\Sigma$ with $n = 2$ at different cut-off Matsubara frequency, respectively. As above, the $Re\Sigma$ part can be regarded as zero, and different features of $Im\Sigma$ can be seen in the figures.

Fig.5.17 (T=0.5), Fig.5.18 (T=0.05), and Fig.5.19 (T=0.008), are respectively the calculation results of $Im\Sigma$ at 3 different temperature with the same cut-off Matsubara frequency $L_0 = 100$ and the maximum Feynman diagram order $n = 3$. The $Im\Sigma$ can show us different features around $\omega = 0$. Note that many interesting physical quantities (e.g. mass enhancement factor on the Fermi surface) are related to the self-energy or its derivative[20, 21].

5.3 References

[1] P.Fulde, Electron Correlations in Molecules and Solids, 3rd edn., Springer Ser. Solid-State Sci. (Springer, Berlin, Heidelberg, 1995).

[2] G.D.Mahan, Many-Particle Physics, 2nd edn., (Plenum Press, New York, 1990).

[3] A.L.Fetter, J.D. Walecka, Quantum Theory of Many-Particle Systems, (McGraw-Hill, New York, 1971).

[4] E. Fradkin, Field Theories of Condensed Matter Systems, (Addison-Wesley Publishing Company, 1991).

[5] J.Gonzalez, M.A.Martin-Delgado, G.Sierra, A.H.Vozmediano, Quantum Electron Liquids and High-Tc Superconductivity, Springer, (Springer, Berlin, Heidelberg, 1995).

[6] R.D. Mattuck, A Guide to Feynman Diagrams in the Many-Body Problem, 2nd edn. (McGraw-Hill, New York, 1976).

[7] The Hubbard Model: its Physics and Mathematical Physics, eds. D. Baeriswyl, D.K.Campbell, J.M.P.Carmelo, F.Guinea, E.Louis, (Plenum Press, New York, 1995).

[8] J.Hubbard, Proc. Roy. Soc. (London) A, **276** 238(1963).

[9] H.-B. Schüttler, A.J. Fedro, Phys. Rev. B **45** 7588(1992).

[10] C.-X. Chen, H.-B. Schüttler, Phys. Rev. B **43** 3771(1991).

[11] C.-X. Chen, H.-B. Schüttler, A.J. Fedro, Phys. Rev. B **41** 2581(1990).

[12] H.-B. Schüttler, Screening in Strongly Correlatd Electron Systems, NSF Proposal, DMR-9970291.

[13] H.-B. Schüttler, J.N.Corcoran, D.K.Lowenthal, R.W.Robinson, Summation of High-order Feynman Graph Expansions, NSF Proposal, ITR-0081789.

[14] R.W. Robinson, Seminar talk .

[15] P.W. Anderson, Phys. Rev. **124** 41(1961).

[16] D.E. Logan, M.T. Glossop, J. Phys.: Condens. Matter,**12** 985(2000).

[17] S. Schafer, D.E. Logan, Phys. Rev. B **63** 045122(2001).

[18] N.L. Dickens, D.E. Logan, J. Phys.: Condens. Matter,**13** 4505(2001).

[19] S.-L. Xu, The Common Algorithms in Fortran, TsingHua University Press, Beijing, 1991.

[20] K. Yonemitsu, J. Zhong, H.-B. Schüttler, Phys. Rev. B **59** 1444(1999).

[21] S. Moukouri, C. Huscroft, M. Jarrell, 53(2000), Computer Simulations in Condensed Matter Physics VII eds. D.P. Landau, S.P. Lewis and H.B. Schüttler (Berlin:Springer).

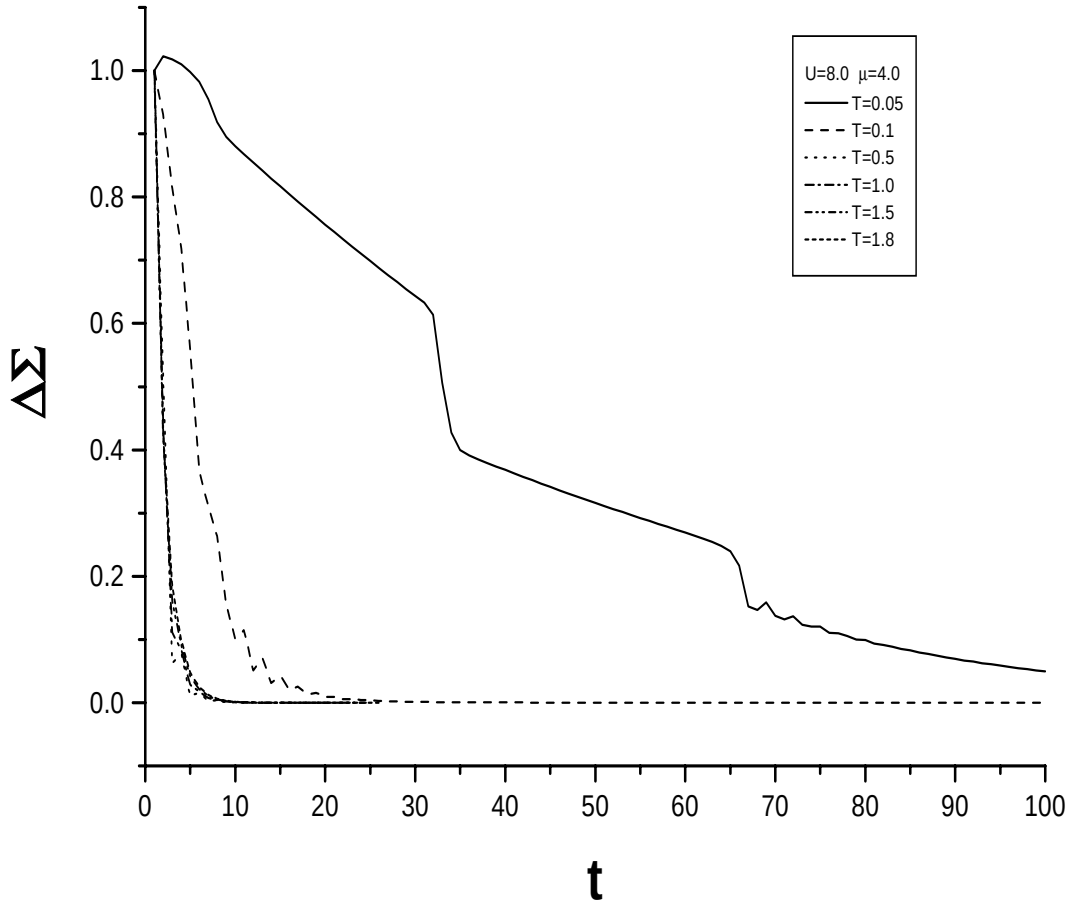

Figure 5.2: Behavior of $\Delta\Sigma = |\Sigma(k)_{new} - \Sigma(k)_{old}|$ at 5 different temperatures with U=8.0, μ=4.0. t is the iteration number. n=2. Note that in order to plot it with appropriate scale in the figure, we divide $\Delta\Sigma$ by the first iteration $\Sigma(k)_{new}|_{t=1}$.

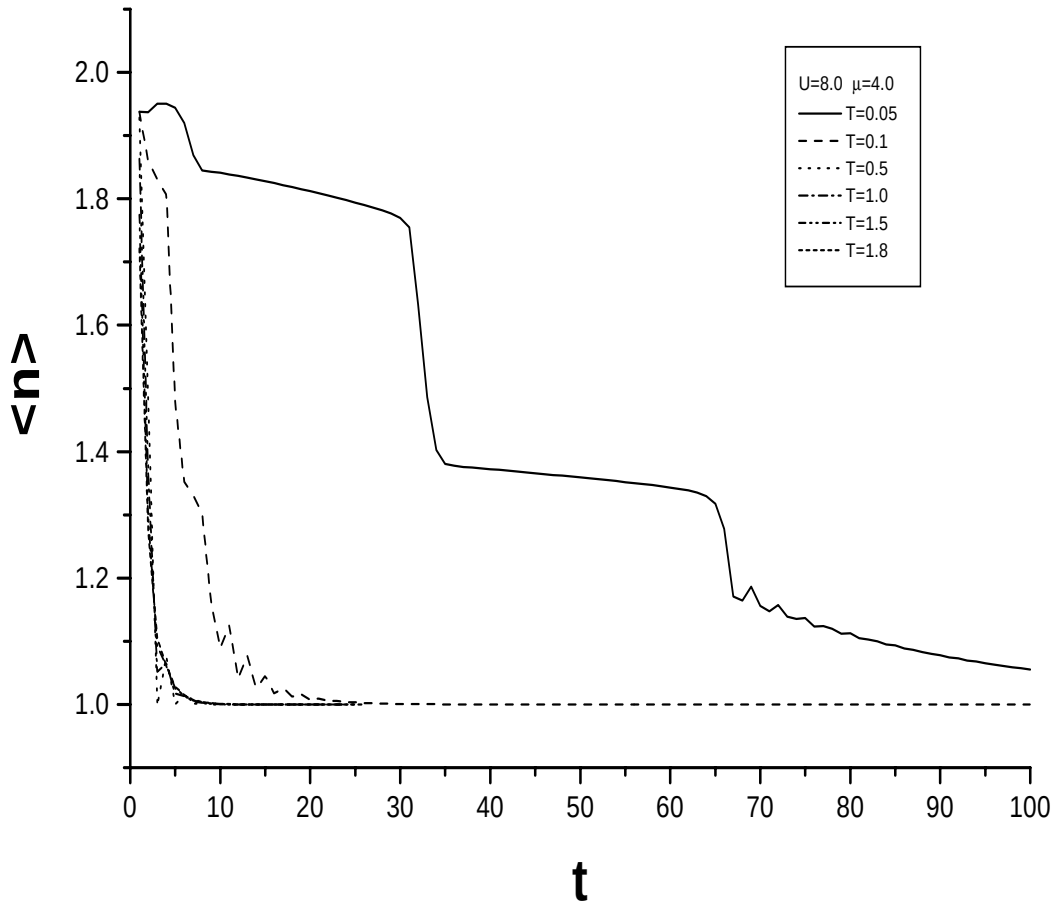

Figure 5.3: Behavior of average electron number at 5 different temperatures with U=8.0, μ=4.0. t is the iteration number. n=2.

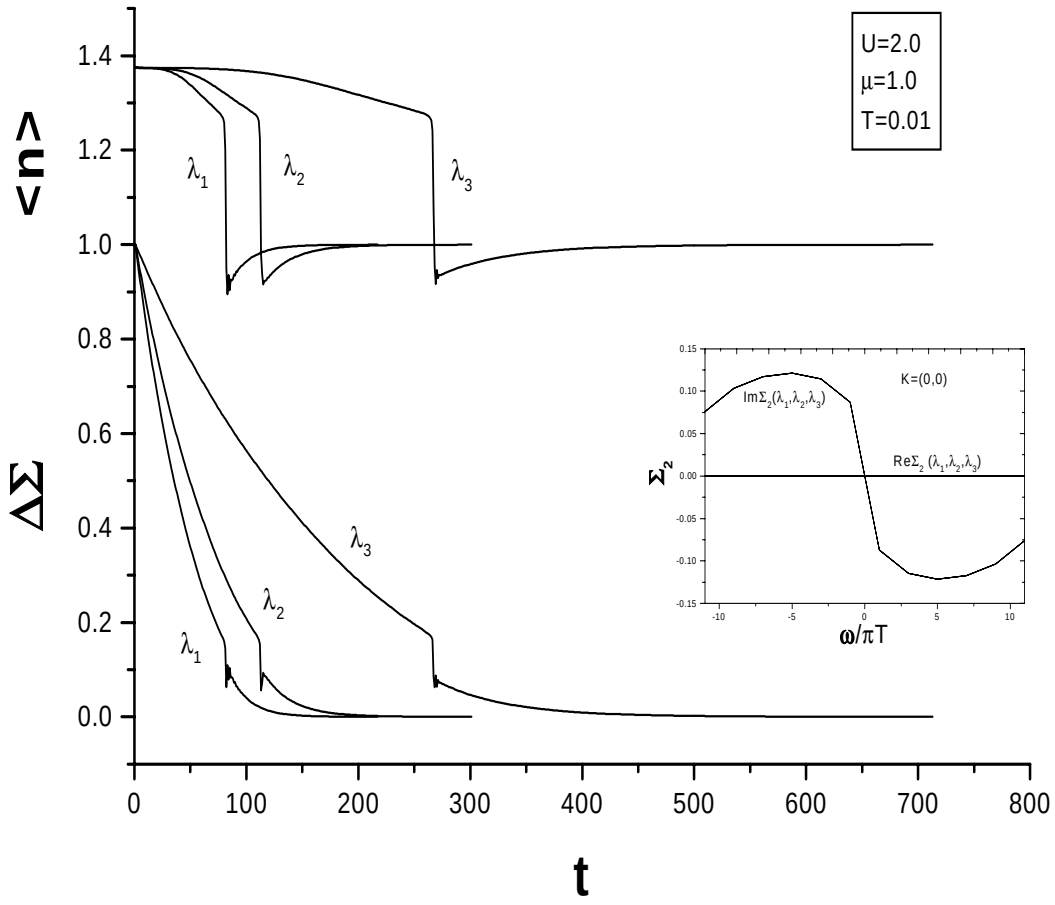

Figure 5.4: Behavior of $\Delta\Sigma$, $\langle n \rangle$, and Σ_2 with three different feed-back convergent parameters. n=2. See text for details. Note that in order to plot it with appropriate scale in the figure, we divide $\Delta\Sigma$ by the first iteration $\Sigma(k)_{new}|_{t=1}$.

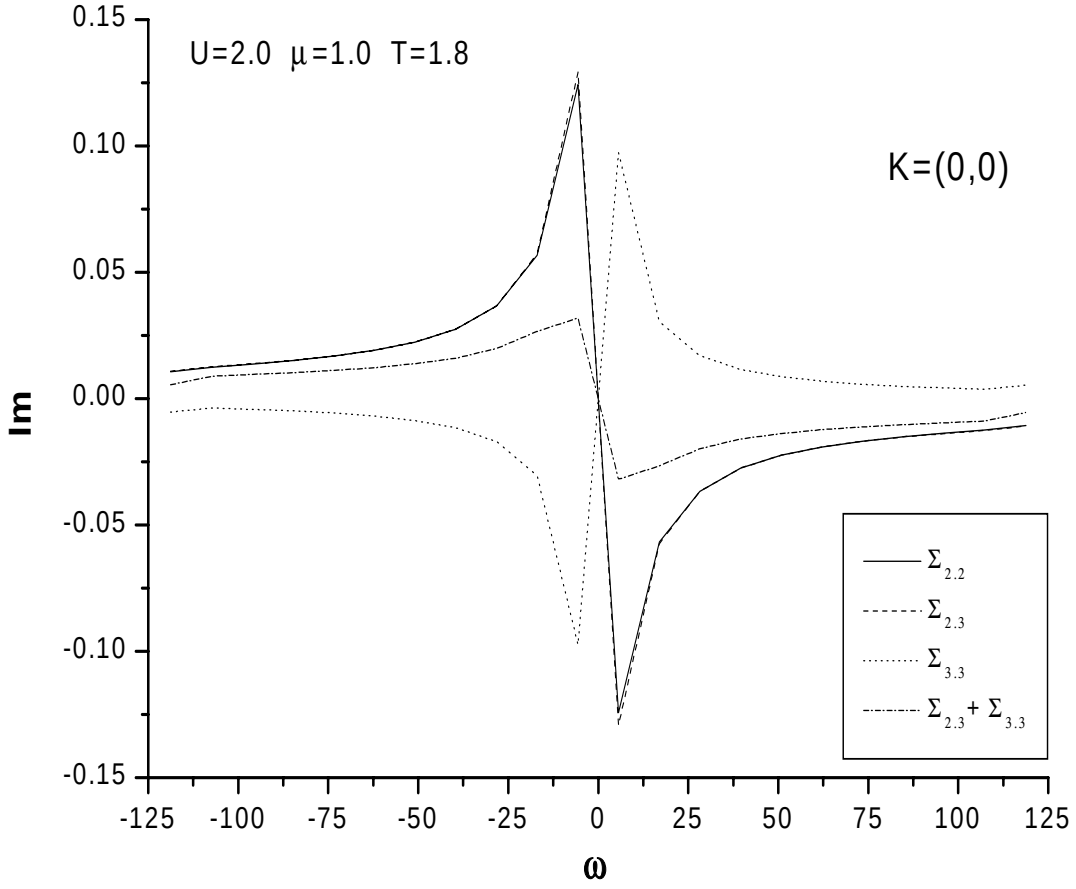

Figure 5.5: Imaginary part of Σ when maximum $n = 3$ order is considered in the computations. See text for details.

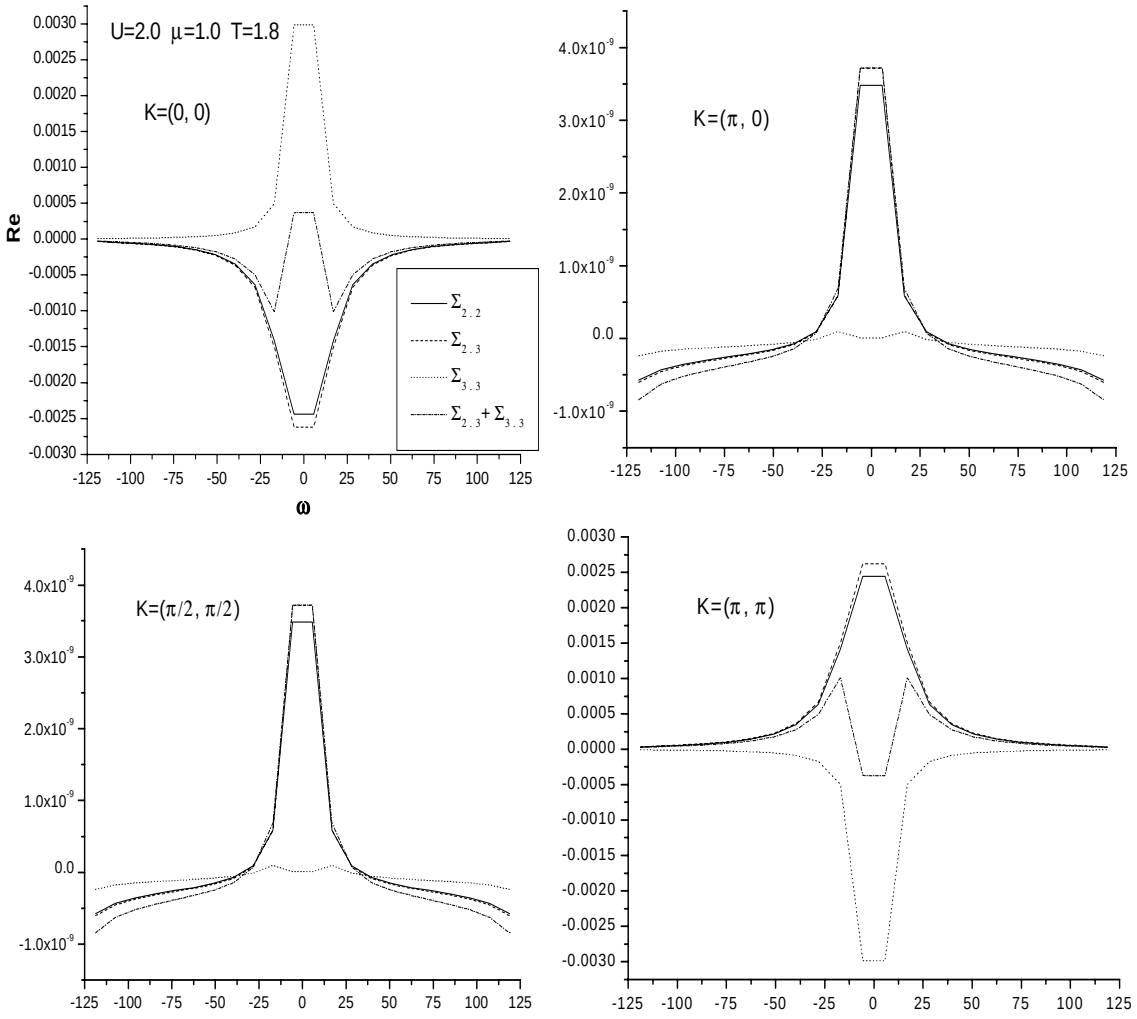

Figure 5.6: Real part of Σ when maximum $n = 3$ order is considered in the computations. See text for details.

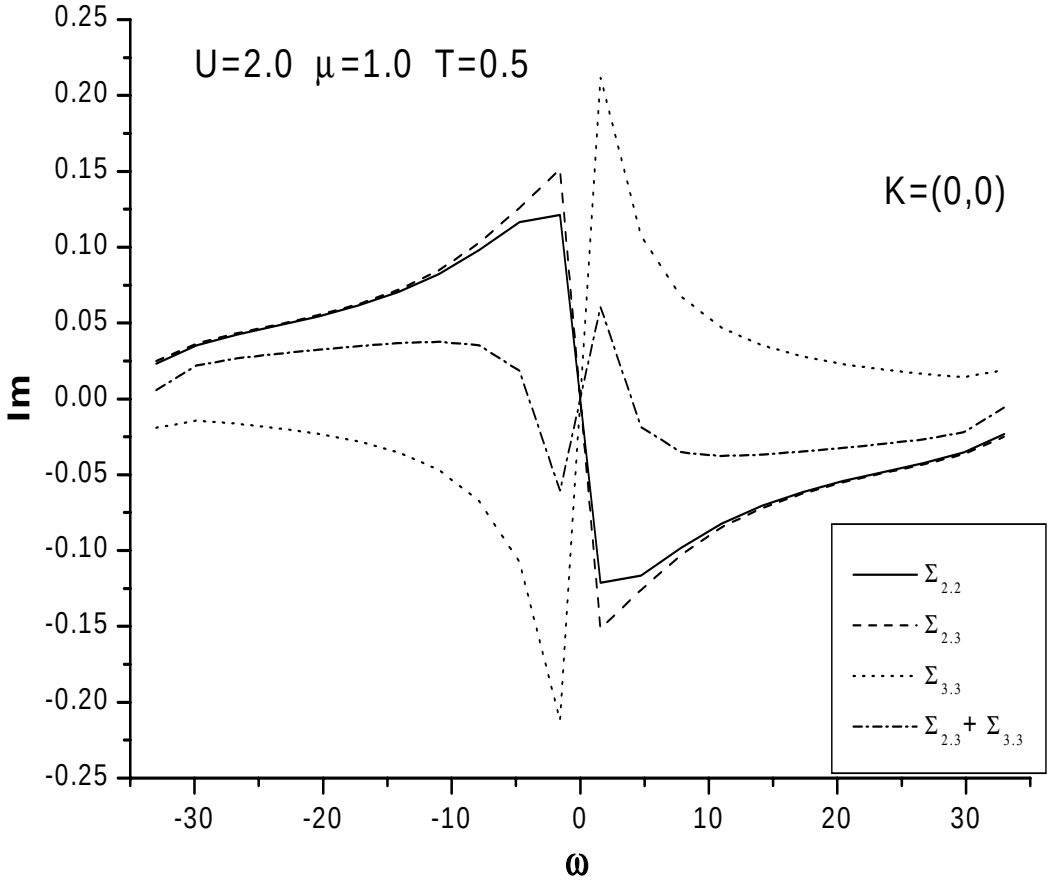

Figure 5.7: Imaginary part of Σ at a *lower* temperature when maximum $n = 3$ order is considered in the computations. See text for details.

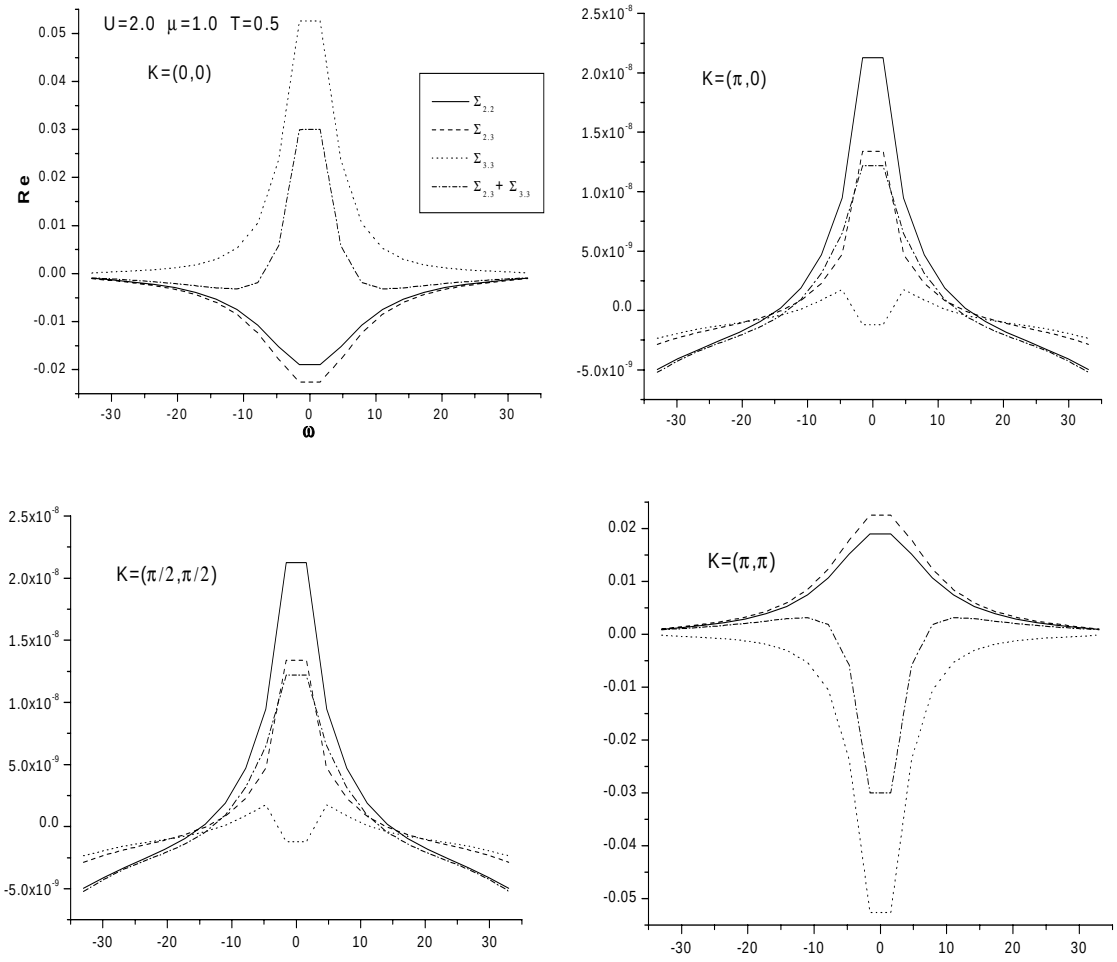

Figure 5.8: Real part of Σ at a *lower* temperature when maximum $n = 3$ order is considered in the computations. See text for details.

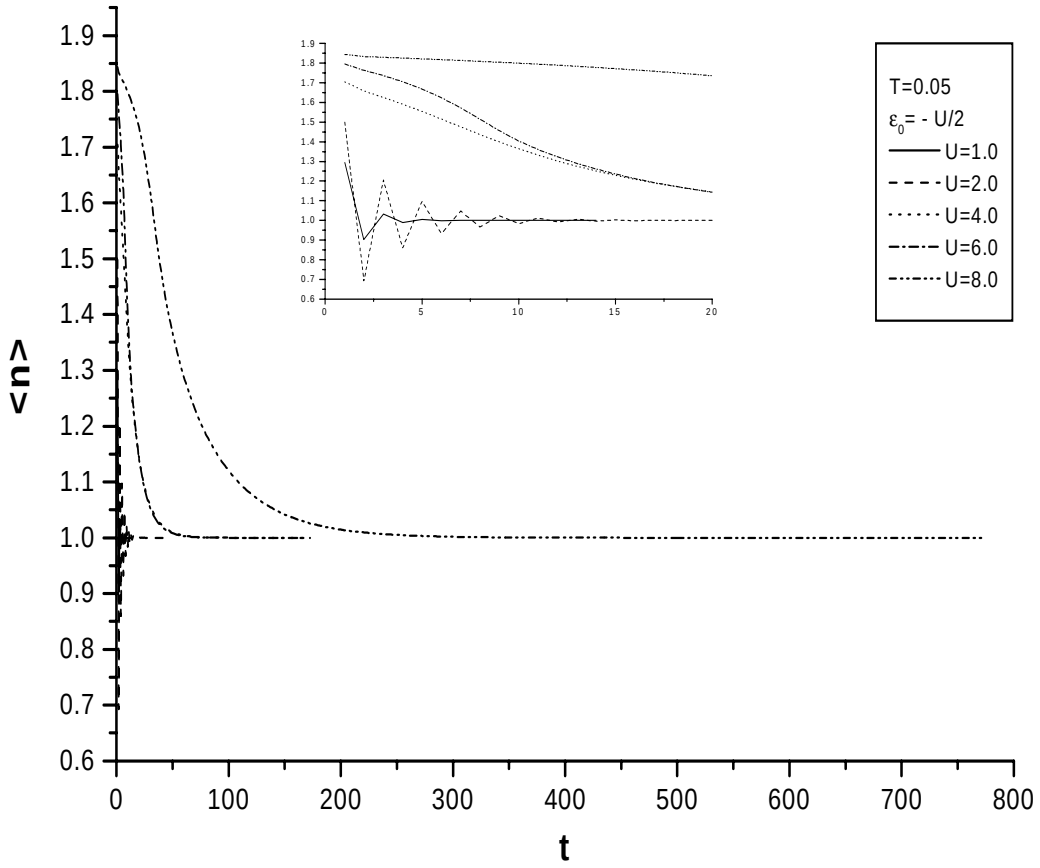

Figure 5.9: Behavior of average electron number at 5 different U with T=0.05. t is the iteration number. n=2.

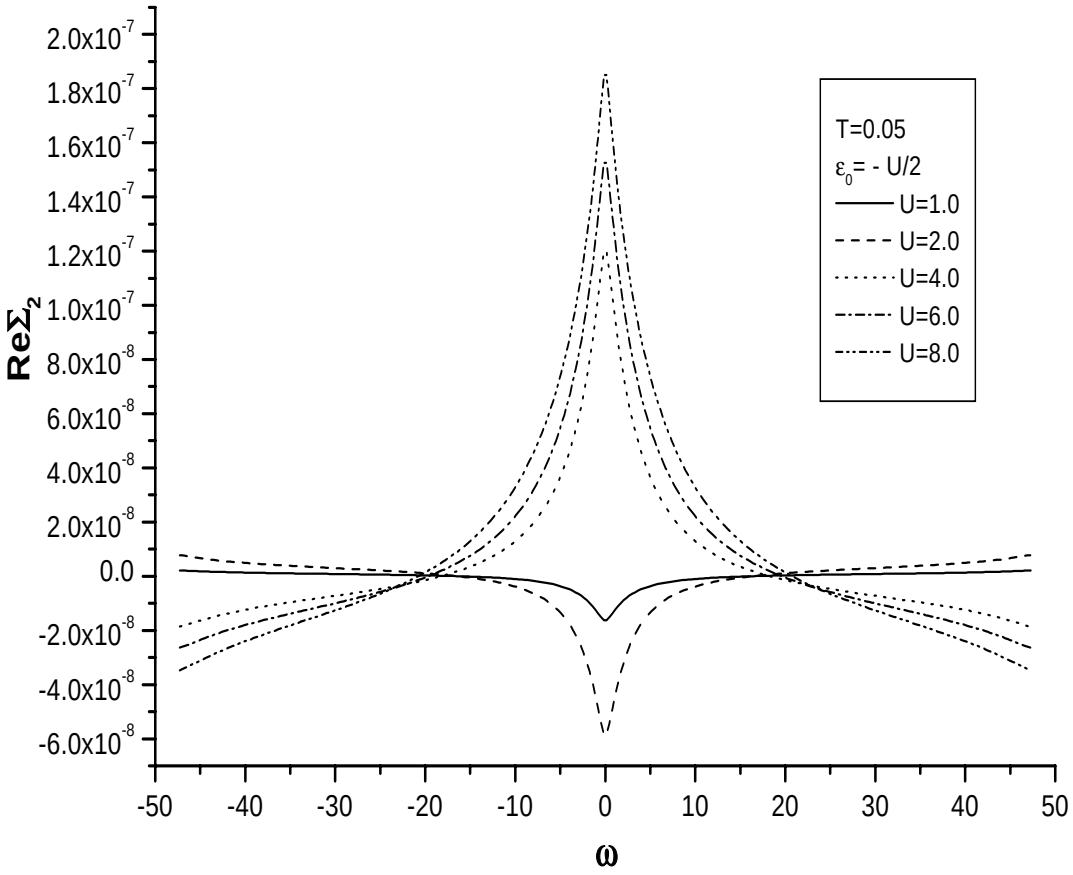

Figure 5.10: Real part of Σ when $n = 2$ order is considered in the computations.

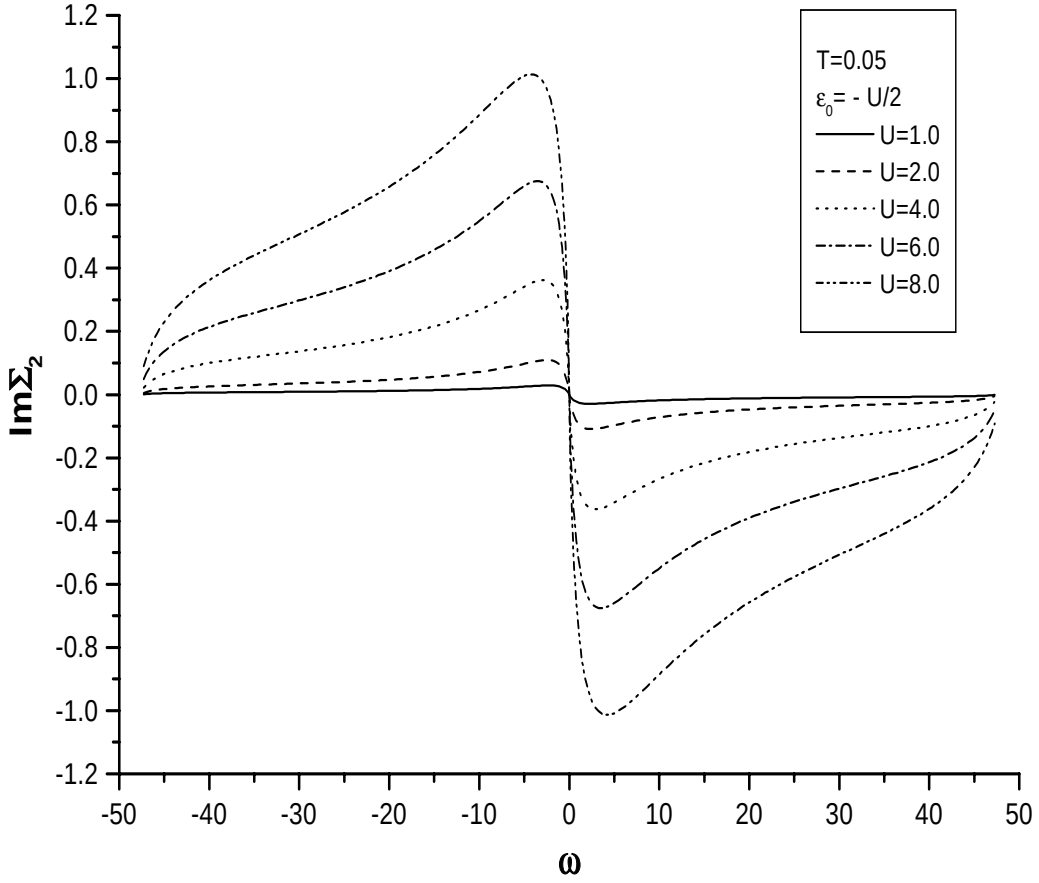

Figure 5.11: Imaginary part of Σ when $n = 2$ order is considered in the computations.

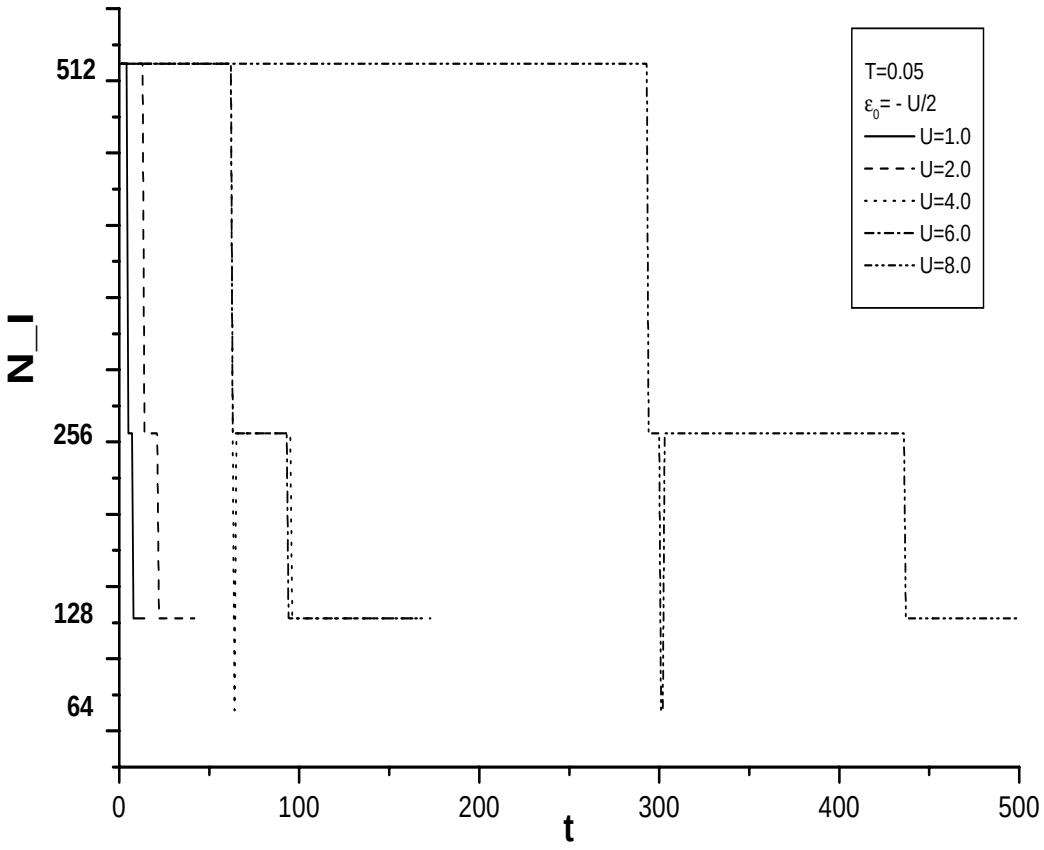

Figure 5.12: The required *number* of trapezoids in order to get $\zeta = 10^{-6}$ in the calculation of integration in Eq.(5.26) for Fig.5.9-Fig.5.11.

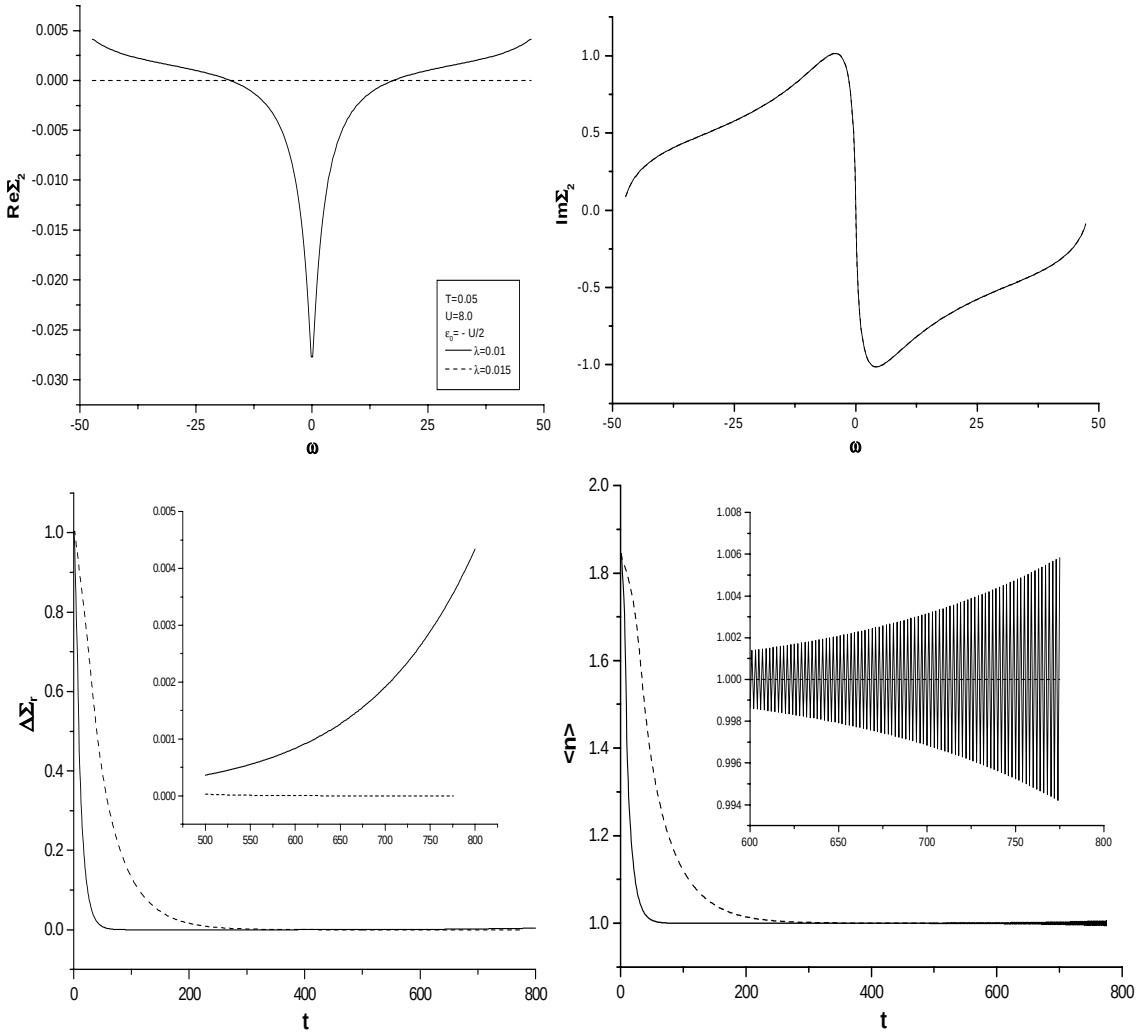

Figure 5.13: Illustration of two λ values' result: one is convergent (dotted line), the other is divergent (real line).

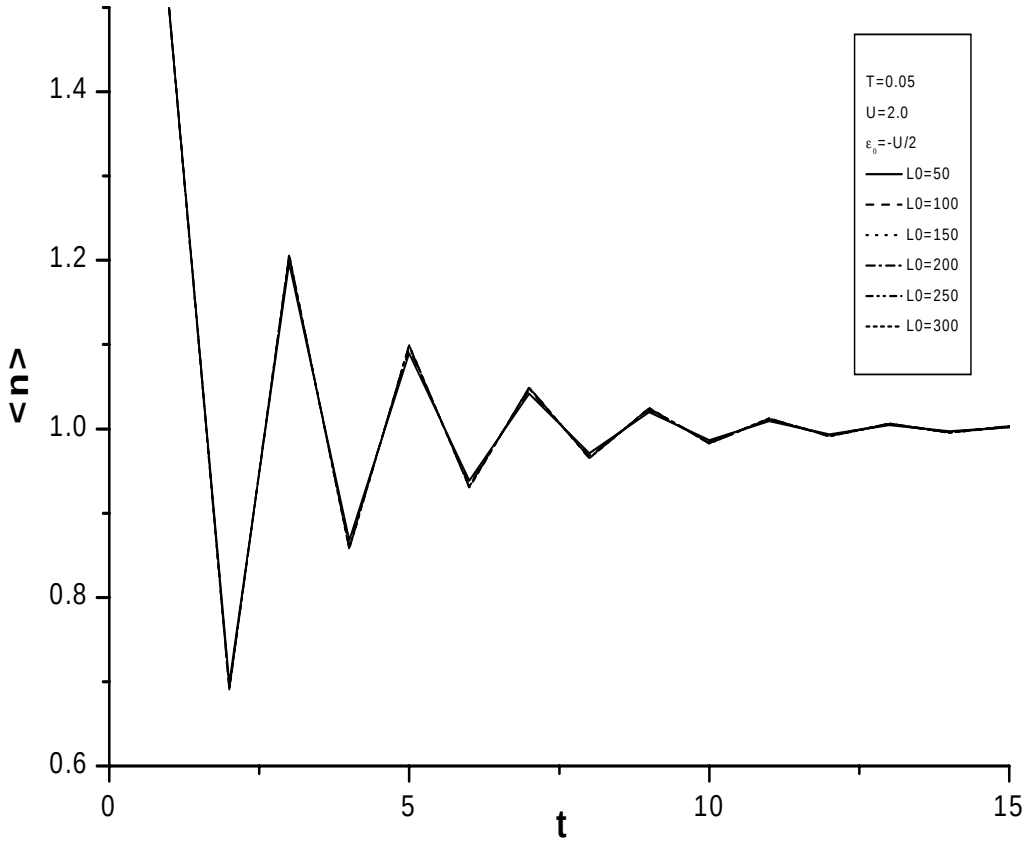

Figure 5.14: Behavior of average electron number at 5 different cut-off L_0. t is the iteration number. n=2.

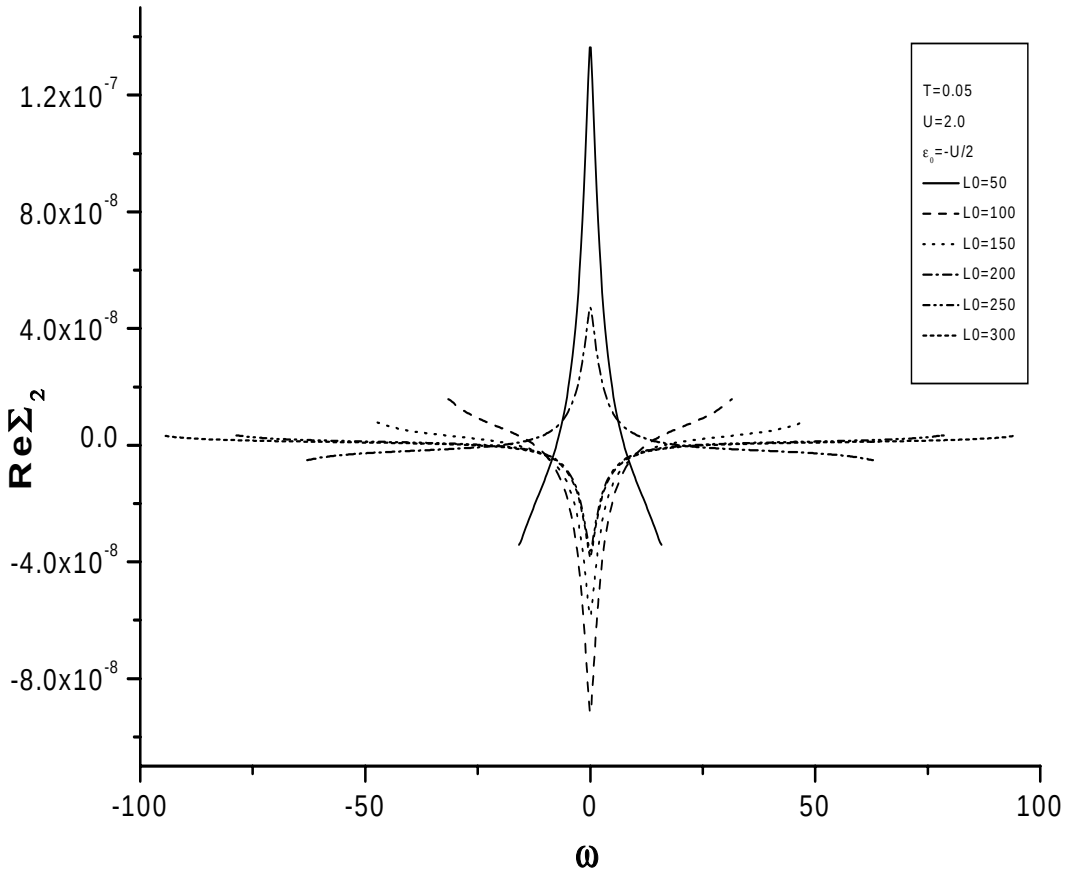

Figure 5.15: Real part of Σ when $n = 2$ order is considered with 5 different cut-off L_0 in the computations.

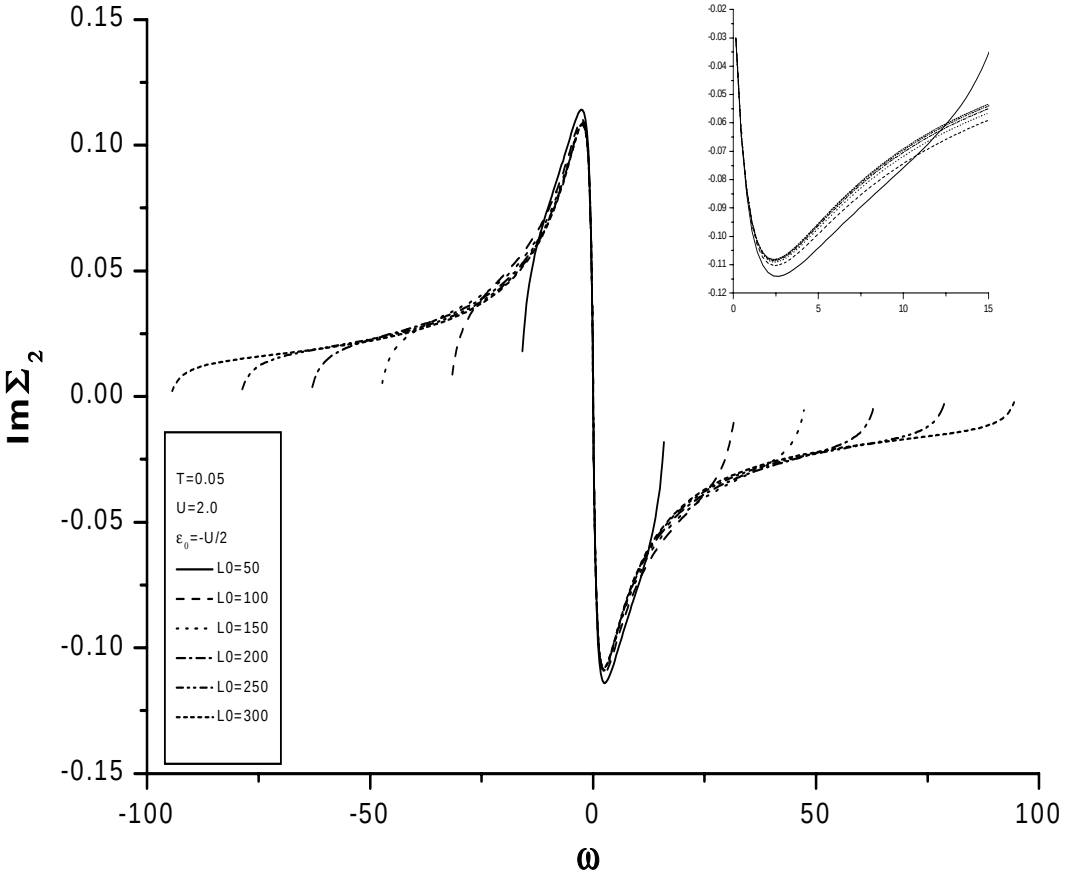

Figure 5.16: Imaginary part of Σ when $n = 2$ order is considered with 5 different cut-off L_0 in the computations.

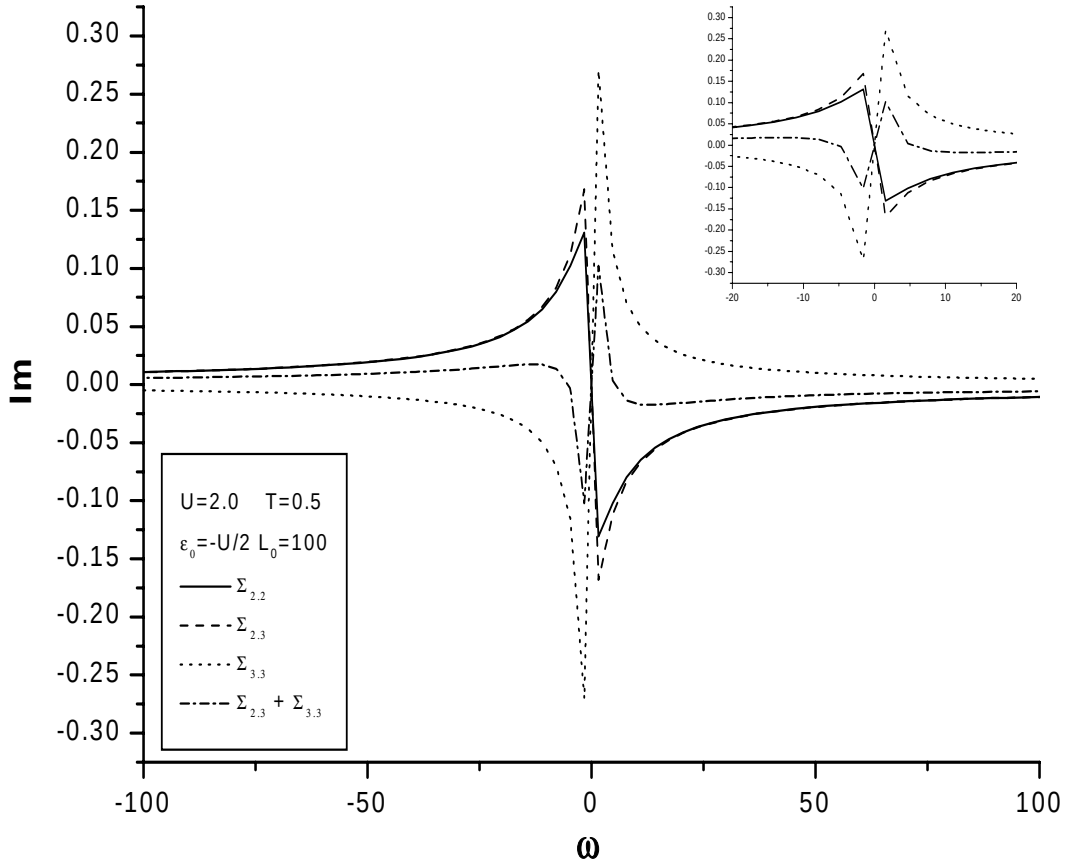

Figure 5.17: Imaginary part of Σ when maximum $n = 3$ order is considered at T=0.5 in the computations. See similar notations in HBM.

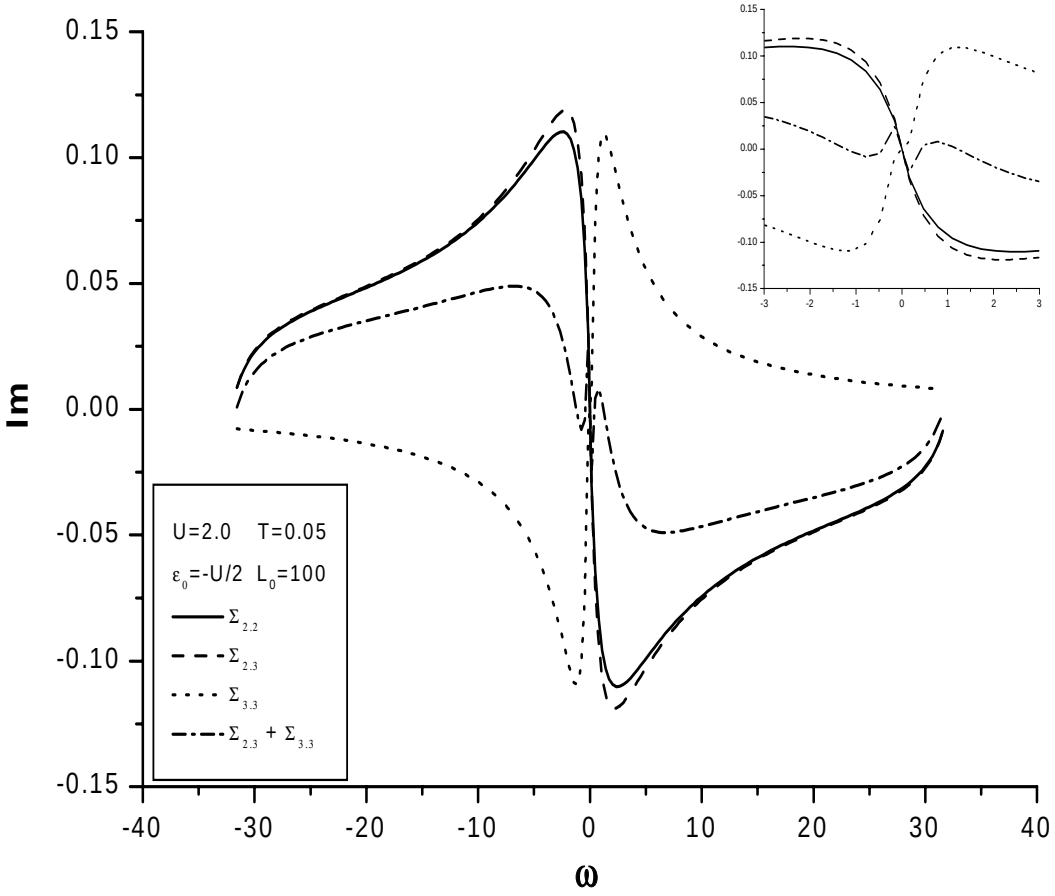

Figure 5.18: Imaginary part of Σ when maximum $n = 3$ order is considered at T=0.05 in the computations. See similar notations in HBM.

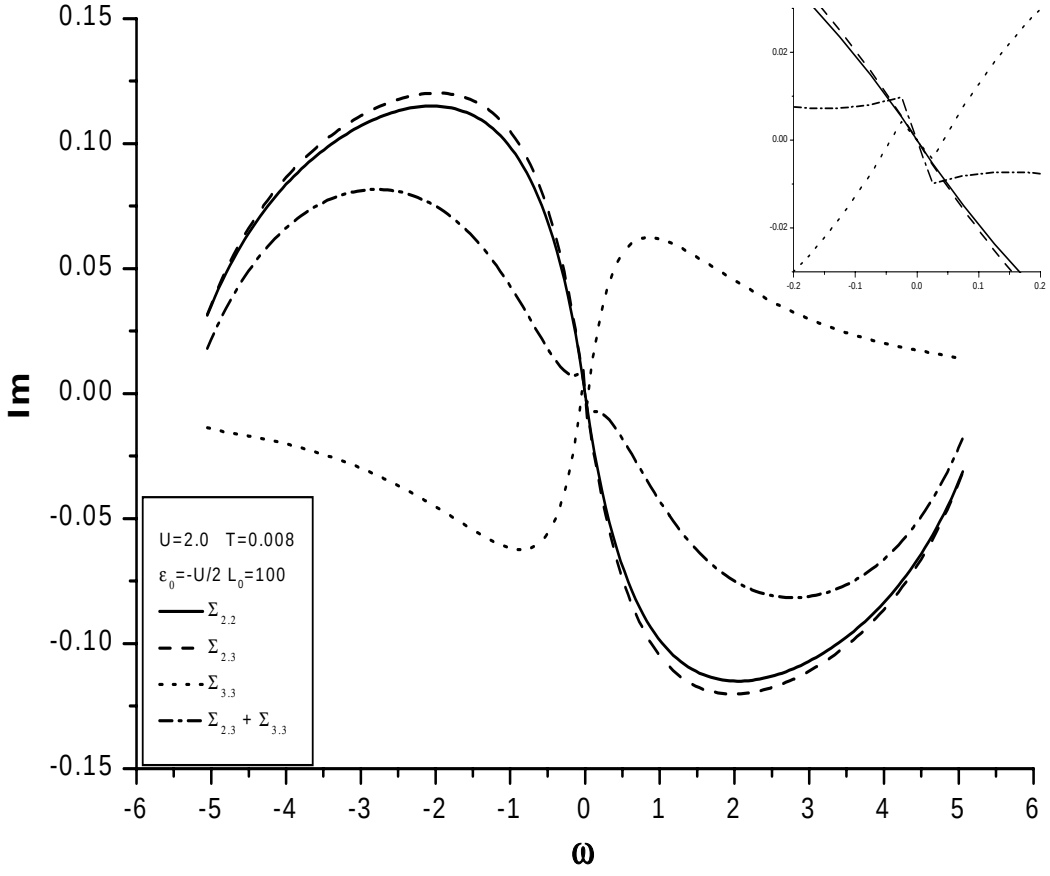

Figure 5.19: Imaginary part of Σ when maximum $n = 3$ order is considered at T=0.008 in the computations. See similar notations in HBM.

Chapter 6

Monte Carlo Summation Technique and Future Work

Note that in the above Feynman diagram summations of Eq.(4.49) and Eq.(4.50), we do the k summation in momentum space for *all* the diagrams of order n's. It is a *brute force* approach and then need a lot of computer CPU time.

Remember that in Chapter 2, the Importance Sampling Monte Carlo method can bring us the more efficient technique to sample a function at points where the main contribution comes from in a *summation* expression. Eq.(4.49) is a *high-dimensional* summation expression, therefore the sum of the higher order ($n \geq 2$) graphs, denoted by $\Sigma^{(>)}(k)$ in Eq.(4.49) can be calculated by Monte Carlo (MC) Summation Technique.

Similar to Eq.(2.4)-Eq.(2.8) in Chapter 2, we briefly give the basic idea of this Monte Carlo Summation Technique here. To sum up a function $I(x)$ over a high-dimensional domain D, we write its sum $\Sigma^{(I)}$ as[1, 2]

$$\Sigma^{(I)} \equiv \sum_{X \in D} I(x) = C_W \sum_{X \in D} S(X) P(X) \tag{6.1}$$

with a probability distribution $P(X)$, score $S(X)$ and norm factor C_W given by

$$P(X) = C_W^{-1} W(X), \quad S(X) \equiv I(X)/W(X), \quad C_W = \sum_{X \in D} W(X) \tag{6.2}$$

respectively. Here, $W(X)$ is an arbitrary non-negative weight function with $W(X) > 0$ where $|I(X)| > 0$. Using a Markov-type random walk procedure, we generate a

large of random $X-$point, $X^{(1)}$, $X^{(1)}$,...,$X^{(M)} \in D$, each with probability $P(X)$, and evaluate the MC average of $S(X)$

$$\langle S \rangle_M := M^{-1} \sum_{m=1}^{M} S(X^{(m)}) \tag{6.3}$$

For $M \to \infty$, $\langle S \rangle_M \to \Sigma^{(I)}/C_W$ with a variance $\delta S^2 \sim O(M^{-1})$. The evaluation of C_W, can be carried out by an analogous MC summation, with the same weight $W(X)$.

The implementation of this Monte Carlo diagram summation method for $n > 1$ higher order Feynman diagram expansion poses major algorithmic and computational challenges in several, quite distinct areas of computational science. The simultaneous stochastic summation over diagram topologies and over internal momentum-energy variables require novel MC updating and scoring approaches as well as major efforts to achieve variance minimization. The detailed description of this method combined with Self-Consistent Feynman Diagram Expansion technique can be found in [3, 4].

The first and successful application of this Monte Carlo Diagram Summation Technique is for the single Anderson impurity model (AIM) up to n=6 order Feynman diagram summation. This method combines the stochastic Monte Carlo sampling technique with a self-consistent Feynman diagram summation into a controlled approximation tool where the self-energy is calculated and compared with quantum Monte Carlo data[4].

Fig.6.1 and Fig.6.2 show two comparisons of Monte Carlo Diagram Summation Technique results (performed in the real space and then Fourier transformed into the k space) and brute force results (k space) for the first time iteration of 2×2 Hubbard model including diagrams up to $n = 3$. Those two results are in very good agreement.

For the future perspectives of this Monte Carlo Feynman Diagram Expansion technique, we may work in the following directions:

(1) Try to obtain the results with the higher order $n > 3$ for the AIM and HBM, and to study the behavior of those models with higher order terms. Similar to the Quantum Monte Carlo (QMC) algorithm, this MC summation here also exhibits a "minus-sign" problem, however, we expect the minus-sign problem to be manageable[5], at least up to $n_{max} \sim 10 - 20$.

(2) Parallelization of the codes to reduce the computer CPU time.

(3) Applications and Extensions of this MC Feynman diagram summation technique. In addition to the Hubbard model (HBM) and Anderson Impurity model (AIM), this technique can also be used in other strongly correlated electron physics, such as the cuprate high-temperature superconductors (HTSC)[6], infinite dimensional Hubbard model (IDHBM)[7], etc. Future extensions of this approach will include applications to (i) multi-band models, relevant to cuprates[8]; (ii) quantum chemistry; (iii) electronic structure of solids. etc.

6.1 References

[1] M.H. Kalos, P.A. Whitlock, Monte Carlo Methods (Wiley, New York, 1986).

[2] Applications of the Monte Carlo Method in Statistical Physics, eds. K. Binder, Topics. Curr. Phys. Vol. 36, 2nd edn. (Springer, Berlin, Heidelberg, 1987).

[3] H.-B. Schüttler, J.N. Corcoran, D.K. Lowenthal, R.W. Robinson, Summation of High-order Feynman Graph Expansions, NSF Proposal, ITR-0081789.

[4] A. Voigt, Ce-Jun Liu, Qun Wang, R.W. Robinson, H.-B. Schüttler, Stochastic Feynman diagram summation for the Anderson impurity model. http://www.csp.uga.edu/publications/HBS/

[5] S.R. White, D.J. Scalapino, R.L. Sugar, E.Y. Loh, J.E. Gubernatis, R.T. Scalettar, Phys. Rev. B **40** 506(1989).

[6] F.-C. Zhang, T.M. Rice, Phys. Rev. B **37** 3759(1988).

[7] W. Metzner, D. Vollhardt, Phys. Rev. Lett. **62** 324(1989).

[8] J.D. Jorgensen, H.-B. Schüttler, D.G. Hinks, D.W. Capone II, K. Zhang, M.B. Brodsky, Phys. Rev. Lett. **58** 1024(1987).

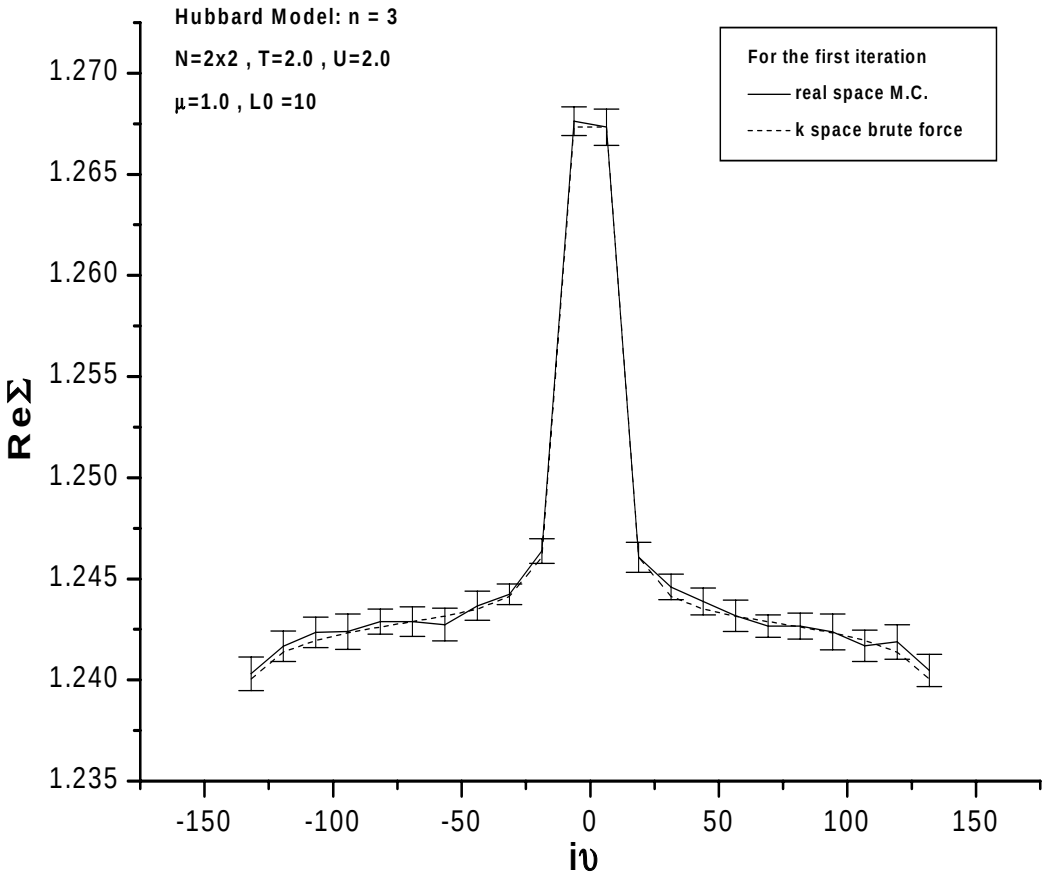

Figure 6.1: real part of the total Σ when maximum $n = 3$ order is considered in the 2X2 HBM for the 1st iteration at T=2.0, U=2.0 .

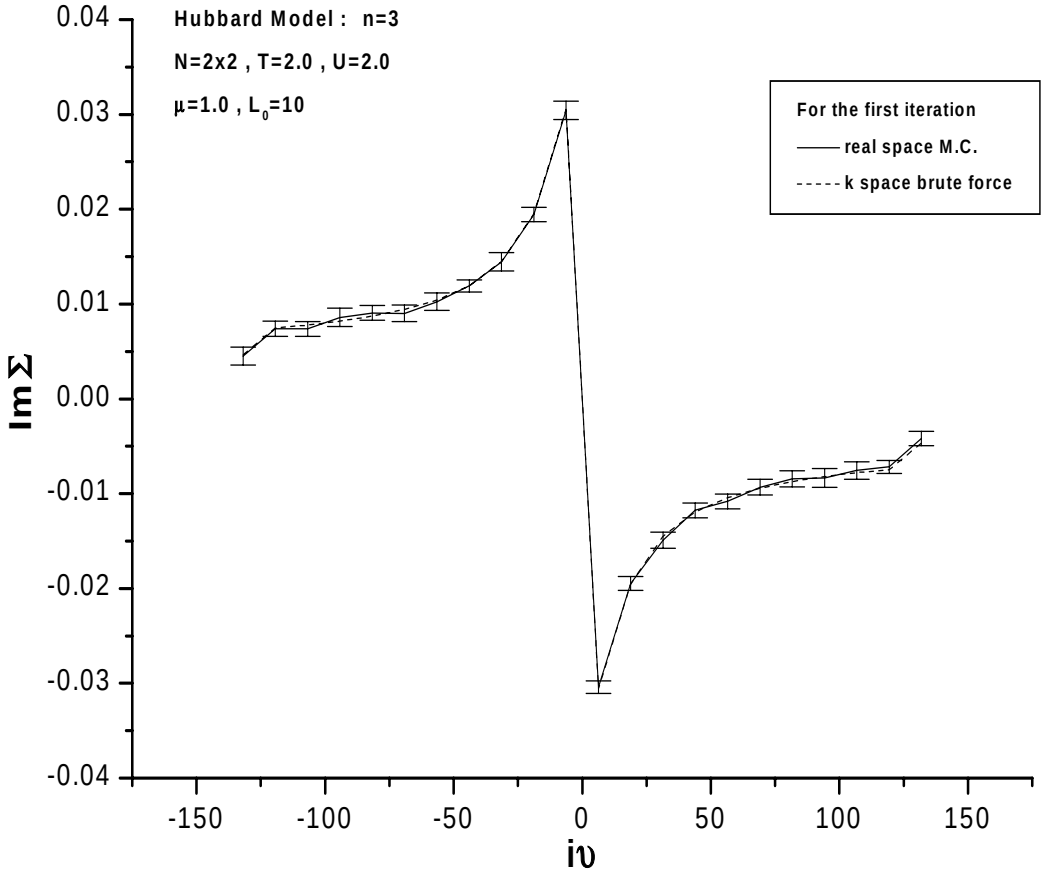

Figure 6.2: imaginary part of the total Σ when maximum $n = 3$ order is considered in the 2X2 HBM for the 1st iteration at T=2.0, U=2.0.